Ph.D. Thesis

Towards development of a thermal monitoring system and analysis of meteorological parameters for the HartRAO Lunar Laser Ranging telescope

By:
Lehlohonolo Philemon Tsele

Supervisor:
Professor Ludwig Combrinck

A thesis submitted in partial fulfilment of the requirements for the degree of Doctor of Philosophy in Geoinformatics

Department of Geography, Geoinformatics and Meteorology
University of Pretoria

26 July 2019

Declaration of originality

This is to certify that the work is entirely my own and not of any other person, unless explicitly acknowledged (including citation of published and unpublished sources). The work has not previously been submitted in any form to the University of Pretoria or to any other institution for assessment or for any other purpose.

Signed:

Date: 26 July 2019

ACKNOWLEDGMENTS

I would like to express my innermost gratitude to the Almighty God of Mount Zion, whom I believe this study became a success through Him. This PhD research work was supported in part by the National Research Foundation (NRF) of South Africa for the Unique Grant No. 93952. Any opinion, finding and conclusion or recommendation expressed in the material is that of the author(s), and the NRF does not accept any liability in this regard. We express our gratitude to the Inkaba yeAfrica project and the Department of Science and Technology of South Africa and Hartebeesthoek Radio Astronomy Observatory (HartRAO) for support. In addition, special thanks to the Department of Research and Innovation Support of the University of Pretoria (explicitly, Dr. Patricia Smit and Prof. Stephanie Burton) for additional funding support.

This PhD research work was implemented at the Department of Geography, Geoinformatics and Meteorology (GGM), University of Pretoria, as well as the Hartebeesthoek Radio Astronomy Observatory (HartRAO) in Krugersdorp, South Africa. Special thanks to these institutions for their firm support with the research facilities and equipment needed for the execution of this study. I am grateful to Prof. Ludwig Combrinck, Mr. Bongani Ngcobo and Dr. Roelf Botha for their incredible support and advice all the way throughout this research work. In particular, I would like to thank Prof. Combrinck for providing me with the opportunity to work on this PhD research, in an effort to contribute to the overall Lunar Laser Ranging telescope project at HartRAO. Furthermore, I would like to thank Mr. Ngcobo for his time, patience, encouragement and technical contribution dedicated to this study. Special thanks to Dr. Botha, Mr. Andre van der Merwe and the HartRAO technical team for their support during the LLR tube integration phase. Special thanks goes to Dr. Abel Ramoelo for his mentorship and encouragement throughout this process until the end. Special thanks also goes to my colleagues in the GGM department for their support.

Last but definitely not least, I would like to express my heartfelt gratitude to my wife (Virginia), mom (Rebecca) and late father (Paul) for their endless support and affectionateness during the duration of this research work.

PUBLISHED MATERIAL FROM THIS THESIS

1) List of published journal articles on the current PhD

- Tsela, P., Combrinck, L., Botha, R., & Ngcobo, B. (**2016**). Thermal analysis of the LLR optical telescope tube assembly based in Hartebeesthoek Radio Astronomy Observatory. *Acta Geodaetica et Geophysica*, *51*(3), 393-403.
- Tsela, P. L., Combrinck, W. L., Botha, R. C., & Ngcobo, B. L. (**2016**). A proposed mathematical model of thermal variations on the HartRAO Lunar Laser Ranging telescope for enhanced test of Earth-Moon system dynamics. *South African Journal of Geology 2016*, *119*(1), 83-90.
- Tsela, P. L., Combrinck, L., & Ngcobo, B. (**2016**). A spatiotemporal analysis of the effect of ambient temperatures on the thermal behaviour of the Lunar Laser Ranging optical telescope at Hartebeesthoek Radio Astronomy Observatory. *South African Journal of Geomatics*, *5*(3), 373-392.

2) Paper(s) submitted on the current PhD

- Tsele, P.L., Combrinck, L.,Ngcobo, B., and Botha R. (**Submitted**). Analysis of thermally-induced displacements of the HartRAO Lunar Laser Ranger optical tube: impact on pointing. *South African Journal of Geomatics*

3) **List of conferences presentation on the current PhD**

- Philemon Tsela, Ludwig Combrinck, Bongani Ngcobo and Roelf Botha. Thermal distortion dynamics of the HartRAO Lunar Laser Ranger optical telescope; impacts on pointing, characterisation and modelling. Oral presentation at the **10th Annual Inkaba yeAfrika and !Khure Africa Conference**, Matjiesfontein's Lord Milner Hotel, **28 September - 03 October, 2014**
- Philemon Tsela, Ludwig Combrinck, Bongani Ngcobo and Roelf Botha. Mathematical model of thermal variations on the HartRAO Lunar Laser Ranger optical telescope. Oral presentation at the **2nd National Conference on Global Change** on the topic, **1 - 5 December 2014**, Nelson Mandela Metropolitan University, Port Elizabeth, South Africa.
- Philemon Tsela, Ludwig Combrinck, Bongani Ngcobo. Tube assembly experiments for optimal temperature sensor placement on the HartRAO Lunar Laser Ranger telescope.

Oral presentation at the **61st Annual conference of the South African institute of physics**, University of Cape Town - **July 4 - 8, 2016**

- Philemon Tsele, Ludwig Combrinck, Bongani Ngcobo. Prototyping a thermal monitoring system for the one-metre aperture Lunar Laser Ranger tube assembly based at the Hartebeesthoek Radio Astronomy Observatory. Poster presented at the **20th International Workshop on Laser Ranging**, GFZ Helmholtz Centre, Potsdam, Telegrafenberg - **October 9-14, 2016**

ABSTRACT

The Hartebeesthoek Radio Astronomy Observatory (HartRAO) of South Africa is currently developing a Lunar Laser Ranger (LLR) system based on a 1-metre aperture telescope in collaboration with the National Aeronautics and Space Administration (NASA) and the Observatoire de la Côte d'Azur (OCA). This LLR will be an addition to a small number of operating LLR stations globally and it is expected to achieve sub-centimetre range precision to the Moon. Key to this achievement, requires thermal analysis of the composite telescope structure, based on thermal properties of the telescope component materials and their interaction with the environment through conventional heat transfer mechanisms. This analysis includes a thermal monitoring system that will feed temperature measurements to a model that will assist the steering and pointing software of the telescope in order to minimize tracking errors. In particular, no study has been reported previously on the thermal behaviour and related structural changes coupled with displacements of the HartRAO LLR composite structure with respect to ambient air temperature at the observatory site. Furthermore, a prototype pointing and steering software package developed for the HartRAO LLR, has so far only been tested on a 125 mm dual refractor testbed telescope (under room temperature conditions) and achieved root mean squared error values at the 0.5 arcsecond level. The extent of variation of the achieved error values is currently not known, particularly when the pointing model will be tested on the actual LLR telescope, which will be exposed to the varying thermal environment during operation.

Therefore, in this study the thermal behaviour and related distortion dynamics of the HartRAO LLR telescope composite structure were modelled for possible adverse impact on pointing. Key findings of this research study were that the thermal response time varies per LLR telescope material component, primarily due to their respective thermal properties. The spider assembly and outer tube surface had the largest range of thermal variations, and thus were identified as the main areas on the telescope where most thermal variations can be expected. However, the primary mirror surface including its mount as well as the fork assembly had the lowest range of thermal variations. The total deformations of the tube assembly were found to be in the range 2.9 μm to 40.7 μm from night (00h00) until approximately midday (11h30). The primary mirror had virtually zero localised deformations due to its resistance against temperature change. The LLR thermal dynamic model was proposed and several test results of the proposed model were presented which covered the placement of RTD sensors on

thermally-important areas of the tube structure; measurement and interpolation of the optical tube temperatures; and tube displacements due to assumed thermal deformations were reported using a laser distance-measurement system. In particular, the smallest variations in relative displacements of the tube were found to be 0.418 mm (east), 0.512 mm (north) and 0.670 mm (height) whereas, the largest variations were 0.523 mm (east), 0.691 mm (north) and 0.751 mm (height) during the time period considered. This period was characterized by ambient temperatures that varied between 11.20 °C and 29.90 °C and corresponding tube temperatures that varied between 13.75 °C and 33.84 °C.

This information constitutes an important input for guiding the efforts to determine the amount of correction needed to be fed into the LLR telescope pointing model to counteract expected thermally-induced pointing offsets. Overall these results are a step towards the development of a real-time thermal monitoring system for the HartRAO LLR telescope, which is imperative in maximizing the pointing accuracy of the telescope, thereby increasing the chance of being on-target with the retroreflectors located on the lunar surface. Efforts to maximize pointing accuracy for the HartRAO LLR would support the global effort of high-accuracy laser ranging, which currently provides millimetre precision. Lastly, these findings have significant implications in exploring strategies and options for developing thermal dynamic models and monitoring systems for current and future LLR optical telescopes.

LIST OF ACRONYMS

Apollo	NASA missions to the Moon of 1969 - 1974
APOLLO	Apache Point Observatory Lunar Laser Ranging Operation
AFCRL	Air Force Cambridge Research Laboratories Lunar Ranging Observatory
CAD	Computer-aided design
CMB	Liquid core/ solid mantle boundary
CTE	Coefficient of thermal expansion
EOP	Earth Orientation Parameters
EP	Equivalence Principle
FE	Finite element
GNSS	Global Navigation Satellite Systems
HartRAO	Hartebeesthoek Radio Astronomy Observatory
LLR	Lunar Laser Ranger
LURE	Lunar ranging Experiment Observatory
LLRRA-21	Lunar Laser Ranging Retroreflector Array for the 21st Century
MLRS	McDonald Laser Ranging System
MLRO	Matera Laser Ranging Observatory
NASA	National Aeronautics and Space Administration
Nd:YAG	Neodymium-doped yttrium aluminum garnet
OCA	Observatoire de la Côte d'Azur
RMSE	Root mean squared errors
RTD	Resistant temperature detector
TMT	Thirty Meter telescope
UTC	Coordinated Universal Time
UT1	Universal Time

TABLE OF CONTENTS

LIST OF FIGURES

LIST OF TABLES

Chapter 1: Introduction

1.1. Brief background

One of the key considerations for the scientific performance of a ground-based telescope, is thermal analysis of the telescope composite structure and associated optics based on the thermal properties of its component materials and interaction with the varying local climatic environment (Mittag et al., 2008; Zheng et al., 2012; Tsela et al., 2016a; Wang et al., 2018). It is an experimental fact that classical telescopes built from materials such as aluminium alloys and steel are subject to varying dimensional changes due to temperature variation (Bely, 2003, Mittag et al., 2008; Murphy Jr et al., 2008; Pisanu et al., 2010; Vogiatzis et al., 2014). Thus, a thorough understanding of the thermal environment of the telescope observatory site, properties of the telescope component materials and system performance requirements could be essential for determining appropriate modeling procedures and mitigation strategies for the temperature variations, which are capable of inducing structural deformations and displacements of critical optical components of the telescope. In addition, temperature variations (also referred to as thermal variations in this study) have also been shown to have a consequent effect on the overall pointing error, especially of unhoused or open-air telescopes (Baars et al., 1988; Énard et al., 1996; Ukita, 1999; Greve and MacLeod, 2001; Shinnaga et al., 2004; Wresnik et al., 2007; Mittag et al., 2008; Cho et al., 2010; Pisanu et al., 2010; Vogiatzis, 2010).

In many realistic situations, the thermal state of an operating open-air ground-based telescope varies with time mainly due to the underlying heat transfer mechanisms that take place within the individual component materials, and also between the overall telescope body and its surrounding climatic conditions (Énard et al., 1996; Bely, 2003, Greve and Bremer, 2010). In particular, heat transfer by conduction, convection and radiation are the three key processes that normally take place simultaneously on an open-air telescope, and as a result, ought to be investigated in-order to: (i) understand their extent of influence on the specified operational temperature range of critical components for example, optics, detectors and supporting structure, and (ii) obtain precise parametric information that could aid development of robust thermal control models for predicting and mitigating their overall effect on the telescope's scientific performance; at least on optical and pointing accuracy requirements.

Several studies have widely demonstrated that constraining the thermal effects arising from heat transfer mechanisms by solely relying on passive control measures such as, coating and insulating the telescope component materials, may not yield desirable results (i.e. timely self-adjustment of the link lengths between the primary and secondary mirrors, mirror curvature changes and deformed structure) under extreme and rapid ambient climatic changes for example Ukita (1999). However, one of the recommended passive control measures is to design an adjustable telescope truss structure comprising diverse combinations of near-zero coefficient of thermal expansion material components (Atwood and O'Brien, 2003; Bely, 2003).

Alternatively, active thermal control measures have by far proven to be reliable in providing detailed (real-time) temperature monitoring and modeling of thermally-induced pointing errors. The measures entail installation of several temperature sensors on strategically identified locations throughout the telescope's critical components. Temperature measurements are acquired and subsequently analyzed for (i) monitoring of thermal variations and consequent deformations of the telescope composite structure, (ii) estimating the magnitude of thermally-induced displacements of critical components, so as to determine the amount of correction necessary to counteract thermally-induced pointing offsets, and/ or (iii) guiding the development of a robust thermal model for mitigating the thermal variations of the critical telescope elements (such as the tube and mirrors) to counteract thermal pointing errors (Ukita, 1999; Bremer and Penalver, 2002; Greve et al., 2005; Mittag et al., 2008; Murphy Jr et al., 2008; Greve and Kaercher, 2009; Pisanu et al., 2010; Tsela et al., 2016b).

Furthermore, the coupling of acquired temperature measurements with observations from inclinometers and laser distance-measurement systems have also shown the potential to determine structural displacements based on varying amounts of the incident beam drift (Hu et al., 2015; Cui et al., 2015; Cui et al., 2016) and correlations between the antenna pointing errors and thermally-induced deformations on selected structural components of the telescope (Pisanu et al., 2010). In overall, these studies confirm to a reasonable degree that thermal modeling, particularly for an open-air ground-based telescope may be necessary which ought to take into account the telescope's structural design, thermal properties of the component materials and site-specific varying climatic factors.

1.1.1. Brief overview of the laser ranging concept

In principle, laser ranging refers to the firing of ultrashort pulses of light from a source fixed at a particular location to a cube retroreflector mounted on a distant entity. In space geodesy, laser ranging is a technique used for acquiring accurate distance measurements between a particular Earth-based reference station and a fixed reference point (retroreflector arrays) on an orbiting satellite or the Moon surface (Figure 1). The main basic tools used in space geodesy for acquiring accurate distance measurements are widely known as Satellite Laser Ranging (SLR) and Lunar Laser Ranging (LLR). In particular, these tools make use of: (i) ultrashort laser pulses for ranging to the retroreflector arrays, (ii) optical receivers and photon detectors to record the light photons returned to the laser ranging station, and (iii) timing systems to measure the round-trip travel time of the laser pulses from the ground-based station to the optical retroreflectors on an orbiting satellite or the surface of the Moon (Bender et al., 1973; Seeber, 2008; Pearlman et al., 2019). This laser ranging concept is expanded upon further in Chapter 2.

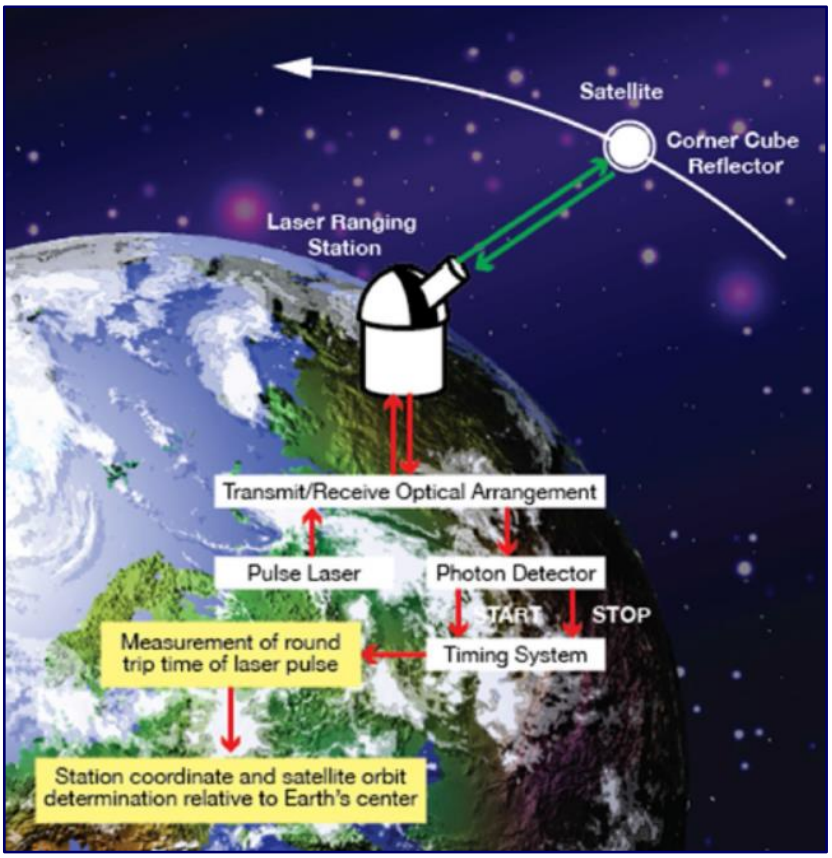

Figure 1: Simplified illustration of the laser ranging concept (source: Pearlman et al., 2019)

1.1.2. Overview of the International Laser Ranging Service

The International Laser Ranging Service (ILRS) was established in July 1999 by the International Association of Geodesy (IAG) with the aim of coordinating satellite and lunar ranging measurements, and ensuring successful delivery of geodetic data to a global user community (Pearlman et al., 2019). These measurements are coordinated through for example, network operations between stations, data archiving, access to data and analysis of data. As a result, the coordination of global satellite and lunar ranging data is key for generating a wide range of geodetic products, which are used to accurately maintain the International Terrestrial Reference Frame (ITRF) (Altamimi et al., 2016).

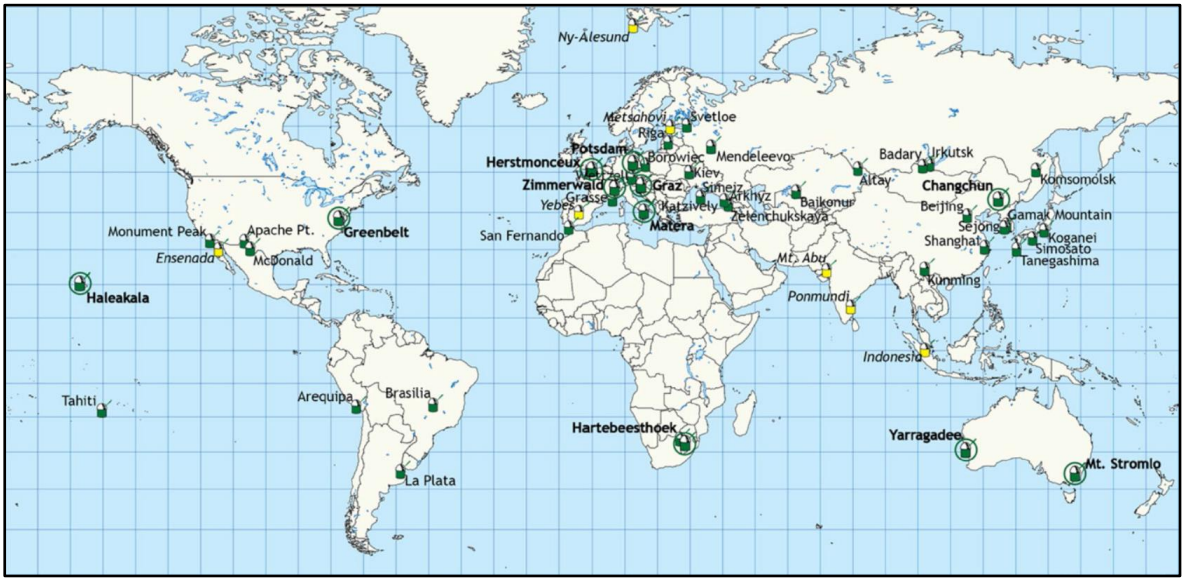

Figure 2: The current International Laser Ranging Service (ILRS) network. The network show stations (green symbols) that contribute to the ILRS operationally, as well as those stations (yellow symbols) that are under development. The green circled stations denote stations that currently contribute to the reference frame analysis (source: Pearlman et al., 2019).

The ILRS consists of a number of operational components which are fundamental to achieving its aim. The operational components include: (i) Observing stations, (ii) Operations Centres (OCs), (iii) Data Centres (DCs), (iv) Analysis Centres (ACs), (v) Central Bureau, and the (vi) Governing Board. For example, the observing stations approved as part of the ILRS network (Figure 2) are expected to adhere to the established set of procedures for ranging to the retroreflectors on the satellites and Moon. Additionally, the acquired data by the stations ought to comply with, among others the accuracy and timeliness requirements. On the other hand, the OCs collect laser ranging data and transfer it for archiving by the DCs. The DCs

forward the archived data to the ACs for deriving ILRS official products. Thereafter, the ACs return the products, which include Earth Orientation Parameters (EOP) and precise orbits for selected satellites, to the DCs to facilitate access of not only laser ranging data but the derived geodetic and geophysical ILRS products to a global user community. A detailed discussion of the ILRS operational components can be found in Pearlman et al. (2019).

1.2. Problem statement

Open-air ground-based telescopes utilized for laser ranging observations of space-based targets at sub-centimetre level accuracy, can suffer from structural deformations induced by varying ambient air factors, wind loading and/ or gravitational forces at the observatory site. These variables need to be measured to enable correction of the resulting pointing errors. This is more so on the LLR 1-metre aperture telescope that is being assembled at the Hartebeesthoek Radio Astronomy Observatory (HartRAO) of South Africa in collaboration with the National Aeronautics and Space Administration (NASA) and Observatoire de la Côte d'Azur (OCA) of France (Combrinck, 2011; Combrinck, 2014; Botha, 2016; Ndlovu et al., 2016; Tsela et al., 2016b; Munghemezulu et al., 2018). The HartRAO LLR is expected to make ranging observations to the corner cube retroreflectors located on the lunar surface with sub-centimetre level precision; and would contribute to ranging observations of 5 capable LLR stations based in the Northern Hemisphere (Murphy, 2013).

Key to the achievement of the required 1 arcsecond pointing accuracy of the HartRAO LLR (Combrinck, 2014) is modelling the thermal behaviour and related distortion dynamics of the HartRAO LLR composite structure for possible impact on pointing. In particular, no study has been previously reported on the thermal behaviour and related structural changes coupled with displacements, of the HartRAO LLR composite structure with respect to ambient air temperature. Secondly, a prototype steering and pointing software package developed for the HartRAO LLR, has so far only been operated on a 125 mm dual refractor testbed telescope (under room temperature conditions) and achieved root mean squared error values at the 0.5 arcsecond level (Combrinck, 2014). The extent of variation of the achieved error values is currently not known, particularly when the pointing model will be tested on the actual LLR telescope, which will be exposed to the varying thermal environment during operation.

Therefore, this study included (i) modelling the thermal behaviour of the LLR composite structure based on the site ambient temperature profile, (ii) proposal of a mathematical model

for monitoring thermal variations and related deformations of the LLR composite structure, and (iii) the determination of the extent of thermally-induced displacements of the optical tube, so as to inform efforts to determine the amount of correction needed to be fed into the LLR telescope pointing model (Combrinck, 2014) to counteract expected thermally-induced pointing offsets. The efforts are a step towards the development of a thermal monitoring system for the HartRAO LLR telescope, which is imperative in maximizing the pointing accuracy of the telescope, thereby increasing the chance being on-target with the retroreflectors located on lunar surface.

1.3. Research aim

The aim of the study was to model the thermal behaviour and related distortion dynamics of the HartRAO LLR composite structure for possible impact on pointing.

1.4. Research objectives

The objectives of the study were to:

(i) investigate the extent of influence of varying ambient air temperatures at the HartRAO site on the thermal behaviour (thermal response times, variations and deformations) of the first-ever LLR telescope in the Southern Hemisphere;

(ii) propose a thermal model for monitoring thermal variations and related deformations of the HartRAO LLR telescope composite structure; and

(iii) quantify the extent of thermally-induced tube displacements during day- and nighttime, so as to inform efforts to determine the amount of correction needed to be fed into the LLR telescope pointing model (Combrinck, 2014) to counteract thermally-induced pointing offsets.

1.5. Overview of Lunar Laser Ranging scientific contributions

In particular, LLR measurements offer potentially more comprehensive solutions for accurate probes of, amongst others, the Moon's motion around the Earth, fundamental gravitational physics, and dynamics of the Moon including the determination of EOP. For example, LLR continues to provide valuable tests of Einstein's Equivalence Principle (EP) dating back from 1976 (Williams et al., 1976). Einstein's EP widely known as the universality of free fall; predicts that the Earth and Moon accelerate alike in the Sun's direction. This theory

has been precisely tested through LLR by comparing the relative gravitational and inertial masses for the Earth and Moon celestial bodies in order to determine whether these bodies have a similar acceleration rate toward the Sun (Williams et al., 2004; Williams et al., 2012). If the two aforementioned celestial bodies exhibit differential acceleration, this may cause displacement of the Moon's orbit in the direction of the Sun, thus violating EP (Nordtvedt, 1999).

The available empirical findings based on analyses of long-term LLR measurements revealed a slow recession rate of the Moon's orbit by about 3.8 cm away from the Earth annually due to tidal friction (Murphy, 2013). In addition, LLR provides a unique opportunity to test temporal changes of the Newtonian gravitational constant, *G*. Temporal changes in Newton's gravitational constant, *G* are constrained to $(2\pm7)\times10^{-13}$ per year which indicates the stableness of the universal force of gravity (Williams et al., 2004; Müller and Biskupek, 2007). While this constraint corroborates Einstein's General Relativity theory which does not predict a changing *G* however, this could contradict other theories of gravity (see Murphy (2013) and references therein).

Furthermore, LLR is being used to define coordinate frames, investigate tidal acceleration of the Moon, geodetic precession (Chapront and Francou, 2006) as well as to study geodynamics (Dickey et al., 1994) and the lunar interior dynamics (Williams and Boggs, 2008) through range distance measurements obtained at various LLR stations worldwide. LLR measurements from various stations, provide information that contributes to the derivation of global ranging data products which can be used in scientific activities spanning for example geophysics, oceanographic research, and geodesy for precise orbit determination and maintenance of the ITRF (Combrinck, 2011; Hofmann et al., 2018; Pearlman et al., 2019).

1.6. Thesis outline

This thesis consists of 5 chapters. The first chapter contains a comprehensive summary and context of this research study as well as the problem statement, aim and objectives.

Chapter 2 provides a detailed discussion of key published material related to this research, and highlights the scientific justification for this study, including the contribution to existing knowledge in the area of telescope thermal modelling.

A detailed discussion of the methodology is presented in Chapter 3 which encompasses the: (a) description of the study site, (b) LLR telescope and its thermal properties, (c) data and equipment used, (d) proposed thermal model and (e) setup of experiments conducted in this study.

Furthermore, Chapter 4 contains the results obtained in this study, coupled with a detailed discussion of the findings.

Lastly, Chapter 5 provides concluding remarks based on the results, while reflecting on the research problem statement and/or significance of the study as well as the aim and objectives of the study.

Chapter 2: Literature review

2.1. Lunar Laser Ranging overview

2.1.1. Basics of Lunar Laser Ranging

Over the past 40 years, the placement of retroreflectors on the lunar surface led to the evolution of the LLR technique. The placement was done through a series of the manned Apollo missions, as well as a series of the unmanned Soviet rover Lunokhod missions (Bender et al., 1973). In particular, the Apollo missions and their respective Moon landing dates were Apollo 11 on 20th July 1969, Apollo 14 on 5th February 1971 and Apollo 15 on 30th July 1971. In addition, the Moon landing dates of the Lunokhod missions 1 and 2 were 17 November 1970 and 15 January 1973 respectively (Figure 3). The retroreflectors placed on the Moon consists of reflective prism faces that return the incident laser beam to its original direction (Figure 3) and as a result, provide the only means to measure the Earth-Moon distance with the LLR technique (Murphy, 2013). The LLR technique basically requires a telescope located at a ground station for transmitting a light pulse to a retroreflector on the Moon (Figure 4). After about 2.5 seconds the retroreflector returns the light pulse in the same direction; and therefore, the departure and arrival times of the light pulse are recorded at the station for deriving Earth-Moon distance measurements (Veillet et al., 1993). The most recently reported precision of the acquisition of these measurements is 1 mm (Murphy, 2013).

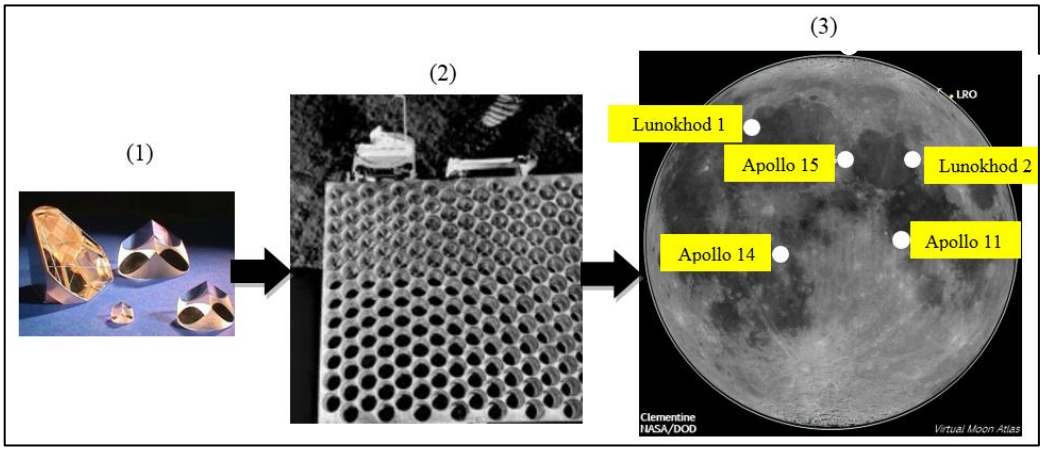

Figure 3: An illustration of the lunar cube reflectors at the Physics department of the University of California, San Diego (1). Hundreds of such cube reflectors are arranged in various retroreflector arrays for example the Apollo 15 array placed on the lunar surface, facing the Earth (2). Distribution of various retroreflector arrays placed on the lunar surface by the manned Apollo and unmanned Soviet rover missions (3).

The use of a laser for ranging to the Moon has several advantages such as making it possible to collimate the outgoing light beam, it makes provision for ultra-short pulses, and its light is extraordinarily directional notwithstanding the possibility of atmospheric distortions. For example, atmospheric turbulence is known to impose divergence on the outgoing beam at a scale of at least one arcsecond i.e. $1/3600^{th}$ of a degree (Murphy, 2013). In particular, such a minor angular size translates to the beam widening up-to approximately 2.0 km at the distance of the Moon and hence, most light photons, about 30 million from 50 transmitted pulses seldom hits the retroreflector(s). The photons that impinge on the corner reflectors, consequently return in a diffracted beam. For example, according to Murphy (2013) the Apollo corner reflectors can diverge the returning beam at a scale of approximately 7.5 arcseconds, which translates to an area wide enough cover about 15 km across the Earth's surface. At least a single photon would be received by the telescope provided the telescope employs a receiver that has high photon detection efficiency. Generally, there are efficient receivers for the green light (532 nm, commonly used for LLR) that exceed 70% photon detection efficiency (Prochazka et al., 2014).

Dickey et al. (1994) showed that the round-trip travel time of the light pulse between the ground-based ranging station and the corner retroreflector on the lunar surface, can be approximately derived using the following basic Equation (1):

$$\rho \simeq |\mathbf{r}| + \mathbf{R}_M \cdot \hat{\mathbf{r}} - \mathbf{R}_E \cdot \hat{\mathbf{r}} \qquad (1)$$

where $\mathbf{r}$ denotes the distance between Earth-Moon barycentre computed in the Barycentric Celestial Reference Frame, $\mathbf{R}_M$ denotes the selenocentric location of the lunar retroreflector on the Moon in the lunar-fixed system, and $\mathbf{R}_{\mathrm{E}}$ is the geocentric position of the ranging station in the Earth-fixed system.

A hypothetical illustration by Dickey et al. (1994) of the geometrical relationship between the above-mentioned parameters is presented in Figure 4. The Earth-Moon mean distance is 385 000 km and, given the respective equatorial radii of the Earth (6378 km) and Moon (1738 km), the lengths and relative orientations of the vectors $\mathbf{R}_{\mathrm{E}}$ and $\mathbf{R}_M$ could influence the measured distance.

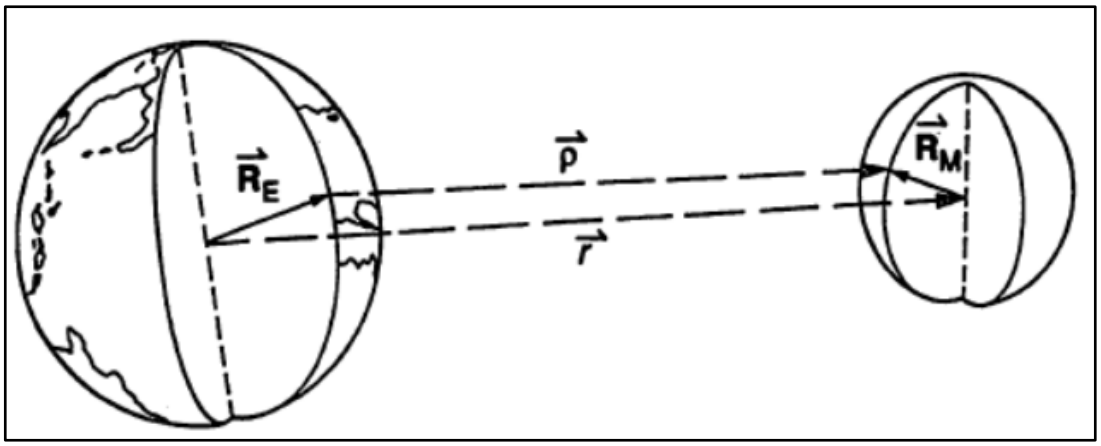

Figure 4: Hypothetical lunar laser ranging telescope transmitting laser pulses through the beam expander or optical tube aperture to the retroreflector array on the lunar surface. After the laser pulse impinge on the retroreflector, the light pulse is returned in the same direction and received at the telescope (source: Dickey et al., 1994).

However, given the Earth-Moon approximate long distance of 350 000 km, the basic observation equation that describes the accurate computation of Earth-Moon distance measurements ought to incorporate certain key parameters given by Müller et al. (2008) as:

$$d = c\frac{\tau}{2} = \left| \mathbf{r}_{\text{em}} - \mathbf{r}_{\text{station}} + \mathbf{r}_{\text{reflector}} \right| + c\Delta\tau \tag{2}$$

where the following parameters d, c, and τ represents the distance from the ground-based station to the retroreflector, the speed of light in a vacuum, and time-of-flight of the laser pulse, respectively. Furthermore, the three distinct vectors $\mathbf{r}_{\text{em}}$, $\mathbf{r}_{\text{station}}$, and $\mathbf{r}_{\text{reflector}}$ describe the connection between the geocentre and the selenocentre, geocentric position of the ground-based station, and the selenocentric position of the retroreflector arrays, respectively. Lastly, the parameter $\Delta\tau$ represent the applied travel-time corrections due to the delays caused during the propagation of the laser pulse through the non-linear atmospheric environment.

When ranging to the retroreflectors on the Moon, it is important that the transmitted laser pulse carry a sufficient number of photons, so that a sufficient number of photons can reach the corner cube reflectors (CCR's) and at least a single photon be returned to the telescope receiver (Märki, 2018). In particular, the large distance between the Earth and the Moon, makes it difficult to receive echoes from the Moon, hence the ratio of photon numbers received and

transmitted is approximately 1:10^{18} (Courde et al., 2017). To estimate the number of photons received by the ranging detector, Degnan (1993) proposed the radar link equation as follows:

$$n_{pe} = \eta_q \left(E_T \frac{\lambda}{hc}\right) \eta_t G_t \sigma \left(\frac{1}{4\pi R^2}\right)^2 A_r \eta_r T_a^2 T_c^2 \tag{3}$$

where n_{pe} denotes the number of received photons, η_q denotes the quantum efficiency of the detector (receiver), E_T denotes the total laser pulse energy, λ denotes the laser wavelength, h is Planck's constant, and c is the speed of light in a vacuum. Furthermore, the parameters $\eta_t, G_t,$ and σ represents the transmit optics efficiency, gain of the transmitter, and optical cross-section of the corner cube retroreflector, respectively; R is the slant range to the Moon retroreflector. Subsequently, the effective area of the receiver telescope, receive optics efficiency, unidirectional transmission through the atmosphere, and unidirectional transmission through the cirrus clouds if present, are denoted by the parameters $A_r, \eta_r,$ T_a and T_c respectively.

In Equation (3) the slant range R, is given by Degnan (1993) as:

$$R = -(R_E - h_t)\cos\theta_{zen} + \sqrt{(R_E + h_t)^2 \cos^2\theta + 2R_E(h_s - h_t) + h_s^2 - h_t^2} \tag{4}$$

where R_E denotes the Earth radius at the Equator (6378 km), h_t denotes the station-height above sea level, h_s denotes the Moon's elevation above sea level, and θ_{zen} is the zenith angle of the Moon as observed from the station. The two Equations (3) and (4) were theoretically tested (Munghemezulu, 2018) based on the estimated, link budget equation parameters for the HartRAO LLR station, and as a result, 5 return photons per minute is expected to be received by the HartRAO LLR telescope. Since, on average it takes about 5 to 25 minutes of ranging in order to generate a typical normal point (Merkowitz, 2010), the HartRAO 1-metre LLR can be expected to collect up-to approximately 100 photons, which may be sufficient to obtain normal points at the envisaged mm level.

2.1.2. Detailed overview of Lunar Laser Ranging scientific contributions

Accurate LLR measurements offer potentially more comprehensive solutions for accurate probes of, amongst others, the Moon's motion around the Earth, fundamental gravitational physics, Einstein's EP, and dynamics of the Moon including the determination of EOP (Müller and Tesmer, 2002). The following sections contain selected examples detailing the contribution of LLR to science.

2.1.2.1. Equivalence Principle Tests

Tests of the EP using LLR data are performed by comparing gravitational accelerations of the Earth and the Moon test bodies toward the Sun (Williams et al., 2012). The hypothesis is that both Earth and Moon regardless of their different masses and compositions, have the same gravitational accelerations a_1 and a_2 in the same gravitational field as follows (Williams et al., 2004):

$$\frac{\Delta a}{a} = \frac{a_1 - a_2}{\frac{1}{2}(a_1 + a_2)} = \left(\frac{M_G}{M_I}\right)_1 - \left(\frac{M_G}{M_I}\right)_2 \tag{5}$$

where parameters M_I and M_G denote the gravitational mass and inertial mass of each test body. Precise differential acceleration measurement is important for determining the sensitivity of the EP test (Williams et al., 2012).

Violation of the EP, would result in the inequality of gravitational and inertial masses such that, the Earth and Moon falls towards the Sun at slightly different rates, leading to the perturbation of the lunar orbit (Nordtvedt Jr, 1968). In case the EP is violated, a range signature with 29.53 day synodic period will result as the lunar orbit will be displaced along the Earth-Sun line. Furthermore, LLR tests of the total EP, taking into cognisance both composition and gravitational self-energy for the Earth and Moon in the gravitational field of the Sun, yield $\Delta a/a$ values of $(-1 \pm 2) \times 10^{-13}$ (Williams et al., 2002) as well as $(-0.7 \pm 1.5) \times 10^{-13}$ (Anderson and Williams, 2001) which correspond to a range amplitude of 2 ± 4 mm (Williams et al., 2004).

In addition, recent test results of EP based on the analysis of LLR data spanning 16,250 NPs yielded the value of $(-0.8 \pm 1.3) \times 10^{-13}$ (Turyshev and Williams, 2007). Overall, the

analysis of historic, accurate Earth-Moon distance measurements does not reveal significant evidence for a violation of EP (in the general theory of relativity) compared to its uncertainty. However, further tests of EP could facility efforts to find a new theory of gravity (Williams et al., 2012) and more stringent limits on any violation of EP. While the Earth and the Moon test bodies vary in composition and gravitational self-energy, the EP is considered to have two formations namely; the weak equivalence principle (WEP) and the strong equivalence principle (SEP). The latter is sensitive to gravitational energy of a body i.e. Earth/Moon, whereas, the former is sensitive to the composition.

2.1.2.2. Tests of gravitational constant, G

Analysis of LLR time-series data permits the determination of limits on the variability of the gravitational constant *G*. Such determination is possible due to the sensitivity of the Moon's orbit to the longitude of the Sun. In particular, this constant describes the temporal variation of gravity due to the magnification of the universe (Turyshev and Williams, 2007). For example, the potential variation of *G* with time, exert torques on not only the monthly lunar orbit but also the annual Earth-Moon orbit around the Sun (Nordtvedt, 1999). Considering Kepler's third law, it is evident that a changing *G* with time would appear peculiar to the evolution of the Moon's orbital period (Merkowitz, 2010):

$$P^2 = \frac{4\pi r^3}{Gm}, \tag{6}$$

and by taking the time derivative and re-arranging comes to:

$$\frac{\dot{G}}{G} = 3\frac{\dot{r}}{r} - 2\frac{\dot{P}}{P} - \frac{\dot{m}}{m} \tag{7}$$

Utilising LLR data, the anomalous evolution of the Moon's orbit can be estimated, coupled with an estimate for *G* (Williams et al., 1996). The analysis of LLR data, sets a limit on the gravitational constant $\dot{G}/G$ estimated to be $(6 \pm 7) \times 10^{-13}$ year^{-1} (Turyshev and Williams, 2007) and more recently $(-0.7 \pm 3.8) \times 10^{-13}$ year^{-1} (Hofmann et al., 2010). Continued LLR observations are expected to enhance this limit.

2.1.2.3. Tidal acceleration of the Moon and Love numbers

Analysis of LLR observations aid in the modelling of tidal effects affecting the Earth-Moon distance measurements (Müller and Tesmer, 2002). Such effects have significant implications for the accuracy of the acquired observations at the LLR station. The Moon is a tide generating body and causes a bulge on the non-ideal elastic Earth. As a result, the bulge of the Earth relative to the Earth-Moon direction, exerts a secular acceleration of the Moon's longitude (Chapront and Francou, 2006). This produces a tidal acceleration of about -25.90″/ cy^2 in the lunar longitude (Pavlov et al., 2016), which slows the rotation rate of the Earth, coupled with an increase of the length of day (Chapront et al., 2002; Chapront and Francou, 2006). Another consequence is the slow recession rate of the Moon's orbit by about 38.20 $mm.year^{-1}$ away from the Earth (Pavlov et al., 2016).

Furthermore, the global or site-specific tidal displacement parameters h_2 (horizontal tides) and l_2 (vertical tides) also called Love numbers and the tidal dissipation parameter τ_m can be estimated to investigate their effect on relativistic quantities. Various tidal parameter values were reported in Müller and Tesmer (2002) for each LLR station. The same study also reported global estimates of the different Love numbers as:

$$\delta h_2 = -0.001 \pm 0.006$$

$$\delta l_2 = +0.014 \pm 0.002$$

In addition, based on LLR observations, the potential Love number k_2 can be estimated from tidal variation of the gravity field (Konopliv et al., 1998).

2.1.2.4. Lunar Science

LLR data contains a wealth of information that can be used to potentially expose details about the dynamics and the inner structure of the Moon. For example, the tidal Love numbers (known to be responsive to the structure and internal elastic properties of the Moon (Williams and Boggs, 2008), moment of inertia ratios, tidal quality factor and changes in the lunar physical librations, obtained from the analysis of LLR data reveal more insight and understanding of the deeper structure of the Moon, mass distribution and internal dynamics (Khan et al., 2004; Williams et al., 2004).

Investigations on the existence of a lunar core, are empirically aided by the sensed properties detected using LLR through physical librations and tides, which indicates a liquid core with a turbulent boundary layer (Williams et al., 2004; Williams and Boggs, 2008). In particular, the first property that indicates a liquid core is energy dissipation which arises at the liquid core/ solid mantle boundary (denoted, CMB). Such dissipation may be triggered by the interaction between tides in the solid mantle and CMB. Furthermore, the second property can be inferred from the ellipticity of CMB which results in a torque as the liquid travels along the oblate spheroid (Williams and Boggs, 2008). The third property arises from the moment of inertia of the liquid core which has an effect on the periodic displacement of a physical libration term (Williams and Boggs, 2008).

The tri-axial mass distribution of the Moon is associated with the principal moments of inertia as follows: A < B < C (Murphy, 2013). The moments of inertia are measured using both the Lunar Prospector (Konopliv et al., 1998) and LLR time-series data (Khan et al., 2004). Thus, sensitivity to the lunar physical librations allows precise calculation of the relative differences in the aforementioned principal moments of inertia to the 0.05% level (Murphy, 2013) as follows:

$$\beta = \frac{(C - A)}{B} \tag{8}$$

$$\gamma = \frac{(B - A)}{C} \tag{9}$$

The current estimated values for the quantities in (8) and (9) are reportedly ~6.3×10^{-4} and ~2.3×10^{-4}, respectively (Murphy, 2013).

Other scientific contributions from LLR include: (i) the precise determination of Earth Orientation Parameters, (ii) Relativity and gravity (iii), Gravitomagnetism and Parameterized Post-Newtonian (PPN) tests, and the (iv) Inverse Square Law. Further details pertaining these scientific contributions can be found in Murphy (2013) and references there in.

2.1.3. Historical overview of observatories with Lunar laser capabilities

Several observatories (Table 1) equipped with lunar ranging capabilities were established across various parts of the world. During the period 1969-1972 a number of observatories located in California, Arizona, Pic du Midi de Bigorre and Tokyo (Table 1) had already started ranging to the Moon and were able to obtain LLR measurements. Although the operational period of the aforementioned observatories was transient probably due to technical, operational and/or funding restrictions; all four abovementioned observatories provided useful empirical LLR data obtained at ranging accuracies of approximately 30 cm.

Subsequently, in 1973 LLR experiments were carried-out successfully at the McDonald observatory based on the 2.7 m telescope and became the first instrument ranging to the Moon on a regular basis (Bender et al., 1973; Silverberg, 1974). At the time, the telescope provided much more accurate lunar ranging information at about the 15 cm level owing to the exclusive use of a four-stage Q-switched ruby laser technology. The laser had a 4 nanosecond (ns) pulse width capable of transmitting laser light pulses with an amplified output energy of 3 Joules (J) per pulse at a repetition rate of one pulse every 3 seconds as well as being able to receive the returned laser light (i.e., Earth-Moon-Earth round-trip travel time) within 1 ns. The LLR empirical efforts at McDonald observatory were reported to be contributing 350 lunar range distance measurements annually (Silverberg, 1974), but time delays as a result of photon detectors and other electronics led to uncertainties in the range measurements (Bender et al., 1973).

Previous lunar ranging experiments coupled with challenges encountered at the observatories provided fundamental inputs in the construction of three additional observatories equipped with both satellite and lunar ranging capabilities around the mid 1980's in Hawaii, Grasse and Texas (Table 1). In particular, the Lunar Ranging Experiment (LURE) observatory based in Haleakala, Hawaii using an amplified pulsed laser system demonstrated improved ranging performance from the historical 15 cm to just below 2 cm; but ceased collecting LLR measurements regularly in 1990.

Table 1: Chronological history of the observatories with lunar laser ranging (LLR) capability. Only three LLR facilities based at Grasse, Texas (not operational for several years) and New Mexico observatories operate on a regular basis.
(Source: https://ilrs.cddis.eosdis.nasa.gov/science/scienceContributions/lunar.html).

Country	**LLR Observatory**	**Date of operation**	**Ranging accuracy**	**Aperture**	**Source**
California, United States	Lick Observatory	1969	30 cm	3.1 m	Faller et al. (1969)
Arizona, United States	Air Force Cambridge Research Laboratories Lunar Ranging Observatory (AFCRL)	1969	Restricted access	Restricted access	Hunt (1974)
Pic du Midi de Bigorre, France	Pic du Midi Observatory	1970	Restricted access	1 m	Calame et al. (1970)
Tokyo, Japan	Tokyo Astronomical Observatory	1972	Restricted access	Restricted access	Kozai (1972)
Texas, USA	McDonald Observatory	1973	15 cm	2.7 m	Bender et al. (1973)
Hawaii, United States	Lunar ranging Experiment (LURE) Observatory	1984	< 2 cm	N/A	Carter and Williams (1974)
Grasse, France	Observatoire de la Côte d'Azur	1984	1.5 cm	1.5 m	Samain et al. (1998)
Texas, USA	McDonald Laser Ranging System (MLRS)	1985	< 2 cm	0.76 m	Shelus (1985)
Matera, Italy	Matera Laser Ranging Observatory (MLRO)	2003	N/A	1.5 m	Bianco and Varghese (1994)
Southern New Mexico, USA	Apache Point Observatory Lunar Laser Ranging Operation (APOLLO)	2006	1 mm	3.5 m	Murphy Jr et al. (2008)

This was followed by the LLR facility utilizing a 1.5 m optical telescope which was established at the Observatoire de la Côte d'Azur (OCA) in Grasse, France in 1984 which acquired range measurements accurate to 1.5 cm level (Samain et al., 1998). This facility used a 70 picosecond (ps) neodymium doped yttrium aluminium garnet (Nd:YAG) two-colour laser system that emitted 4 short pulses at a repetition rate of 10 Hz with an energy pulse of 75 mJ (Samain et al., 1998).

The OCA LLR facility is characteristic of return rates of 0.002 and 0.01 photons per pulse (Samain et al., 1998) and contributed regular range measurements to various LLR data analyses centres (https://ilrs.cddis.eosdis.nasa.gov/science/scienceContributions/).

In the mid 1980's LLR system operations at the McDonald's observatory were decommissioned and replaced by a dual laser system with satellite and lunar ranging capabilities designed to regularly operate on a dedicated 0.76 m telescope (Shelus, 1985). This laser system is typical of a 200 ps Q-switched Nd:YAG that produces high-intensity laser pulses in the green wavelength (0.523 μm) with an energy pulse of 150 mJ and a repetition rate of 10 Hz. The satellite and lunar laser ranging facility at the McDonald observatory was named the McDonald Laser Ranging Station (MLRS). The station acquired range measurements on a regular basis at centimetre level accuracy, and was reported as one of the routine contributors to lunar range data between the years 1990 and 2006 (Murphy, 2013).

For the first time in LLR history, the recently established Apache Point Observatory Lunar Laser Ranging Operation (APOLLO) in New Mexico with a dedicated 3.5 m telescope achieved 1 mm range precision to the Moon (Murphy Jr et al., 2008). The LLR facility at APOLLO was implemented based on sophisticated optical and mechanical designs including electronics (Murphy Jr et al., 2008) and offer the most accurate ranging data to date following multi-decadal cm range measurements (Murphy, 2013).

By 2007, about 16000 LLR distance measurements were reported to have been acquired by the existing observatories (Müller et al., 2007) and this number is expected to increase considering integrated measurements from the currently operating and in progress LLR stations (i.e., Matera, Italy (this station has obtained successful returns) and Wettzell, Germany (this station is still under development)). These measurements have significant implications for conducting and improving tests of several gravitational and mechanical phenomena. Currently, all the LLR facilities collecting range measurements regularly are situated in the Northern

Hemisphere (Figure 5). New efforts are geared towards developing a dedicated station in South Africa i.e. Hartebeesthoek, represented in the Southern Hemisphere which will have LLR ranging capabilities (Combrinck, 2011; Tsela et al., 2016b; Munghemezulu et al., 2018). Additionally, a similar effort is underway at Mount Stromlo, Australia (Greene and Luck, 2002).

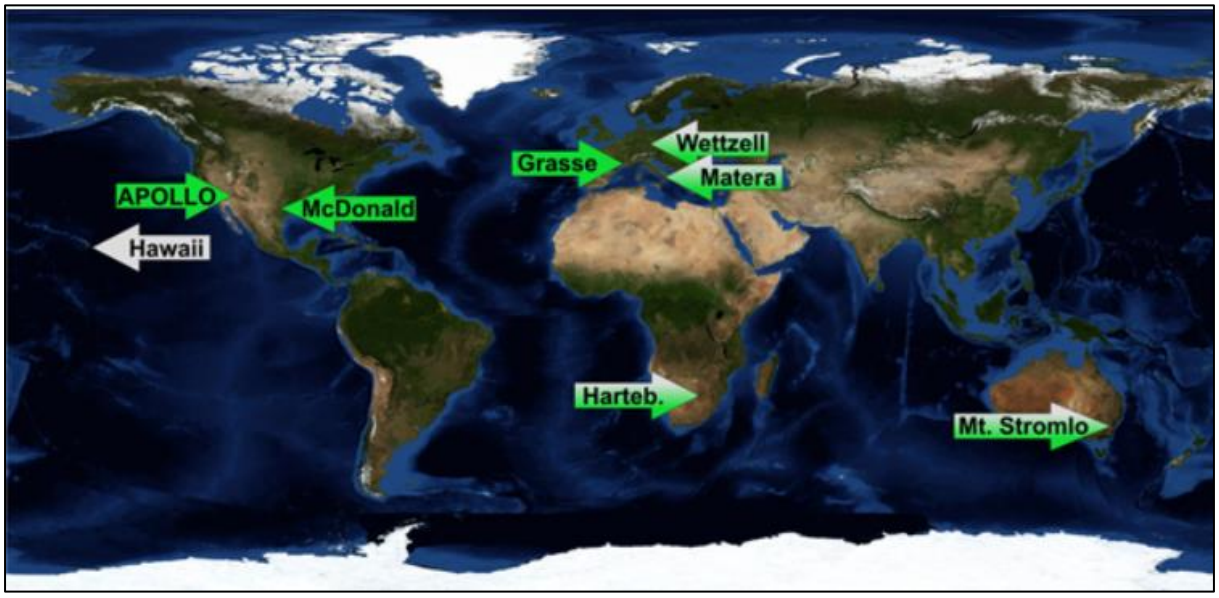

Figure 5: Distribution of stations with lunar laser ranging (LLR) facilities (https://ilrs.cddis.eosdis.nasa.gov/science/scienceContributions/lunar.html). Only three LLR stations namely, the McDonald Observatory (Texas, U.S.A), Grasse/ Observatoire de la Côte d'Azur (France) and Apache Point Observatory (New Mexico, U.S.A.) performed LLR on a regular basis. The McDonald Observatory has ceased LLR operations.

In particular, development of the new LLR geodetic station at the HartRAO of South Africa is planned to acquire (millimetre) Earth-Moon distance measurements in the Southern Hemisphere (Combrinck, 2014; Munghemezulu et al., 2016; Combrinck, 2014; Tsela et al., 2016b) using the refurbished ex-French 1-metre aperture telescope (Combrinck and Botha, 2014); and would be an addition to the five capable LLR stations based in the Northern Hemisphere (Noda et al., 2014), namely the McDonald Observatory (Texas, U.S.A), Observatoire de la Côte d'Azur (France), Apache Point Observatory (New Mexico, U.S.A.), Matera (Italy) and Wettzell (Germany). Currently, only the first 4 stations consistently contribute LLR observations to the ILRS database (Courde et al., 2017).

Considering the uneven distribution of capable LLR stations worldwide, the HartRAO LLR station would play a significant role in the continuous global monitoring of the Earth-Moon system dynamics, as well as understanding the processes in the complex Earth system. According to Hofmann et al. (2015), the current geometry network of LLR stations is likely to increase globally in the near future given the ongoing developmental efforts in other countries such as Russia (Vasilyev et al., 2014), Japan (Noda et al., 2014) and Chile (Fienga et al., 2014).

The HartRAO LLR system is expected to be operational in 2019 and will be using a 200 ps Nd:YAG laser system firing green light pulses at 10 Hz and 200 mJ per pulse. A suitable site for the permanent installation of the first South African LLR station has already been identified. The station will be located in Matjiesfontein, Western Cape province, which was found to be characterized by favourable optical seeing and atmospheric conditions as well as other important environmental characteristics that would enable effective operation of the LLR instrument (Nickola et al., 2011).

2.1.4. Infrared lunar laser ranging

Since the early 1990's the LLR measurement precision using the green detector at 532 nm particularly at the Grasse station in France, has reached millimetric level (Samain et al., 1998). However, at the time, the precision level when using the infrared (IR) detector at 1064 nm was reportedly insufficient relative to the green detector (Samain and Mangin, 1994) due to limitations of the detector's internal noise coupled with the requirement of sophisticated venting systems (Cova et al., 1994). About two decades later, notable advancement in indium gallium arsenide (InGaAs) technology (Itzler et al., 2011) led to an improved IR single-photon detector. Consequently, the Grasse station currently performs LLR in IR at 1064 nm utilising an InGaAs single-photon detector (Courde et al., 2017). IR LLR increased station efficiency on all five corner cube retro-reflectors as well as during the new and full Moon periods.

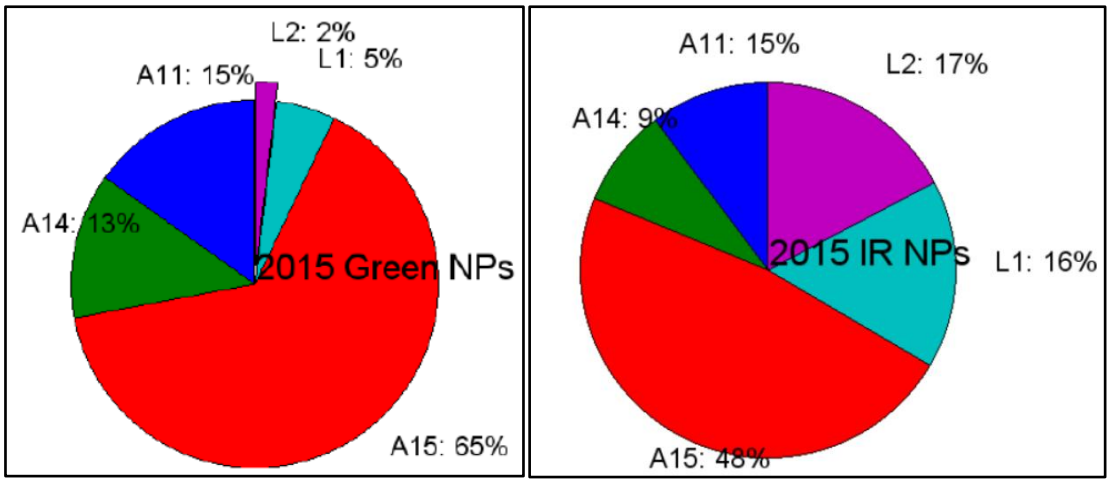

Figure 6: Distribution of normal points obtained on both the Apollo and Lunokhod retro-reflectors, using the green and infrared detectors of the Grasse LLR for the first nine months of 2015 (Source: Courde et al., 2017).

For example, IR LLR was found to have more normal point (NP) observations, precision of up-to three millimeters relative to a five millimetre level when the green detector is used. In principle, each NP represent, averaged range observations from multiple single-pulse measurements (Turyshev et al., 2013). Furthermore, the IR detector had increased observability duration, such that more i.e. 741 normal points (NPs) were acquired in IR compared to the green NPs at 211 (Courde et al., 2017). In addition, Courde et al. (2017) empirically found that IR LLR showed improved homogeneity in-terms of the distribution of NPs obtained on all five corner cube retro-reflectors (Figure 6). This is contrary to the green LLR observations which showed considerably low distribution of NPs on the Lunokhod retro-reflectors coupled with very high (65%) distribution on the Apollo retro-reflectors, especially A15 (Figure 6). Such findings suggest, utilising the IR detector in current and envisaged LLR stations for LLR observations, could have significant implications for the derived LLR scientific products, in-terms of increased accuracy of estimated parameters for example some lunar gravity field coefficients, mass of the Earth-Moon system, lunar orbit speed and location, and the lunar core dynamical parameters (Viswanathan et al., 2016; Viswanathan et al., 2017).

2.1.5. The next generation corner cube retroreflectors

In the last four decades, the ranging to Apollo lunar retroreflectors by different LLR stations led to numerous scientific findings in for example gravity, relativity and selenophysics (Murphy Jr et al., 2004). To date, the Apollo lunar retroreflectors still operate and are used to

generate new science results. Key to the accuracy of the science results, is the laser and detector (timing) technology used at the LLR station as well as the telescope aperture size.

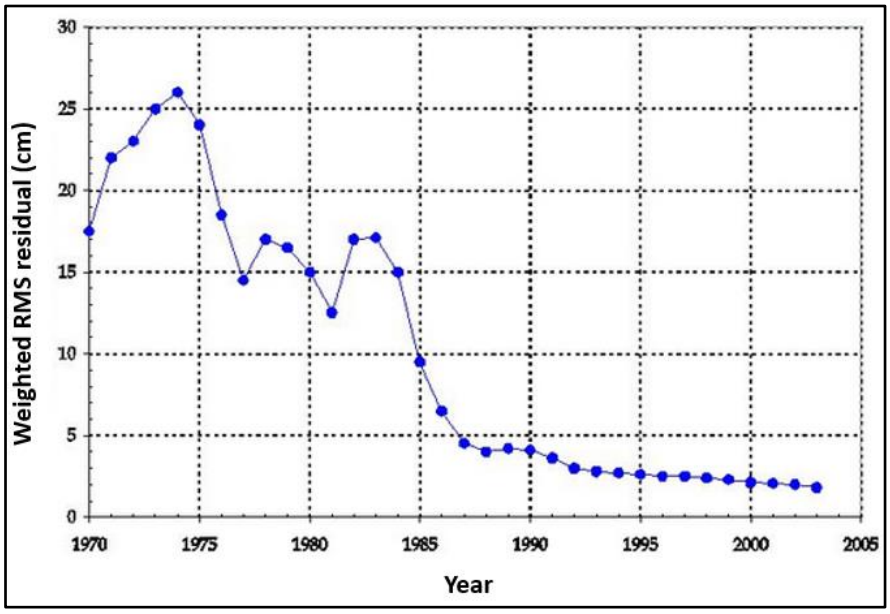

Figure 7: Historical accuracy of LLR data showing improvement in the ranging accuracy, since 1970 from 20 – 25 cm to about 2 cm in 2003 (Source: Murphy Jr et al., 2004).

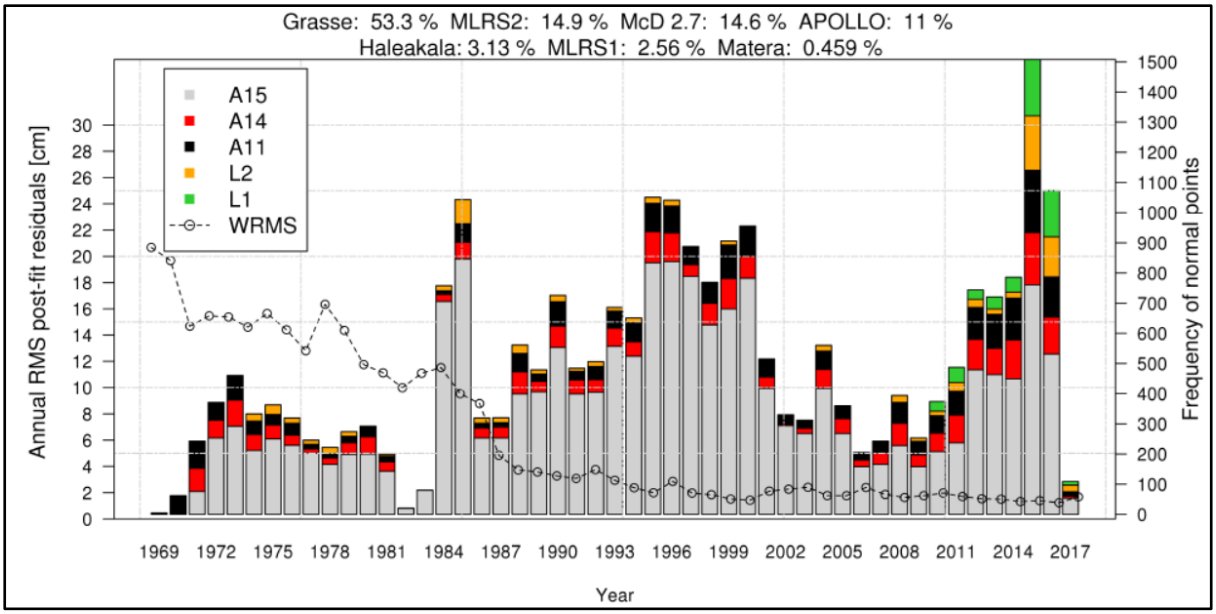

Figure 8: Historical accuracy of LLR data showing improvement in the ranging accuracy, from cm-level up-to sub-centimetre level (Source: Viswanathan et al., 2017). The LLR data accuracy is superimposed on ranging observations acquired from all five retroreflector arrays.

During the last few decades, there has been a dramatic amelioration of the abovementioned factors at various LLR stations such as the MLRS (0.76 m telescope), OCA (1.5 m telescope) and APOLLO (3.5 m telescope). Technological advancement has also led to

improved accuracy of the LLR observations by more than a factor of 200 (Currie et al., 2011), i.e. from the initial ranging accuracy of approximately 20 – 25 cm (in the 1970's) to about 2 cm in 2003 (Figure 7). In particular, the 2.7 m aperture telescope ranging system at McDonald Observatory (Bender et al., 1973) initially had ranging accuracies of around 25 cm, which improved to about 15 cm in the late 1970s due to incorporation of improved technology. Furthermore, around the mid-1980s the MLRS (Shelus, 1985) replaced the aforementioned telescope ranging system, while on the other hand, additional ranging systems from LURE (Carter and Williams, 1974) and OCA (Samain et al., 1998) equipped with enhanced detectors, lasers and precision timing systems came into existence, which gradually improved the ranging accuracy since those years to ~ 2 cm in 2003 (Williams et al., 2009). Generally, there is dominance of LLR observations to the A15 Apollo array; however, since 2014 notable changes are evident in the LLR observations acquired by the use of infrared ranging at Grasse. This showed improved homogeneity in terms of the distribution of normal points obtained on all five corner cube retro-reflectors. Furthermore, the accuracy of the current LLR observations has reached millimetre level (Figure 8).

Notwithstanding the progress thus far, the return signal level particularly from the Apollo lunar retroreflectors has diminished by a factor of 10 up to 100 below the expected signal return (from the Apollo arrays) when initially deployed (Burns and Lazio, 2011, Turyshev et al., 2013). The deterioration in signal return is reportedly due to lunar librations and the fading of the lunar reflectors, suspected to be caused by levitated dust (Currie et al., 2011) For example, simulations (Turyshev et al., 2013) show that the Earth's centre varies as seen from the Moon due to the eccentricity and perturbation of the Moon's orbit. As a result, the Earth's position is estimated to vary at most by 8.2 ° in longitude and 6.9 ° in latitude (Turyshev et al., 2013).

This means, during the Moon's rotation normal to the direction of the Earth, the lunar retroreflectors comprising the Apollo array temporally occur at different ranging distances from the ground-based LLR station, and thus results in a spread in the width of the returned pulse. In addition, the root mean squared error uncertainties associated with optical lunar librations were estimated to range from 24 mm for the Apollo 11 up-to about 46 - 70 mm for the Apollo 15 reflector arrays (Currie et al., 2011). In overall, the accuracy of single-shot returns on the Apollo arrays is limited to a few centimetres (Martini et al., 2012), even with the dominant observations from the A15 array across all stations. In particular, LLR stations with sub-metre aperture telescopes suffer more than telescopes with large apertures such as the

APOLLO, which can acquire thousands of single photoelectron returns to obtain one millimetre normal point (Currie et al., 2011).

The single large corner cube reflector (CCR), denoted as the Lunar Laser Ranging Retroreflector Array for the 21st Century (LLRRA-21) is expected to address the problems of optical lunar libration, such as single pulse spread due to tight CCR spacing within the array, and exposure of CCR to the accumulation of dust (Burns and Lazio, 2011; Currie et al., 2011; Martini et al., 2012). This next generation retroreflector is being developed through a joint collaboration between the University of Maryland and National Laboratory of Frascati (Martini et al., 2012) and its deployment is planned for 2019. In particular, the LLRRA-21 is based on the concept of having a series of single larger CCR of size 100 mm launched individually on the Moon surface.

Figure 9: The fabricated 100 mm second generation retroreflector (left) placed next to the 38 mm Apollo retroreflector (right) of the first generation (source: Currie et al., 2011).

The size of this CCR is larger than the current 38 mm CCRs (Figure 9) arranged within the panels of the Apollo arrays. The hypothesis for the utilisation of a single large solid CCR relative to 100 or 300 38 mm CCRs, is that the single large CCR would be unaffected by the lunar librations whereas, the current small CCRs change position with respect to the direction of the Earth due to tilting of the array by few centimeters (Martini et al., 2012). This means,

with the single large CCR the ambiguity on which CCR within the array gave a return pulse becomes irrelevant. In particular, this notion reduces single pulse error (Murphy Jr et al., 2008) and supports ranging with much shorter laser pulses to get an accurate timing of each return pulse (Currie et al., 2011). Furthermore, the LLRRA-21 would have sufficient signal strength, even for LLR stations with sub-metre aperture telescopes to provide an increased number of observations (i.e. two orders of magnitude) per month at millimetric level (Burns and Lazio, 2011).

2.2. Telescope pointing overview

The aim of pointing, is for a telescope to point toward the desired target for example retroreflectors on the Moon for a ground-based telescope. Pointing to the desired target can be described in terms of theoretical position and actual position. In particular, the theoretical position, usually expressed in azimuth (hereafter, *Az*) and elevation angles (hereafter, *El*), takes into cognizance the natural effects such rotation of the Earth, refraction, aberration and the discrepancy between Coordinated Universal Time (UTC) and Universal Time (UT1) triggered by irregularities in the rotation of the Earth. In particular, leap seconds are normally added to minimize the aforementioned discrepancy to less 0.9 seconds, and subsequently the UTC is converted into ephemeris time (ET) for computational use at the ranging station (Mulholland, 1977).

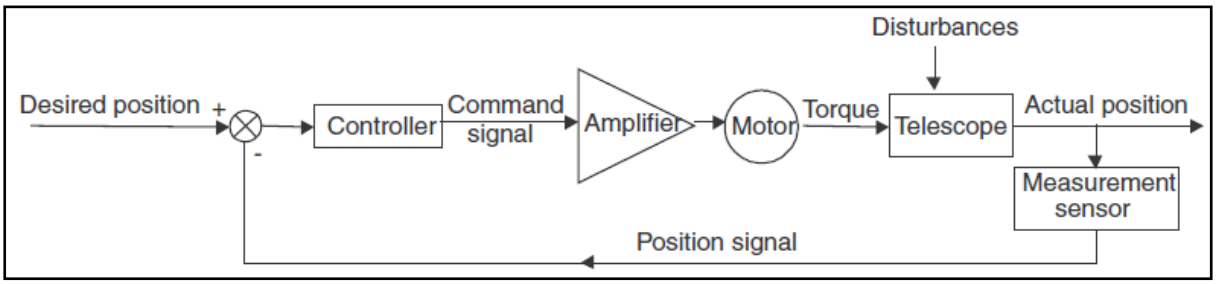

Figure 10: A basic closed-loop pointing servo system that systematically compares discrepancies between desired and actual positions. The detected discrepancy represents an error which is then fed into the drive system for correcting the initial actual position (Source: Bely, 2003)

However, as shown in Figure 10 that due to both internal and external disturbances around the telescope, the theoretical position seldom match the actual position at which the telescope is pointing, and as a result correction of the detected discrepancy takes place (Bely, 2003; Mittag et al., 2008; Zheng et al., 2012). In general, pointing errors can either be

repeatable or non-repeatable. Repeatable errors include mechanical misalignments (Greve and Mangum, 2008), gravity deformations (von Hoerner and Wong, 1975; Nkosi et al., 2016; Bergstrand et al., 2018) and thermally-induced deformations (Mittag et al., 2008; Cho et al., 2010) whereas, non-repeatable errors entail mechanical and servo errors and torque ripple in the drive motors, cable wraps as well as wind turbulence (Ukita et al., 2007). Furthermore, repeatable errors can be corrected through control systems that regularly feed corrections in a pointing model (Wresnik et al., 2007).

A widely known classical pointing model by Plaza (2001) also referred to as the 7 parameter model, is presented below to illustrate the fundamental parameters which are taken into account for telescope pointing:

$$\delta Al = Al_{\text{off}} - Al_N \sin A\, l \tan E\, l - Al_E \cos A\, l \tan E\, l - N_{\text{PAE}} \tan E\, l + B_{\text{NP}} \sec E\, l \qquad (10)$$

$$\delta El = El_{\text{off}} + Al_N \cos A\, l - Al_E \sin A\, l + T_F \cos E\, l \qquad (11)$$

where Al_{N} and Al_{E} denotes a tilt of the *Az*-axis to the north and east respectively; N_{PAE} denote the non-perpendicularity of *El* to *Az*-axis (deviation of *El*-axis from horizontal); B_{NP} denote the non-perpendicularity of the optical axis to *EL*-axis (i.e. misalignment of the optical axis to the telescope tube axis); and lastly T_{F} denote tube flexure. The errors arising from the telescope mount (axis mis-alignment), non-perpendicularity of *El* to *Az*-axis, optical collimation, and tube flexure can be corrected using the telescope (optical) model.

Various studies adopted the pointing model described ((10) and (11)) as a base method and introduced additional parameters in-order for the model to adapt to prescribed pointing performance requirements for example Mittag et al. (2008). Similar efforts are underway in HartRAO of developing the pointing model of the 1-metre LLR telescope (Combrinck, 2014).

2.3. Telescope disturbances

In general, the operational performance of the telescope (as per specifications) is as good as being able to locate, describe and mitigate the different disturbances depicted in Figure 10. In particular, ground-based telescopes such as the LLR, experience disturbances from the varying climatic environment which entails air temperature, wind, solar radiation temperature,

sky temperature and ground surface temperature (Greve et al., 2005; Mittag et al., 2008; Vogiatzis, 2010; Greve and Bremer, 2010). Additionally, interaction of these aforementioned climatic factors with the telescope often leads to heat transfer processes taking place on, and within the telescope system components, and as a result this could be detrimental to the telescope's operational performance (Cho et al., 2009; Zheng et al., 2012). In particular, the largest disturbance for ground-based telescopes is wind, especially for unhoused or open-air telescopes that are wholly exposed to the outside environment (Bely, 2003; Ukita et al., 2007).

Other disturbances are mechanical and may include friction in the telescope axes, optical misalignments (secondary mirror defocus), tube structure deformations due to thermal gradients and gravity gradient torque, and mechanical movements in the drive motors. On the other hand, space-based telescopes also undergo virtually similar disturbances (Yoon et al., 2012) described above, expect that their environment is not the same as for ground-based telescopes and therefore, some of the disturbances are negligible. For example, the gravity gradient torque especially in high orbits, and most climatic effects are negligible for space-based telescopes. However, solar radiation both direct and reflected from Earth, is a major torque for space-based telescopes (Bely, 2003). In overall, disturbances can be mitigated or compensated by means of control systems (Greve and Kaercher, 2009; Yoon et al., 2012). For the purpose of this study, the discussion going-forward is focused on ground-based telescopes in relation to the varying climatic environment (temperature) and consequent effect on telescope stability for pointing.

2.3.1. The varying climatic environment of the telescope

Over the past decades, studies have demonstrated that an optical telescope operating at an observatory site is subject to a varying thermal environment which influences the thermal behaviour of the telescope structure and its optical performance (Perry, 1943). At an observatory site, an optical telescope interacts with various climatic elements (Figure 11), thus the relative effects induced by each of these elements on the operational and optical performance of the telescope varies both spatially and temporally (Tsela et al., 2016a; Tsela et al., 2016). For example, ambient air characteristics interact with the telescope structure differently, depending on the ground topography, local altitude of the observatory site and height of the telescope structure. In particular, ambient air is characterized by temperature, pressure, humidity and density coupled with its heat capacity, heat conductivity, viscosity and

motion (Greve and Bremer, 2010). These characteristics, which can also be referred to as parameters of ambient air vary daily, monthly, yearly and seasonally; therefore their properties and profiles at a local observatory site ought to be known for robust thermal modelling of the telescope structure.

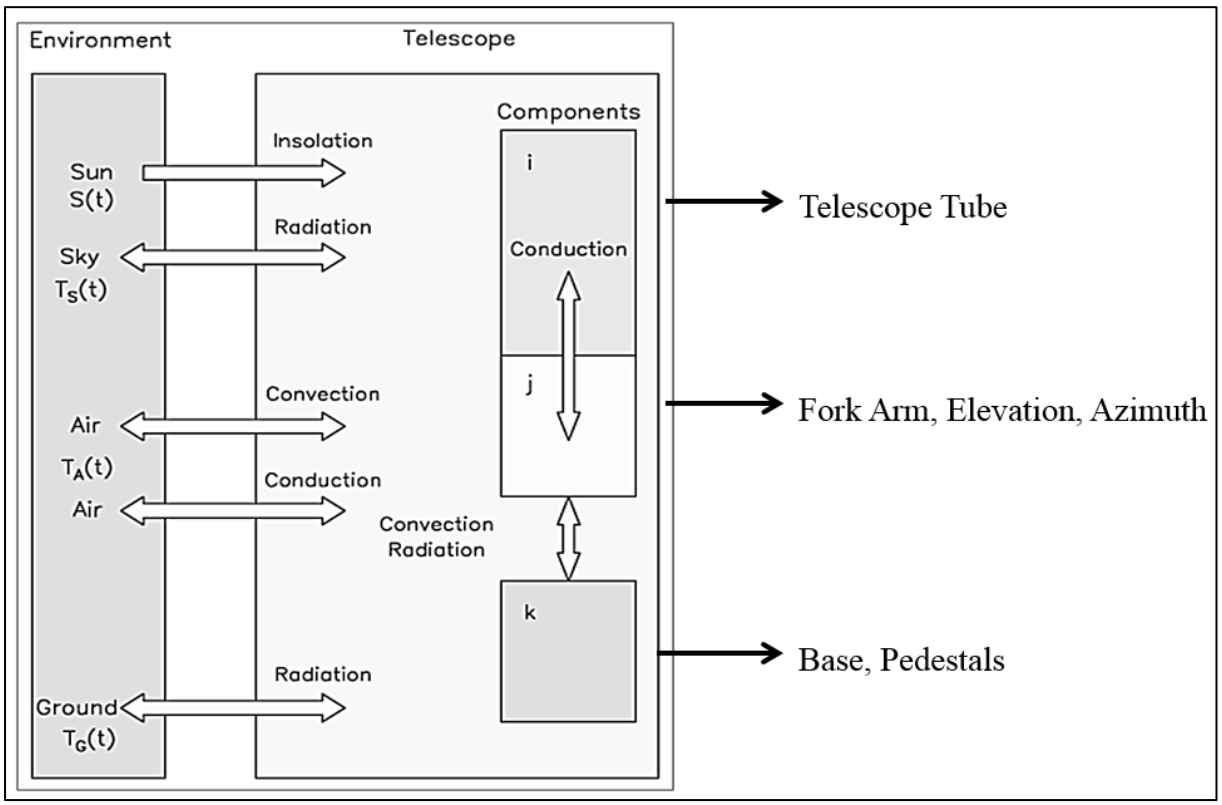

Figure 11: Illustration of the interaction between the varying climatic environment and the telescope components, coupled with heat transfer processes. Variables S_t, $T_S(t)$, $T_A(t)$ and $T_G(t)$ denotes solar radiation temperature, sky temperature, ambient air temperature, ground surface temperature respectively (Source: Greve and Bremer, 2010)

One of the basic parameters of ambient air which has been studied widely for thermal considerations of site-based open-air telescopes is ambient air temperature (hereafter, denoted T_∞) for example Baars et al. (1988); Bayley et al. (1994); Borovkov et al. (2004); Bremer and Greve (2011); Bremer and Penalver (2002); Cho et al. (2010); Cho et al. (2009); Greve et al. (2005); Mittag et al. (2008); Tsela et al. (2016a); Tsela et al. (2016); Ukita (1999); Ukita et al. (2007); Vogiatzis (2010); Vogiatzis et al. (2014); Wresnik et al. (2007); Zheng et al. (2012). Analysis of T_∞ is key for guiding the estimation of the widest possible temperature range including, the approximate times when rapid temperature changes occur at the site where the telescope is located. It has been shown that temperature variations of the telescope structural

components tend to follow or gradually respond to oscillations of T_∞ at the site. However, the rate and magnitude of temperature variations would depend (to larger extent) on the thermal properties of structural components as well as the overall size of the solid telescope structure (Tsela et al., 2016). Therefore, the relationship between T_∞ and telescope thermal response at the site ought to be investigated and well understood in-order to determine: (i) the extent of influence that T_∞ has on the specified operational temperature range of critical components such as optics, detectors and supporting structure, (ii) effect on the tube stability for achieving the pointing accuracy requirement of the telescope, (iii) thermal time constants of the telescope components, and (vi) options for developing a thermal dynamic model for correcting the temperature variations.

As shown in Figure 11 that solar radiation injects heat to a telescope. Solar radiation is a major natural heat source for open-air ground-based telescopes (Greve and Bremer, 2010) and can provide heat of about 1000 W/m^2 at ground level on a clear day (Pantic et al., 2010; Çengel and Ghajar, 2011). The solar radiation interaction (Figure 11) is initiated by the radiation incident on the telescope surface area, and thereafter the telescope surface area would lose portion of the incident radiant energy by emission and reflection as follows:

$$\dot{\boldsymbol{Q}}_{\boldsymbol{i}} = \boldsymbol{A}_{\boldsymbol{i}}(\boldsymbol{\varepsilon}_{\boldsymbol{i}}\boldsymbol{E}_{\boldsymbol{bi}} + \boldsymbol{\rho}_{\boldsymbol{i}}\boldsymbol{G}_{\boldsymbol{i}} - \boldsymbol{G}_{\boldsymbol{i}}) \tag{12}$$

where $\dot{Q}_i$ represent the net rate of radiation heat transfer, $\varepsilon_i E_{bi}$ is the blackbody emissive power of surface area ρ_i is the proportion of reflected radiation by A_i, and G_i denote the incident radiant energy on A_i.

The effect of radiation emitted by the Sun (Figure 11) during day-time on the telescope structure varies depending on the orientation of the telescope; paint usage and use of the enclosure i.e. dome. For example, a telescope receiving direct radiant energy would have uneven heat distribution across its structural surfaces i.e. due to some surfaces not exposed to the sun directly. This may cause thermal expansion of the surfaces and possible optical misalignments which collectively may affect the operational temperature range of critical components, telescope pointing stability and optical performance. However, the detrimental effect of the radiation emitted by Sun can be mitigated, especially for open-air ground-based telescopes by use of white paint such as Chemglaze A276 (Greve and Bremer, 2010) and

double-layered structural designs for insulating critical components (Tsela et al., 2016a). Furthermore, placement of the telescope in an enclosure such as a dome, can potentially eliminate the radiation effect (particular during day-time) in a way that each of the telescope structural surfaces is isothermal (Greve and Bremer, 2010).

In addition to the Sun's emitted radiation, wind also poses as a large disturbance for ground-based telescopes. Wind disturbance is best mitigated when the telescope is placed in an enclosure (Figure 12); otherwise exposure to winds of approximately 2 to 5 ms^{-1} could shake the telescope and cause pointing instability (Medwadoski, 1981; Bely, 2003).

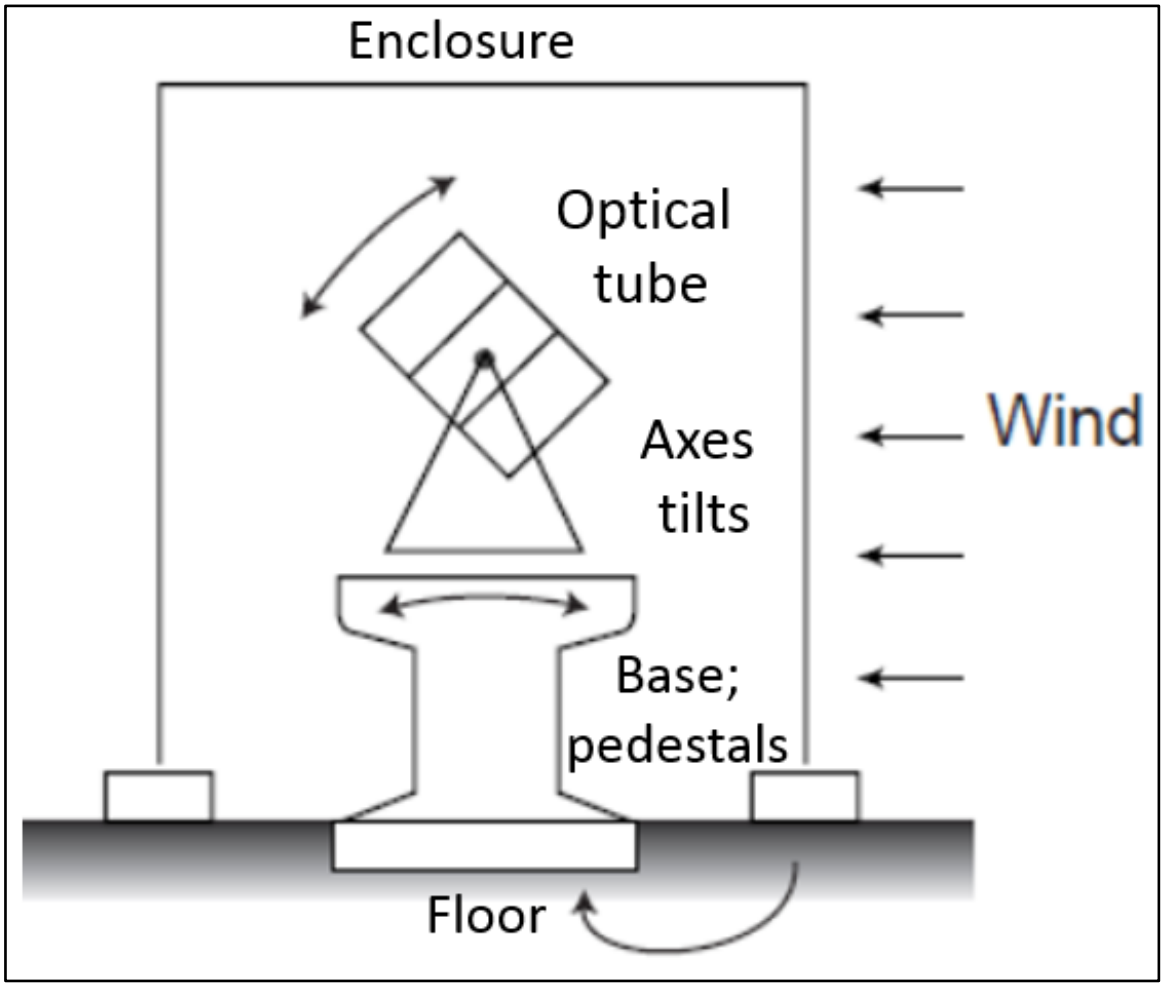

Figure 12: Wind interaction with the telescope enclosure (observatory building), whereby the telescope is protected. However, this interaction may cause the building to shake, and consequently the telescope through vibrations on the ground and base/ pedestals (Source: Bely, 2003)

Wind has effects on the telescope structure, optical mirrors, and telescope piers or pedestals (Figure 12). The effects can be categorized as static or dynamic. In particular, a static wind effect on a certain telescope surface component has the following load:

$$F = C_{D\rho}\frac{v^2}{2}A \tag{13}$$

where C_D denote the drag coefficient (based on the geometry of the telescope body), ρ denote air density, v denote wind speed and A is the telescope's surface area normal to the wind direction (Bely, 2003). Equation (13) typically describes a force (F) generated by a constant wind, assuming a laminar flow incident on the telescope components i.e., cylindrical tube carrying the optical mirrors.

Whereas, a dynamic wind effect would be given by:

$$f = \frac{Str \times v}{Td} \tag{14}$$

where Str denote the Strouhal number (approximated for different structural shapes), Td denote the transverse dimension of the element and, v denote wind speed (Bely, 2003).

Equation (14) typically describes pressure exerted by swirling vortices due to vortex shedding around the telescope surfaces. These vortices have a non-steady flow component and may result in large amplitude oscillations (Çengel and Ghajar, 2011). Above all, information pertaining wind speed, wind direction and air density at the location of the telescope, consist of pivotal inputs in the modeling of convective heat transfer between the ambient air and telescope surfaces (Greve and Bremer, 2010).

Other interactions that are important for thermal consideration of the telescope include ground and sky temperatures (Figure 11). It is known that the telescope is radiatively coupled to the ground and sky (Greve and Bremer, 2010). For example, for a given ground, it has unique thermal properties including emission and absorption coefficients at infrared wavelengths; and as result the ground (where the telescope is based) would experience

warming during the day and radiate the heat toward the telescope's light of sight into the sky during night-time. Similarly, due to temperature difference between the telescope components and sky, the telescope would interact with the sky radiatively; hence radiative cooling of the telescope toward the sky. Furthermore, relative humidity can be used to determine sky temperature (i.e. low humidity ~ dry weather conditions or high humidity ~ wet weather conditions) to which the telescope is radiatively coupled (Greve and Kaercher, 2009).

2.3.2. Seeing effects due to temperature fluctuations

One of the effects which has received considerable attention is mirror seeing mainly as a consequence of temperature gradients between the optical mirror surface and T_{∞}. The same effect may also occur when temperature differences are induced in the mirror. As the air temperature fluctuate on a daily basis, the mirror temperature (depending on its size and thickness) may not change simultaneously with T_{∞} around it, and therefore could remain warmer or colder than ambient air for a considerable time period. The temperature difference between the mirror and its surrounding triggers a transfer of energy by convection, whereby a thin turbulent layer occurs a few millimeters above the mirror surface which affects the optical path (Greenhalgh et al., 1994).

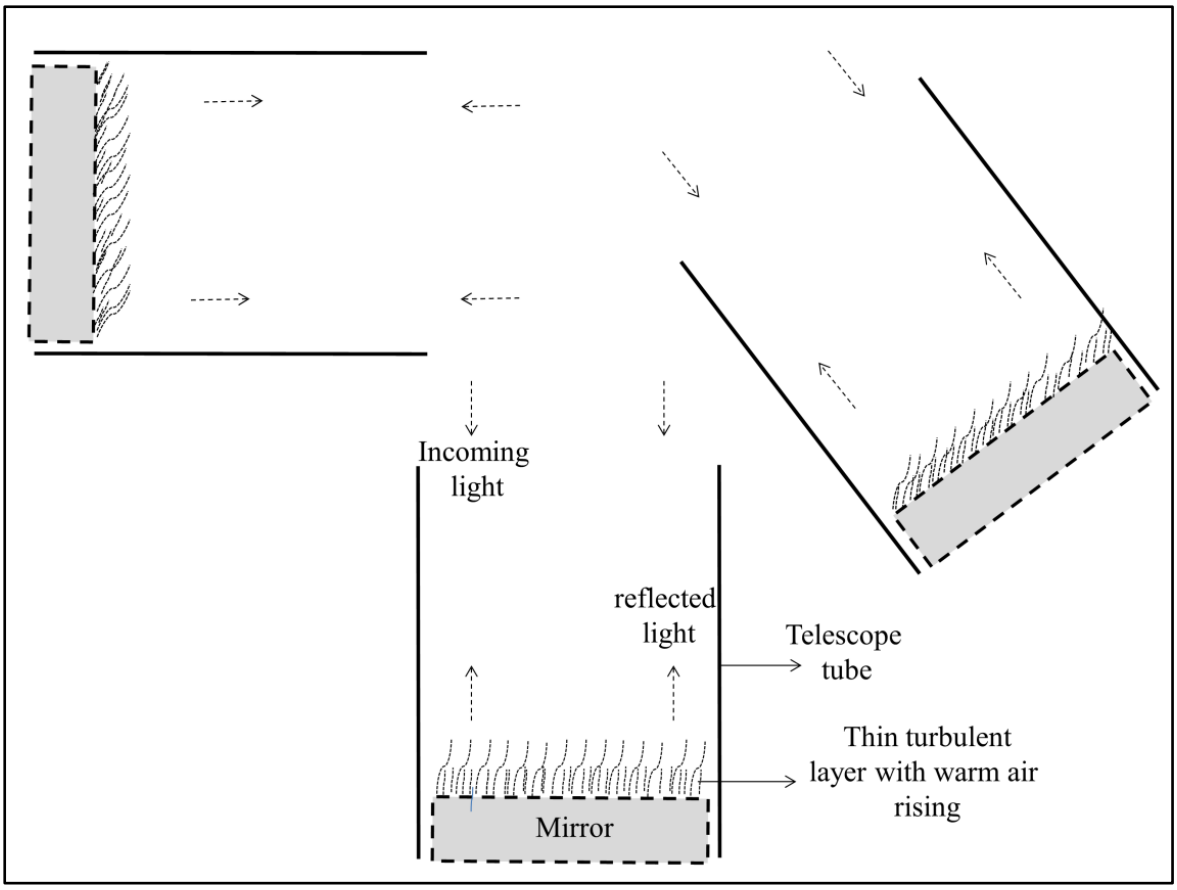

Figure 13: Hypothetical telescope mirror within a tube at different inclinations showing a layer of uprising warm air as a result of natural convection thus leading to mirror seeing. In all three mirror inclinations, according to Lowne (1979), the worst mirror seeing condition occurs when the mirror is facing horizontally while the warm air rises in the vertical light path.

For example, the uprising warm air from the mirror surface along the optical path or telescope's line-of-sight at different inclinations (Figure 13) is likely to be detrimental to image quality for astronomical observations (Lowne, 1979), divergence angle (Zheng et al., 2012) and refractive index (Bohannan et al., 2000; Saydi et al., 2014; Cui et al., 2016) of the outgoing beam for laser ranging telescopes. A solution to address mirror seeing is for the mirror temperature to reach thermal equilibrium with the surrounding T_∞ through either natural or forced ventilation of the mirror. Natural ventilation allows the mirror temperature to adjust itself by tracking T_∞ changes through free air convection. While this approach may produce desirable results particularly for small telescope mirrors however, for large mirrors coupled with their long thermal time scales, natural ventilation may not produce timely temperature adjustments on the mirror with respect to rapid changes of T_∞. As a result, experiments have shown that mirror seeing rapidly diminishes when the mirror undergoes forced ventilation (Zago, 1997).

2.3.3. Analysis strategies for telescope's thermal variations

Ground-based telescope utilized for laser ranging observations of space-based targets at sub-centimetre level accuracy can suffer from structural and optical deformations induced by thermal variations. These deformations are known to be detrimental to the telescope tube displacements and defocusing, thereby affecting pointing performance. It is an experimental fact that classical telescopes built from materials such as aluminum and steel are subject to varying dimensional changes due to external and internal temperature changes (Mittag et al., 2008; Murphy Jr et al., 2008; Vogiatzis et al., 2014). Therefore, analysis of temperature variations and induced deformations of the telescope's critical components, coupled with their consequent effect on the overall pointing error budget is important for (i) a thorough exploration of the extent of their influence on the telescope performance, and (ii) the selection of suitable control measures (that can be either passive or active), in-order to mitigate the temperature variations (Baars et al., 1988; Énard et al., 1996; Bremer and Penalver, 2002; Atwood and O'Brien, 2003; Ukita et al., 2007; Tsela et al., 2016a).

One of the key factors in the operational and optical performance of a ground-based optical laser telescope, is thermal analysis of the telescope structure and associated optics, based on the thermal properties of component materials and their interaction with the environment mainly through conventional heat transfer mechanisms (Bely, 2003, Greve and Bremer, 2010; Çengel and Ghajar, 2011). The relative effects induced by the heat transfer mechanisms i.e. conduction, convection and radiation on the performance of the telescope vary both spatially and temporally (Cho et al., 2010; Bremer and Greve, 2011; Vogiatzis et al., 2014).

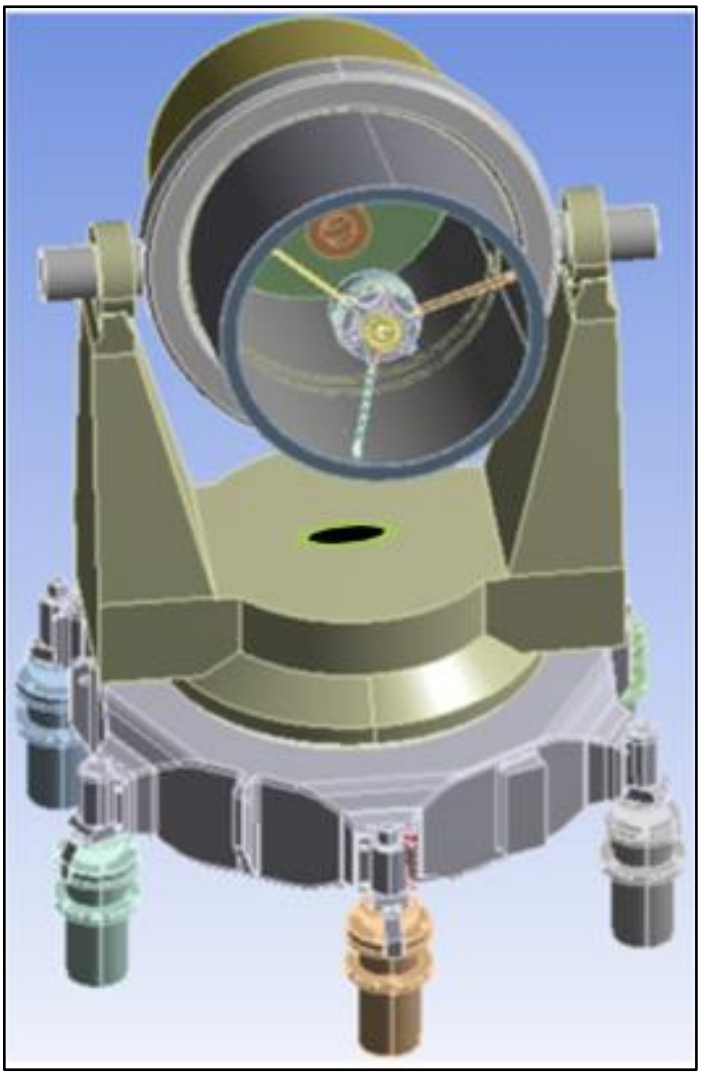

Figure 14: A 3-dimensional model of the 1-metre aperture Lunar Laser Ranging telescope at the Hartebeesthoek Radio Astronomy Observatory displayed in ANSYS software.
Credit: The original scaled and highly detailed technical drawing of the tube and mount was done by Wikus Combrinck.

Usually locally-parameterized temperature control systems are put in place to regulate the temperature of critical components of the telescope, so as to ensure (i) they are kept within their design temperature range, (ii) they reach thermal equilibrium and (iii) maximum telescope scientific performance for example Murphy Jr et al., (2008).

Telescope thermal variations caused by T_{∞} are usually analyzed using three widely known methods. The first method entails simulating thermal variations using Finite element (FE) modelling software on a geometrically accurate three-dimensional model of the telescope for example. Figure 14 coupled with corresponding thermal properties of the component materials and typical spatio-temporal climatic parameters (Ukita, 1999; Greve and MacLeod,

2001; Cho et al., 2010; Vogiatzis et al., 2014; Tsela et al., 2016a; Tsela et al., 2016b; Greiner et al., 2018; Wang et al., 2018). Furthermore, the reliability of thermal simulation results would depend to a large extent on the defined boundary conditions, correct parameterization of thermal loads which include for example T_{∞}, film coefficient of air temperature (hereafter, denoted *h*) and material thermal properties (Vogiatzis et al., 2014). After all, simulation results may have to be validated using real measurements for a reliable judgment on their accuracy.

The second method is infrared thermography which uses a camera to detect photons of thermal infrared radiant energy exiting the target object, in the two primary thermal infrared (optimal atmospheric transmission) windows i.e. 3 - 5 μm and/or 8 -14 μm. The radiant energy is converted to temperature and thereafter an image of the object's (i.e. telescope's) temperature distribution is displayed (Jensen, 2009; Greve and Bremer, 2010; Yang and Chen, 2011; Tantele et al., 2018).

Lastly, the third method involves installation of several temperature sensors on strategically identified locations throughout the telescope's critical components. Thereafter, the acquired temperature measurements can be fed into a thermal dynamic model for timely monitoring, prediction and correction of the telescope's thermal variations (Ukita, 1999; Bremer and Penalver, 2002; Greve and Kaercher, 2009; Mittag et al., 2008; Murphy Jr et al., 2008; Pisanu et al., 2010; Tsela et al., 2016b). For the current study, the first and last methods were adopted in order to model the thermal behaviour and related distortion dynamics of the HartRAO LLR composite structure for possible impact on pointing. In particular, this entailed (i) analysing the extent of influence of T_{∞} at the HartRAO site on the thermal behaviour of the LLR telescope structure and its mirrors (Tsela et al., 2016a; Tsela et al., 2016); (ii) proposing a thermal model for monitoring thermal variations and related deformations of the LLR telescope composite structure (Tsela et al., 2016b); and (iii) quantifying the extent of thermally-induced tube displacements during day- and night-time.

Several studies have used the first method described above for the analysis of thermal variations and related deformations, coupled with their consequent effect on the pointing performance of ground-based optical telescopes. For example, Cho et al. (2010) reported structural thermal variations due to varying T_{∞} on the thirty metre telescope (TMT) ranging between 0.01 °C and 7.32 °C corresponding with thermally-induced deformations ranging

between 141 μm and 993 μm respectively; and thus these findings had a temporal impact on the telescope pointing with offsets ranging from 0.7 to 1 arcsecond (hereafter, denoted ″) at selected elevation angles (Vogiatzis et al., 2014). Mittag et al. (2008) analysed the influence of T_∞ on the pointing of the Hamburg robotic optical telescope for 16 nights (with temperatures ranging from -6.4 ºC to 25.8 ºC) and found that thermal expansion of component materials primarily triggered misalignments of the optical axis within the tube. This expansion was responsible for the observed peak azimuth and elevation offsets of 40″ and 10″ respectively. Furthermore, Tsela et al. (2016a) simulated the thermal behaviour of the LLR optical tube assembly in HartRAO and found structural thermal variations of about 1 °C and consequent total deformations that varied between 2.9 and 40.7 μm. These results were due to T_∞ at the site which varied between 9 and 23 °C on a non-windy, cloud-free and winter day; and therefore suggests potential tube displacements which ought to be investigated for their influence on the pointing. In general, such simulation-based studies gives an indication of the extent of influence of T_∞ on the thermal behaviour of the telescope, as well as, the extent of thermally-induced deformations which may cause displacement/ misalignment of components (for example telescope mount axes, tube and optical axis within the tube) critical for pointing performance. This information has significant implications for exploring options for developing a thermal dynamic model to monitor thermal variations, and determining the amount of correction needed to be fed into a telescope pointing model to counteract thermally-induced pointing offsets.

In particular, the third method described earlier of installing sensors on the telescope's critical components becomes more relevant, if real-time measurements of temperature (and structural deflections) are to be acquired for monitoring and correcting for thermal variations and their induced pointing offsets (for example Bremer and Penalver (2002); Greve et al. (2005); Murphy Jr et al. (2008); Greve and Kaercher (2009); Tsela et al. (2016b)). This third method often incorporates algorithm-driven ventilation procedures also called active control systems, for adjustable cooling and thermal stabilization of critical systems. By far, this method has been tested over the years to be reliable in providing detailed real-time temperature monitoring and modeling for prediction and correction thermally-induced pointing errors.

For example, Greve et al. (2005) mounted 156 thermal sensors on the Institut de Radioastronomie Millimétrique (IRAM) 30 m telescope for temperature monitoring and prediction of structural deformations from FE calculations (see also Bremer and Penalver

(2002)). As a result, the study predicted deformations with an average accuracy of 0.03 mm coupled with pointing corrections in *El* and *Az* accurate to about 1″. Further, a similar approach was adopted by Antebi et al. (1998) for the 50 m Large Millimeter Telescope (LMT) and reportedly found residual surface deformations and pointing root mean squared (RMS) errors of 13.5 μm and 0.5″ respectively, which were acceptably below the specified RMS error budgets of surface deformations and pointing accuracy of the LMT telescope. Pisanu et al. (2010) demonstrated strong correlations between the antenna pointing errors and thermally-induced deformations on selected structural components of the Medicina 32 m telescope, based on measurements acquired using inclinometers, temperature transducers and a non-contact laser alignment system, in order to guide development of a robust mathematical model for instantaneously correcting the thermal pointing errors. In addition, virtually similar studies with varying model outputs have been conducted for various radio and optical telescopes (for example Bayley et al. (1994); Lamb and Woody (1998); Borovkov et al. (2004); Ukita et al. (2007); Greve and Mangum (2008); Mittag et al. (2008); Murphy Jr et al. (2008); Vogiatzis (2010); Mészáros et al. (2014)).

Furthermore, Vogiatzis et al. (2014) presented a thermal model founded by Cho et al. (2010) that utilize FE analysis, Merit function routine and optical sensitivity matrix for varying thermal boundary conditions to allow for the monitoring of diurnal temperature variation and related deformations of the TMT structure, as well as deriving the corresponding pointing error during operation. More recently, Tsela et al. (2016b) described a thermal model based on planned installations of 136 resistant temperature detectors (RTDs) on selected FE nodes of the HartRAO LLR telescope. The model is expected to monitor thermal variations and related deformations of the LLR telescope composite structure, so as to compensate for thermally-induced misalignments that lead to pointing errors for the LLR telescope. Tests and calibration of RTDs for accurate temperature measurements have been reported using a two-way separable mockup tube structure (Tsela et al. 2016).

With regards to optimal thermal modeling of a telescope, it is worth mentioning that a major challenge is to develop solution strategies that can actively control i.e. mitigate through forced air, and stringently constrain the thermal variations at approximately 1 °C (Murphy Jr et al., 2008) especially for the optical tube assembly including its mirrors in an open-air environment. Relative to active control, passive control measures can also be adopted to constrain thermal effects arising from heat transfer mechanisms. These measures entail coating

and insulating the telescope surface components, and a telescope structure design comprising a combination of near-zero coefficient of thermal expansion (CTE) material components, which would either allow minimal thermal effects and/or cancel the thermal effects through self-adjustment of the telescope optical elements and structure (Atwood and O'Brien, 2003; Bely, 2003). However, passive control measures may not yield desirable results in particular timely self-adjustments of the telescope structure and optics, under extreme and rapid ambient climatic changes for example Ukita (1999).

2.4. Concluding remarks

This chapter contains the basics of the LLR technique and scientific contributions emanating from the LLR measurements. This was followed by a discussion on the chronological establishment of observatories or stations equipped with lunar ranging capabilities across various parts of the world. Additionally, relative performance of in-terms of ranging accuracies by each of the LLR stations was also discussed, including the biased geometry network of LLR stations globally. Key to the relative performance of ground-based optical telescopes such as the LLR, this chapter acknowledged various disturbances that could influence the pointing performance of open-air optical telescopes operating at an observatory site.

These disturbances were identified to be mainly as a result of, the varying climatic environment, mechanical misalignments, gravity- and thermally-induced structural deformations. Furthermore, the effect of these disturbances on the operational performance of site-based open-air telescopes was discussed. This was followed by a discussion on various solution strategies particularly on the analysis of thermal variations in-order to determine: (i) the extent of influence ambient air temperature has on the specified operational temperature range of critical components such as optics, detectors and supporting structure, (ii) effect on the tube stability causing displacements detrimental to pointing accuracy, (iii) thermal time constants of the telescope components, and (vi) options for developing a thermal dynamic model for correcting the temperature variations. This review literature show consensus on that, the severity of disturbances encountered by ground-based telescopes vary depending on the observatory site characteristics.

Therefore, this background laid a foundation for the current research study to (i) investigate the extent of influence of varying ambient air temperatures at the HartRAO site on the thermal behaviour (thermal response times and deformations) of the first-ever LLR telescope in the Southern Hemisphere, (ii) present a thermal model for monitoring thermal variations and related deformations of the LLR telescope composite structure, (iii) quantify the extent of thermally-induced tube displacements during day- and night-time, so as to inform efforts to determine the amount of correction needed to be fed into the LLR telescope steering and pointing model (Combrinck, 2014) to counteract thermally-induced pointing offsets. Lastly, it is worth mentioning that portions of the background literature presented in this chapter, especially in sections 2.2 and 2.3 have been published in journal papers by the current author (Tsela et al., 2016a; Tsela et al., 2016b; Tsela et al., 2016).

Chapter 3: Materials and Methods

3.1. Description of the HartRAO LLR

HartRAO is a national facility of the National Research Foundation of South Africa (Figure 15) and operates the following instruments for geodetic and astronomical observations: the 26 m and 15 m radio telescopes, National Aeronautics and Space Administration (NASA) MOBile LASer 6 (MOBLAS-6), SLR, Russian satellite ranging system «Sazhen-TM+OWS», Global Navigation Satellite Systems (GNSS) base-station receiver, as well as a gravimeter, seismometer and several weather stations on site. The co-location of these instruments enable precise orbital measurements and small geometrical errors for computing geodetic and astronomical parameters within the global geometry network (Combrinck, 2011; Munghemezulu et al., 2016).

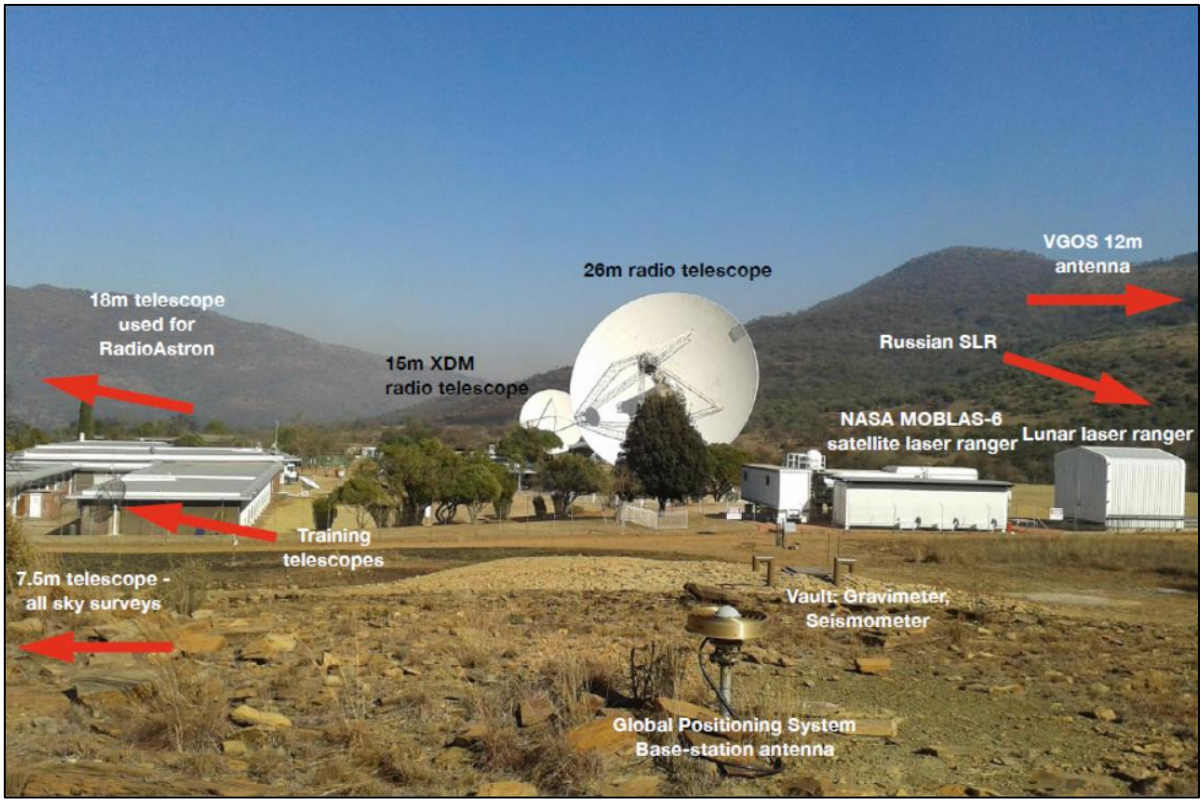

Figure 15: Overview of geodetic and astronomical instruments based at the Hartebeesthoek Radio Astronomy Observatory (HartRAO) located north of Krugersdorp in South Africa. This is the only observatory in the Southern Hemisphere where such instruments can be found co-located in one site. In particular, the Lunar Laser Ranging enclosure can be seen on the far middle right. Picture credit: Aletha de Witt, HartRAO researcher.

The LLR telescope (Figure 16) which is located at HartRAO was previously used by OCA for Satellite Laser Ranging (Combrinck, 2011). Various components ex-OCA telescope are currently being revamped for integration at HartRAO, coupled with the installation of modern instrumentation and development of subsystems with LLR capability such as: laser and optics (Botha, 2016; Ndlovu et al., 2016; Nkosi et al., 2016), timing (Munghemezulu et al., 2018), pointing and control (Nickola and Combrinck, 2011; Combrinck, 2014) as well as thermal monitoring (Tsela et al., 2016b).

Figure 16: The ex-French 1-metre aperture Lunar Laser Ranger (LLR) stationed at Hartebeesthoek Radio Astronomy Observatory. The integration of other components such as the inner tube components is still in progress at HartRAO; hence are not shown.

This telescope is a typical Cassegrain system comprising various component materials such as, a concave 1 m primary mirror and convex 0.3 m secondary mirror mounted on the spider assembly, and a double layered tube structure for thermal insulation (Figure 17). In

principle, the outgoing/incoming laser light to/from the retroreflectors mounted on the lunar surface will be transmitted/received through the primary mirror which is preferred for the sake of better laser light collimation (Combrinck, 2011).

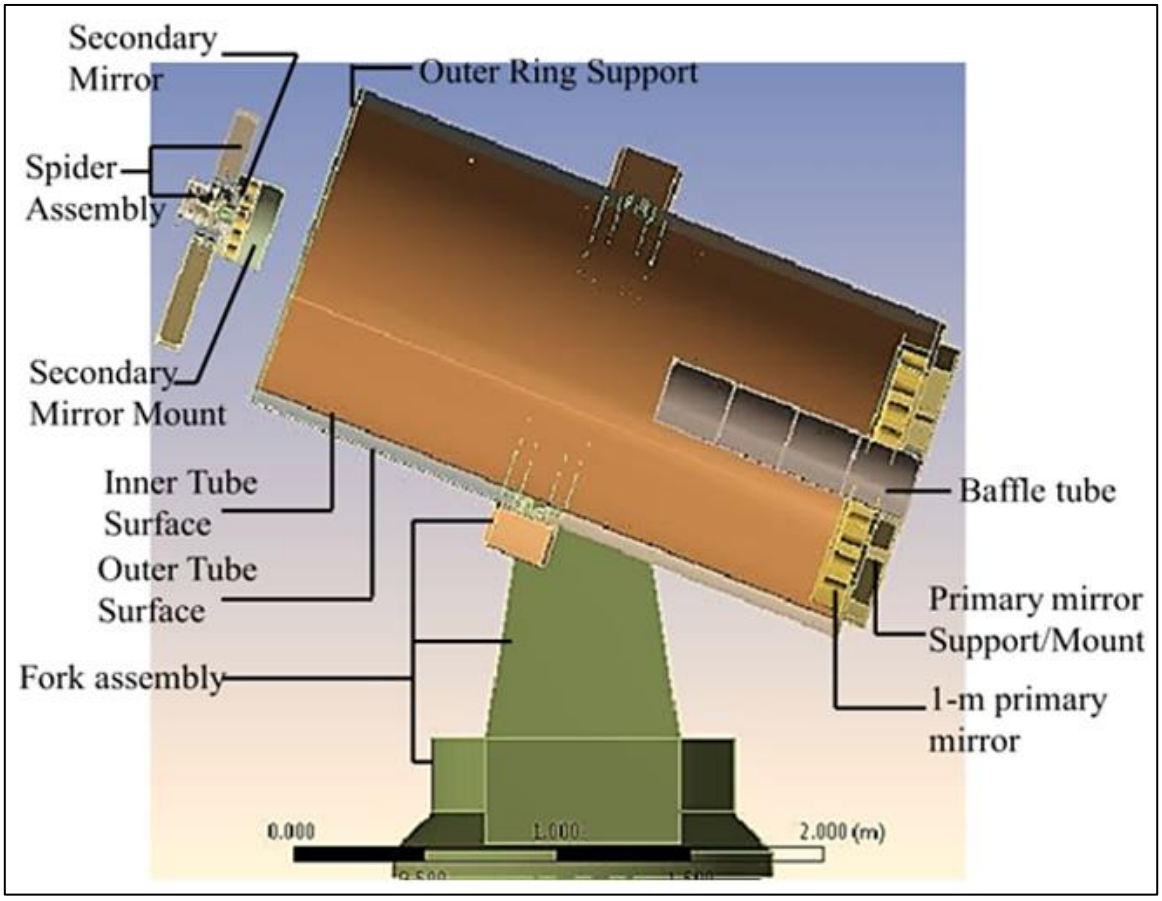

Figure 17: Cross section and side view of the Lunar Laser Ranger at HartRAO indicating the material components considered for thermal analysis in this study. Note: the spider assembly is shown in exploded view for legibility. This CAD model was considered in this study to illustrate the various surface-component materials and their respective thermal properties. The model does not include the telescope base i.e., pedestal and feet material components.

3.1.1. The LLR Telescope foundation

A temporary telescope foundation for the LLR telescope has been set-up at HartRAO (Figure 18). The set-up comprises the massive steel foundation which is important for the stability of the telescope structure and conducting pointing tests (Combrinck, 2011); and further facilitates the process of removing the telescope to the appropriate site, described in Nickola et al. (2011). The telescope is housed in a run-off enclosure (Figure 18), such that when not in operation and/or during unfavourable weather conditions it can be enclosed. The mobile enclosure of the LLR telescope takes approximately 2.5 minutes to open and move away, and

can be disassembled at the time of re-location (Combrinck, 2011). Detailed information on the telescope mobile enclosure and the LLR control centre can be found in Combrinck (2011) and Combrinck and Botha (2014).

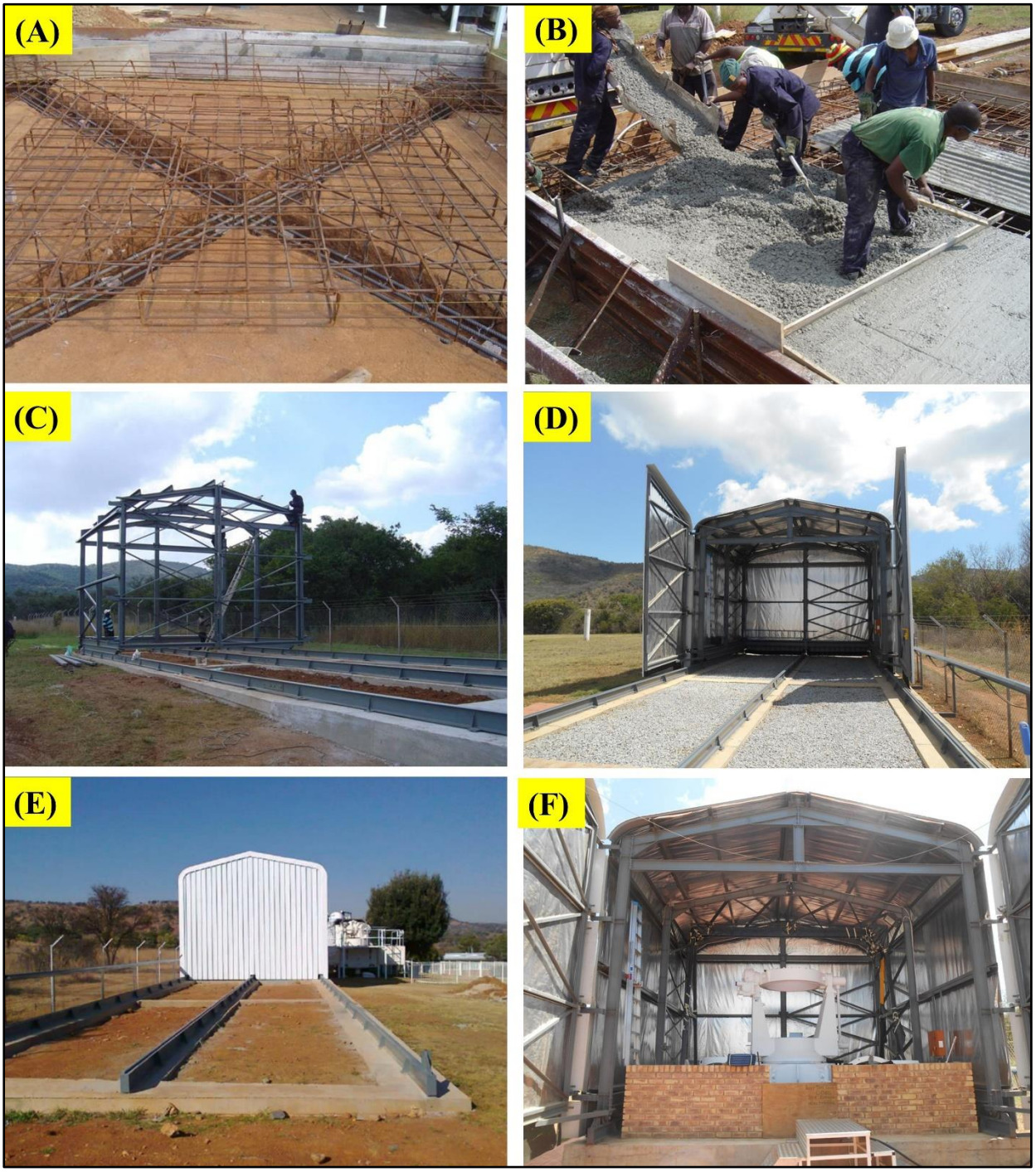

Figure 18: Development of the LLR telescope foundation which include, the massive steel foundation key for the stability of the telescope structure and pointing tests (A), 30 m^3 of concrete to produce a steel reinforced concrete floor (B), telescope mobile enclosure or housing designed to run-off the steel tracks (C, D and E), and the housed LLR telescope installed on its foundation (F). Picture credit: Ludwig Combrinck.

3.1.2. LLR performance requirements

The LLR telescope is expected to achieve pointing accuracy at 1 arcsecond level with estimated photons of 3-4 per minute (detected at 532 nm wavelength) based on the 130 Millijoule (mJ), 80 ps pulse width system (Table 2). Detailed explanation of these requirements can be found elsewhere (Combrinck, 2011; Combrinck and Botha, 2014; HartRAO, 2005; Botha, 2016). The future goal of this study is to have a dynamic thermal model that can contribute toward the attainment of proposed performance requirements (Table 2) particularly pointing accuracy (Combrinck, 2014). To date, a prototype pointing model operated on a 125 mm dual refractor testbed telescope (located in a closed, fairly stable environment) achieved RMS error values at the 0.5 arcseconds level (Combrinck, 2014). It will be interesting to observe the extent of variation of the achieved values, particularly when the pointing model is tested on the actual LLR telescope which is exposed to the varying climatic environment. For this reason, the research study (1) analyzed the relative thermal response times and deformations of the telescope structure and optics due to T_{∞} at the HartRAO site, (2) analyzed the extent of thermally-induced tube displacements during day- and night-time, and (3) proposed a theoretical, thermal dynamic model for monitoring thermal variations and thermally-induced deformations of the telescope structure and optics; with the aim (future goal) of determining the amount of correction needed to be fed into the telescope pointing model (Combrinck, 2014) to counteract thermally-induced pointing offsets.

Table 2: Summary of the selected pointing and optical constraints and requirements of the Lunar Laser Ranging optical telescope at the Hartebeesthoek Radio Astronomy Observatory. The two columns do not relate to each other.

Pointing related	Optical related
Pointing accuracy: ≤ 1″	Transmit/ Receive efficiency: > 0.9 / > 0.8
Tracking accuracy: < 1″	Estimated photons: 3-4 per minute based on the proposed 130 mJ, 80 pico-second pulse width system and an atmospheric seeing condition of 2-3″
Maximum slew rate in azimuth and elevation: ~3 degrees per second	Return Detector: Avalanche photo diodes with 100-200 micron aperture and detection efficiency of ~50%. Single photon mode with a wavelength of 1064 nm ;
Position resolution: <0.5″;	Start detector Fast (< 50 Pico seconds) photo diode detecting at 532 nm wavelength. Single or multiphoton mode.
Range precision: 1 mm	Effective focal length: 7.6 m

3.2. Description of materials used

3.2.1. 3-D CAD model of the telescope

Figure 17 discussed earlier, presents a 3-dimensional geometrical model of the telescope prepared in SolidWorks (Onwubolu, 2013). This model, coupled with its thermal properties (Table 3), was used in this study to perform thermal and structural simulations in ANSYS software. The material components of the computer-aided design (CAD) model shown in Figure 17 are deemed sensitive to T_{∞} and play an important role for pointing accuracy (Perry, 1943). In addition, the thermal properties (Table 3) related to each component material play an important role in the correct parameterization during thermal and structural analyses of the telescope. In particular, the analyses were two fold i.e. first, only the optical tube assembly was considered (Tsela et al., 2016a) and, the second analysis entailed the integrated telescope (Tsela et al., 2016). Given the thermal properties related to each component material, it is suspected that, this could have thermal variations and related deformations of varying magnitudes across the telescope structure, in relation to the varying ambient air temperatures at the HartRAO site.

Table 3: A succinct summary of selected thermal properties of the Lunar Laser Ranging telescope's component materials (Green, 2008).

	Zerodur	**Aluminium T6 7075**	**Low carbon steel 1023**
	Primary/Secondary mirror	**Inner/Outer tube surface; Baffle tube**	**Primary mirror mount/support; Fork assembly; Spider assembly; Outer ring support**
Thermal Conductivity *k* [*W/m.K*]	1.46	130	50
Specific heat C_p [*J/kg.K*]	820	1047	490
CTE 10^{-6} K^{-1}	0.10	24.4	11.7
Density p [kg/m^3]	2500	2800	7850

From Table 3 the components with lower thermal conductivity (*k*) and CTE such as the mirrors and fork assembly (comprising fork arms, azimuth and elevation mounts) might result in slow thermal response times (Tsela et al., 2016) and slow internal equalization of thermal variations coupled with very small distortions (Jedamzik et al., 2010) relative to other components; particularly with respect to HartRAO site-based air temperature profiles which are on average broadly estimated in the range 0 °C to ±35 °C (Tsela et al., 2016a). It is therefore important to simulate the extent of these variations with the highest possible accuracy in-order to guide the development of a dynamic thermal model (Tsela et al., 2016b).

3.2.2. Finite element model of the telescope

In this study, the FE model of the 1-metre LLR optical telescope was generated in ANSYS (Figure 19) which considered appropriate element types for the varying structural shapes of the components; such as the 3-dimensional 4-noded tetrahedrons and 8-noded hexahedrons for the fork assembly and tube respectively (Tsela et al., 2016b). The FE model

of the telescope (Figure 19) had a total of 423097 nodes and 269307 elements across all the considered components (Table 4). Only a relatively small number of nodes regarded as thermally important were selected for the mounting of temperature sensors (Table 4) since, the installation of temperature sensors at all FE nodes may not be practical (Bremer and Penalver, 2002; Greve et al., 2005).

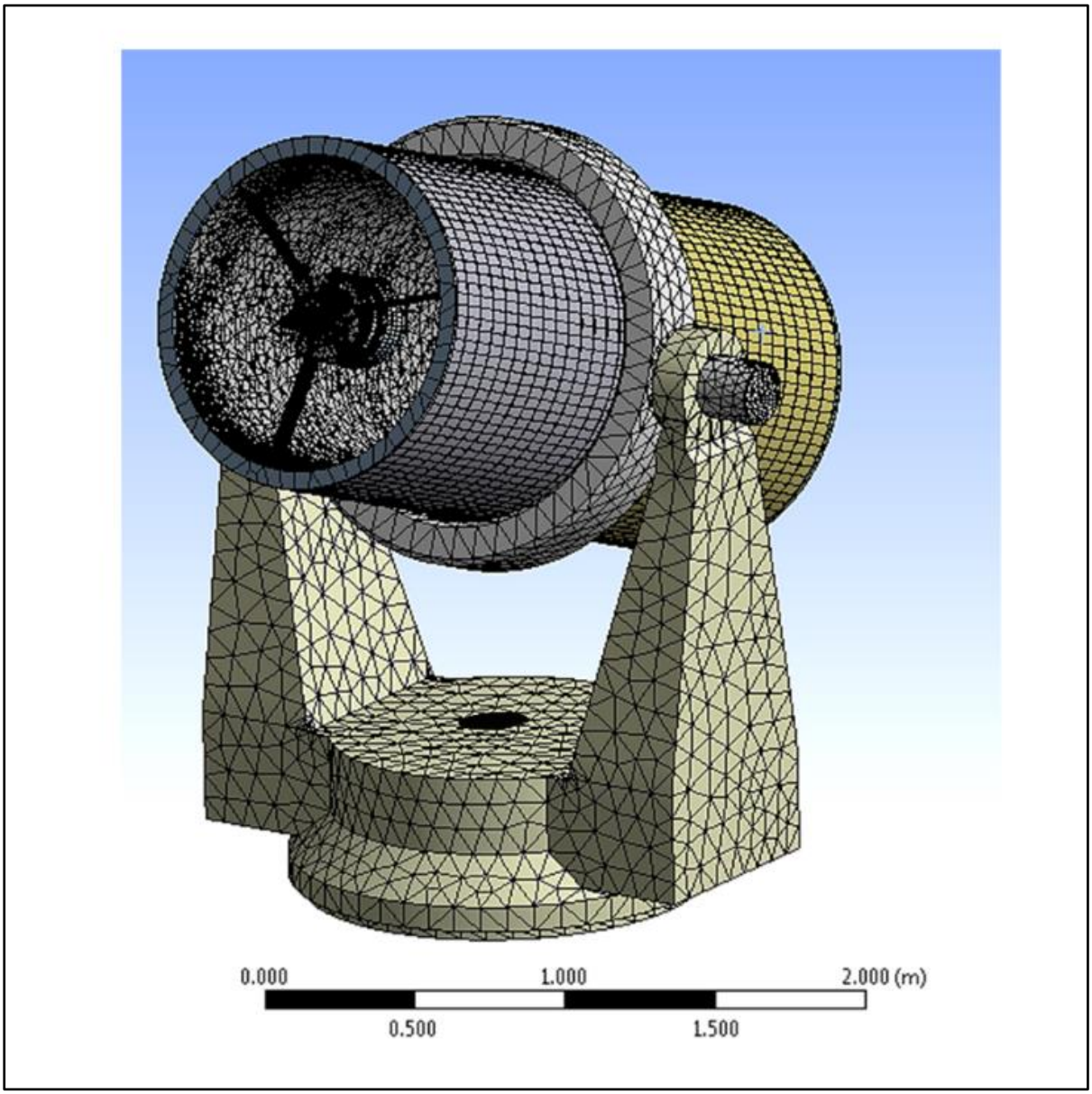

Figure 19: Finite element model of the integrated telescope containing the fork assembly (i.e. fork arms, azimuth and elevation mounts), double layered tube, primary mirror support (not visible), spider assembly, secondary and primary mirrors. The model used for analysis does not include the pedestals and feet.

Table 4: The total number of nodes and elements from the Finite element (FE) model of the Lunar Laser Ranging telescope and the selected number of FE nodes considered for mounting the temperature sensors.

Telescope component	**Number of nodes (*N*)**	**Number of elements (*E*)**	**Selected number of nodes (*K*) with corresponding sensors (*T*) = T_K**
Outer tube surface	5184	672	8
Inner tube surface	28960	14289	16
Primary mirror	15377	9281	48
Secondary mirror	10126	5331	14
Primary mirror support	21496	11226	24
Spider assembly	329281	220171	6
Fork assembly	12673	8337	20
Total	**423097**	**269307**	**136**

In particular, a preliminary study on the analysis of thermal simulations of the LLR telescope had indicated key areas on the telescope components which are likely to have large thermal variations and related deformations due to T_∞ (Tsela et al., 2016a; Tsela et al., 2016). These simulations were considered in this research study to guide the selection of thermally important nodes throughout the FE model of the telescope's structural and optical components (Figure 20).

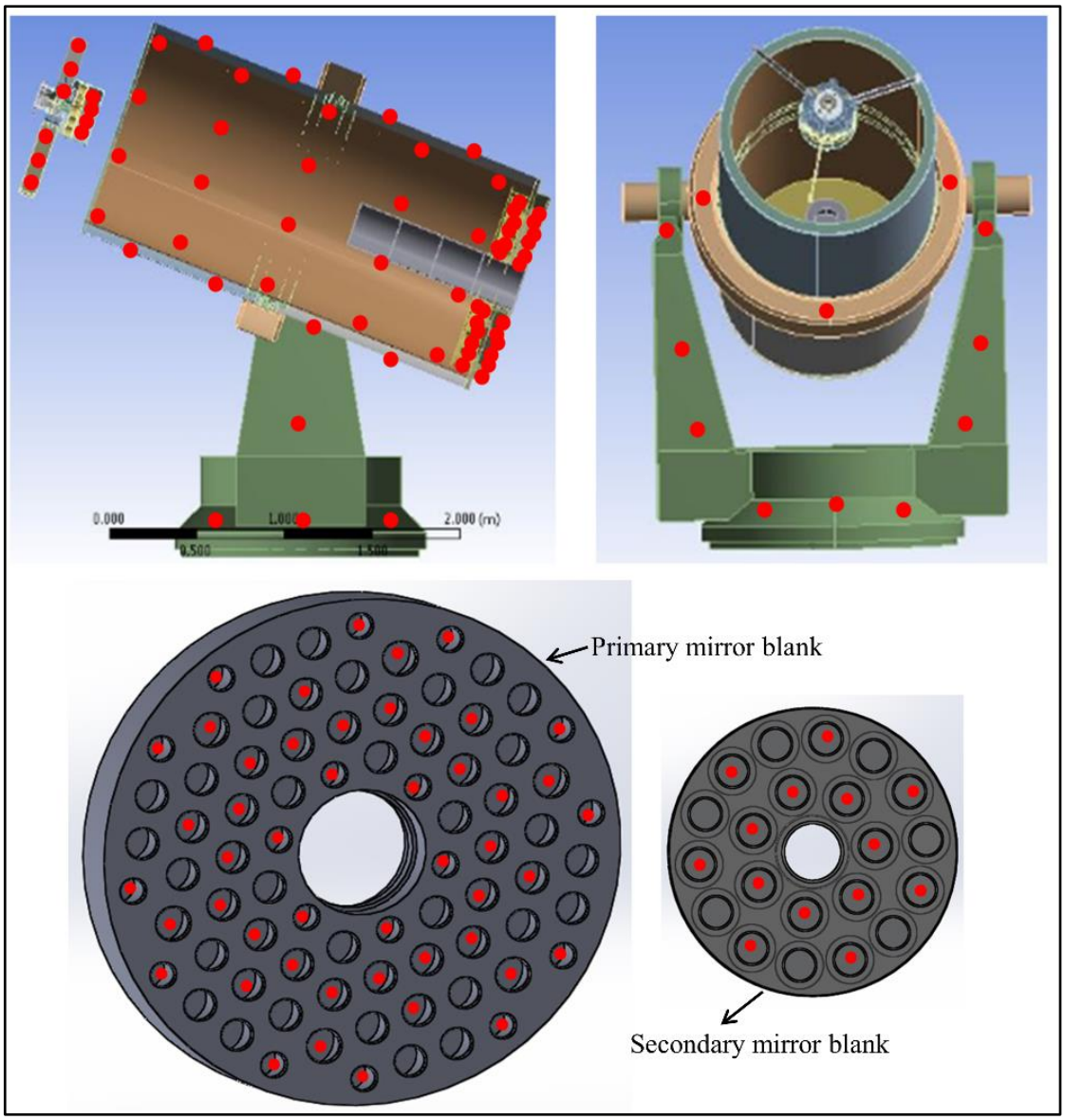

Figure 20: Proposed locations of temperature sensors on the telescope components. The red dots represent relative positions where the sensors ought to be mounted closer to the selected Finite element model nodes of the telescope structure and optics for acquisition of real-time temperature measurements.

3.2.3. Temperature sensors and calibration

The mounting of 136 RTDs was planned on the telescope components, virtually corresponding with the selected FE nodes (Table 4). In this research study, the F2020, 100 Ω, Class 'A' Platinum RTD thin film sensors manufactured by OMEGA were selected in accordance with the system design specifications (HartRAO, 2005). In particular, these sensors can detect any temperature within the range -100 ºC and +100 ºC at an accuracy level of ±0.5 ºC (or better given the observed ambient air temperature profiles of the HartRAO site (Tsela et

al., 2016a)). Additionally, these sensors (i) have a smooth contacting surface which is ideal for good thermal contact, and (ii) are compact in size, with dimensions of 2 mm (W) x 2 mm (L) x 0.8mm (H). The OB-200 epoxy adhesive from OMEGA with thermal conductivity of 222 *W/m.k* was used to glue RTD sensors onto a target surface. Notwithstanding their utilization for thermal monitoring of one of the world's best LLR systems (Murphy Jr et al., 2008), RTDs have been widely reported to possess excellent accuracies over wide temperature range, improved linearization, long-term stability and an annual drift below 0.1 ºC (Greenhalgh et al., 1994; Ibrahim, 2002).

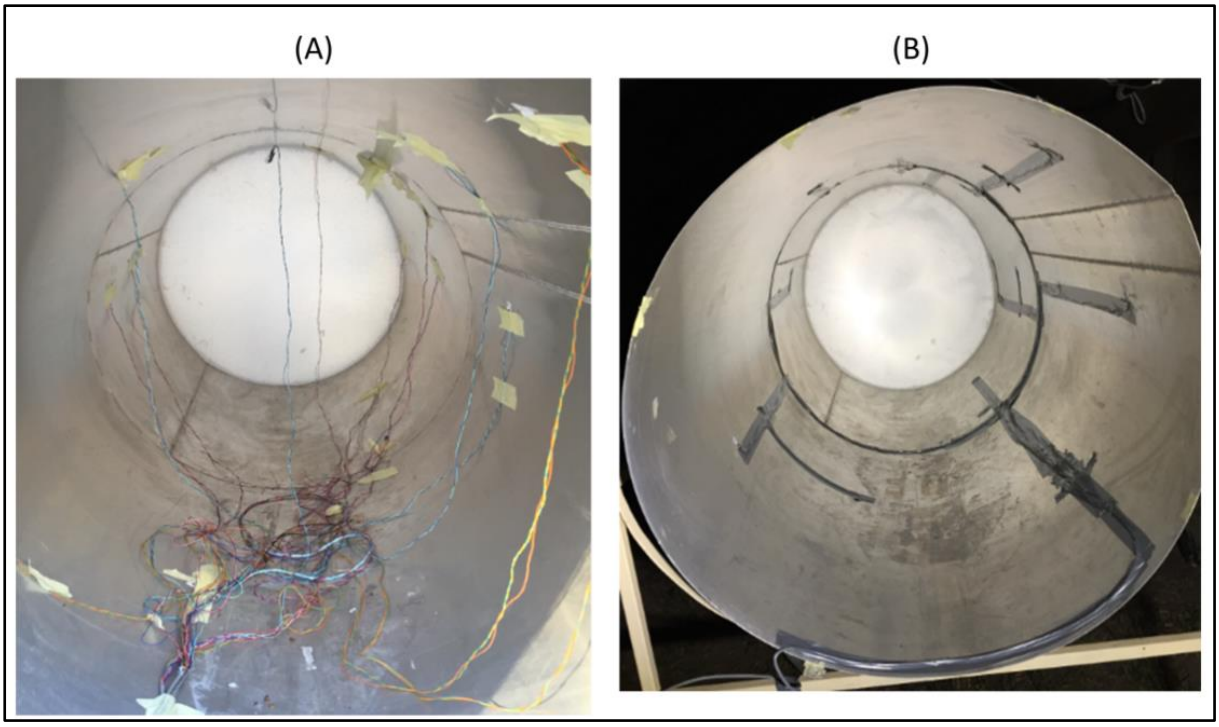

Figure 21: (A) Mounting of the 15 DS18B20 reference sensors within the mock-up tube (clearly depicted in section 3.2.5). The back-end of the tube is fitted with polystyrene which represents an insulator, with virtually similar thermal properties to the 1-metre Zerodur primary mirror of the HartRAO LLR telescope. (B) Concealment of the 15 mounted DS18B20 reference sensors and wires within the tube using a grey insulation tape.

Furthermore, the DS18B20 sensors (1-wire digital thermometer) were used to calibrate and compare temperature measurements obtained from the RTD sensors during day and night for successive days (Figure 21, Tsela et al., 2016). This DS18B20 1-wire digital thermometer detects temperatures between -10 ºC and +85 ºC at an accuracy of ±0.5 ºC. A total of 15 DS18B20 sensors were randomly mounted on the mockup tube close to any of the mounted RTDs (Figure 21, Tsela et al., 2016). As a result, the discrepancy between the RTD and DS18B20 concurrent temperature measurements at sampled locations was found to be on

average ±0.5 ºC, and therefore both sensor types were considered in this study to be reading the same temperature. These tests were important for detection of possible defects in the RTDs prior to installation on the HartRAO LLR telescope structure.

3.2.4. MAQ®20 Industrial data acquisition and control system

The commercially available MAQ®20 data acquisition system (Figure 22) which is manufactured by Dataforth Corporation, was used in this study for the real-time logging of temperature measurements from the mounted F2020, 100 Ω Platinum RTDs discussed in section 3.2.3. This system takes in a set of RTD31 modules, each with 6 input channels and has a module-dependent system accuracy of ±0.0035% (Figure 22).

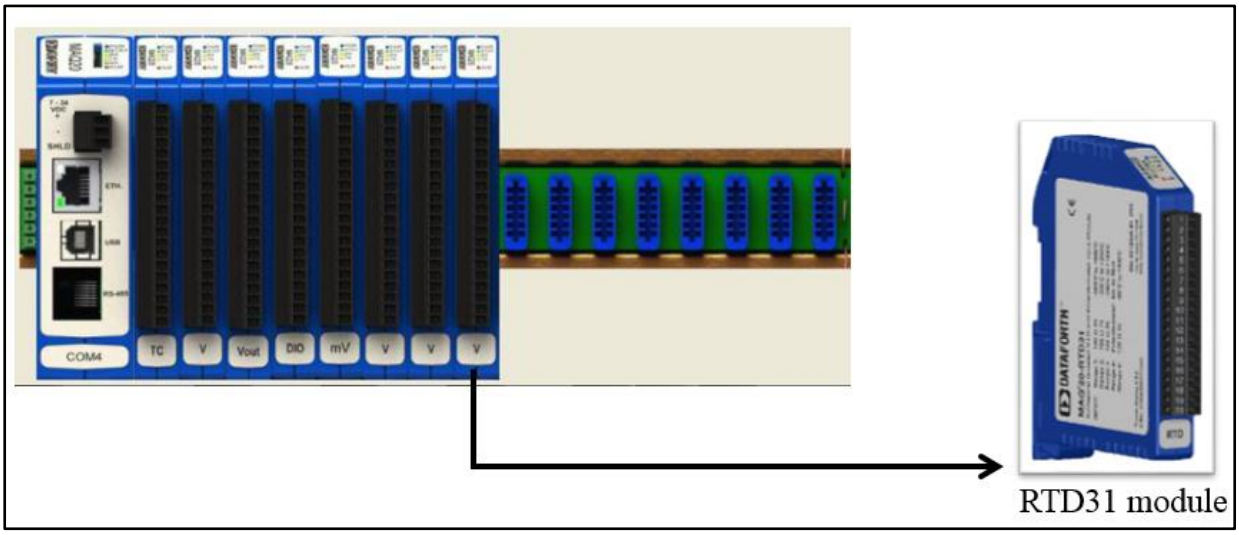

Figure 22: Illustration of the MAQ®20 data acquisition system comprising the power module and multiple input modules (https://www.dataforth.com/maq20.aspx). In particular, the Analog input module i.e. Resistant temperature detector (RTD) 31 with 6 input channels, supports connection of the 3-wire 100 Ω Platinum temperature sensors used in this study.

These modules support the 3-wire RTD configuration which has an embedded lead-wire compensation circuit to eliminate the effects of wire resistance (Pradhan and Sen, 1999). For instance, the wiring used in this study (i.e. Cat5e 12-core shielded cable) spans a distance of 9.4 m, which has lead-wire resistance of 1.77 Ω ±0.8%. This resistance (if not accounted for by the RTD31 modules) was estimated to erroneously offset temperature measurements by approximately 4.6 °C.

3.2.5. Mock-up telescope tube structure

The 1-metre aperture mock-up tube (Figure 23) which resembles virtually similar material and structural properties of the HartRAO LLR telescope tube (Figure 16, Tsela et al., 2016a) was used in this study, to conduct sensor calibration (section 3.2.3) and thermal experiments for comparison with the derived thermal simulations (Tsela et al., 2016). The mock-up tube is a two-way separable structure with a combined length of about 2500 mm and a diameter of 1020 mm (Figure 23). As shown in subsequent sections, temperature sensors were mounted on the outer tube surface and arranged systematically (guided by the initial thermal simulation results reported in Tsela et al., (2016a)) in order to measure the thermal variations across the tube surface at thermally important nodes.

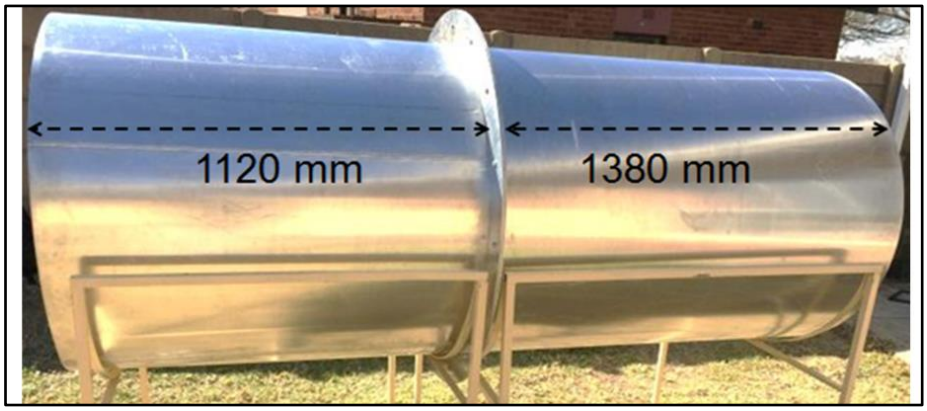

Figure 23: Aluminium mock-up tube structure used for conducting thermal experiments

3.2.6. Multi-Station and Prism Precision Reflectors

The Leica Nova MS50 Multi-Station manufactured by Leica Geosystems is an instrument for measuring, calculating and capturing data. In this study, the multi-station was used to conduct laser distance measurements to prism reflectors (Figure 24). This multi-station can range to a prism reflector located at distance of 1.5 m up to 10,000 m with a distance measurement accuracy of 1 mm + 1.5 parts per million (ppm) (http://surveyequipment.com/assets/index/download/id/219/). The ranging or distance measurement is done through the emission of a visible laser beam (centred at 658 nm) from the multi-station telescope, at a maximum average radiant power of 0.33 mW. In this study, the prism reflectors (Figure 25) were set-up to point directly at the multi-station. In particular, a total of 4 Leica GPH1P Prism Precision Reflectors (Figure 25) were used for the set-up. These reflectors have a centring accuracy of 0.3 mm (which relates to the optical centre of the prism)

at a range distance of up to 3500 m. Repeated laser distance measurements to the optical centre of the prisms mounted on the LLR telescope tube, are expected to yield distance variations between the true centre and the apparent centre of the prism, especially due to tube thermal variations.

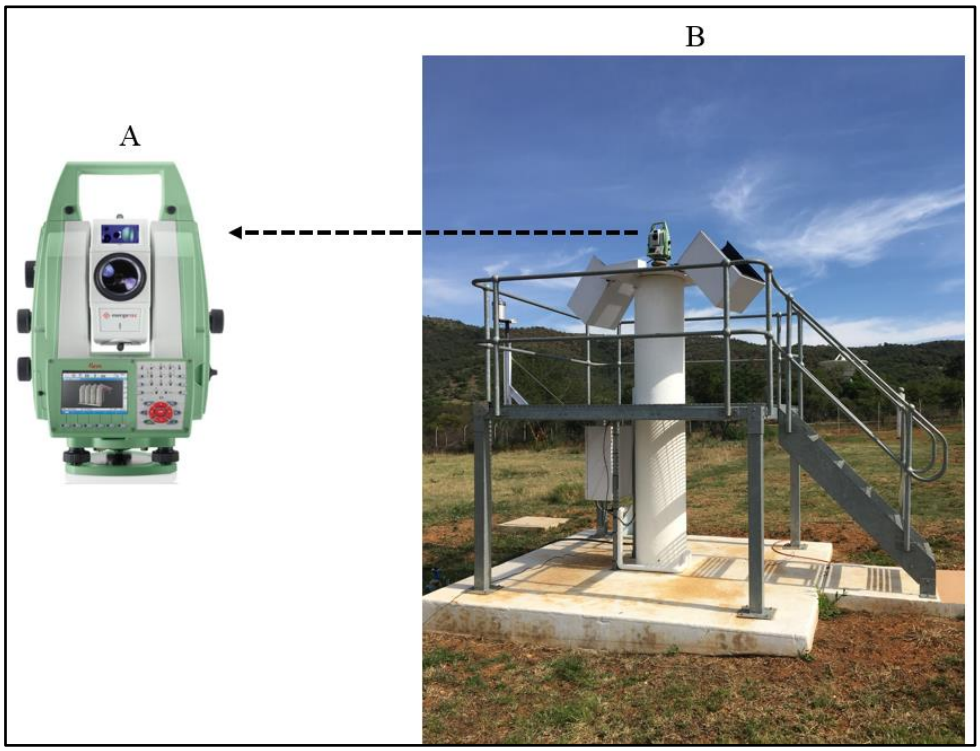

Figure 24: Leica Nova MS50 Multi Station (A) based in HartRAO (B) used to monitor coordinate displacements i.e. the northing, easting and height of the GPH1P retroreflectors mounted on the Lunar Laser Ranger tube structure.

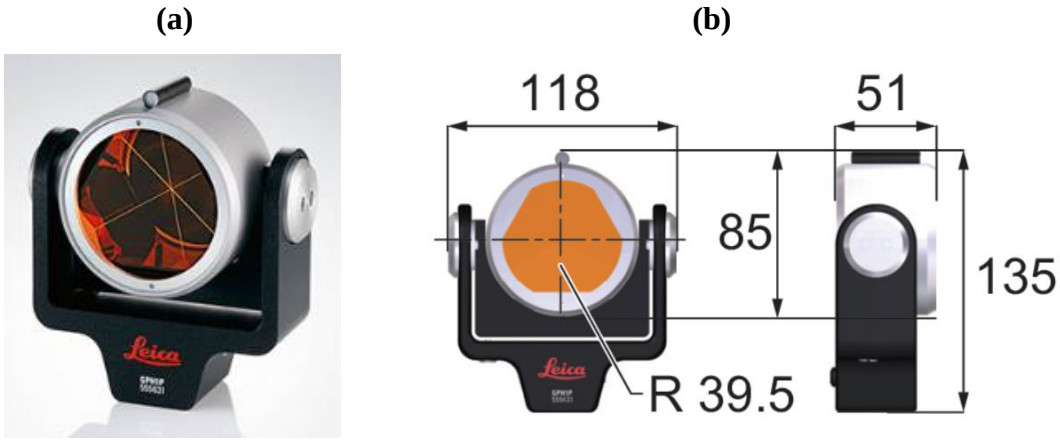

Figure 25: (a) Leica GPH1P Prism Precision Reflector that was used for measuring coordinate displacements and (b) its corresponding dimensions (https://accessories.leica-geosystems.com/common/shared/downloads/inc/downloader.asp?id=17723)

The automatic logging of 3-D coordinate displacements from each of the 4 prisms (Figure 26) took place during consecutive day- and night-time's at 5 minute intervals. This setup aided efforts to determine the extent of thermally-induced tube displacements during day- and night-time. In general, laser alignment systems could be regarded as an alternative method (Greve and Mangum, 2008; Pisanu et al., 2010; Zheng et al., 2012; Cui et al., 2015; Hu et al., 2015) relative to traditional approaches (Bremer and Penalver, 2002; Greve et al., 2005; Tsela et al., 2016b) to detect and measure the extent of object displacements particularly of the telescope's critical components as they undergo varying disturbances such as, thermal expansion or deformation triggered by the local climatic environment.

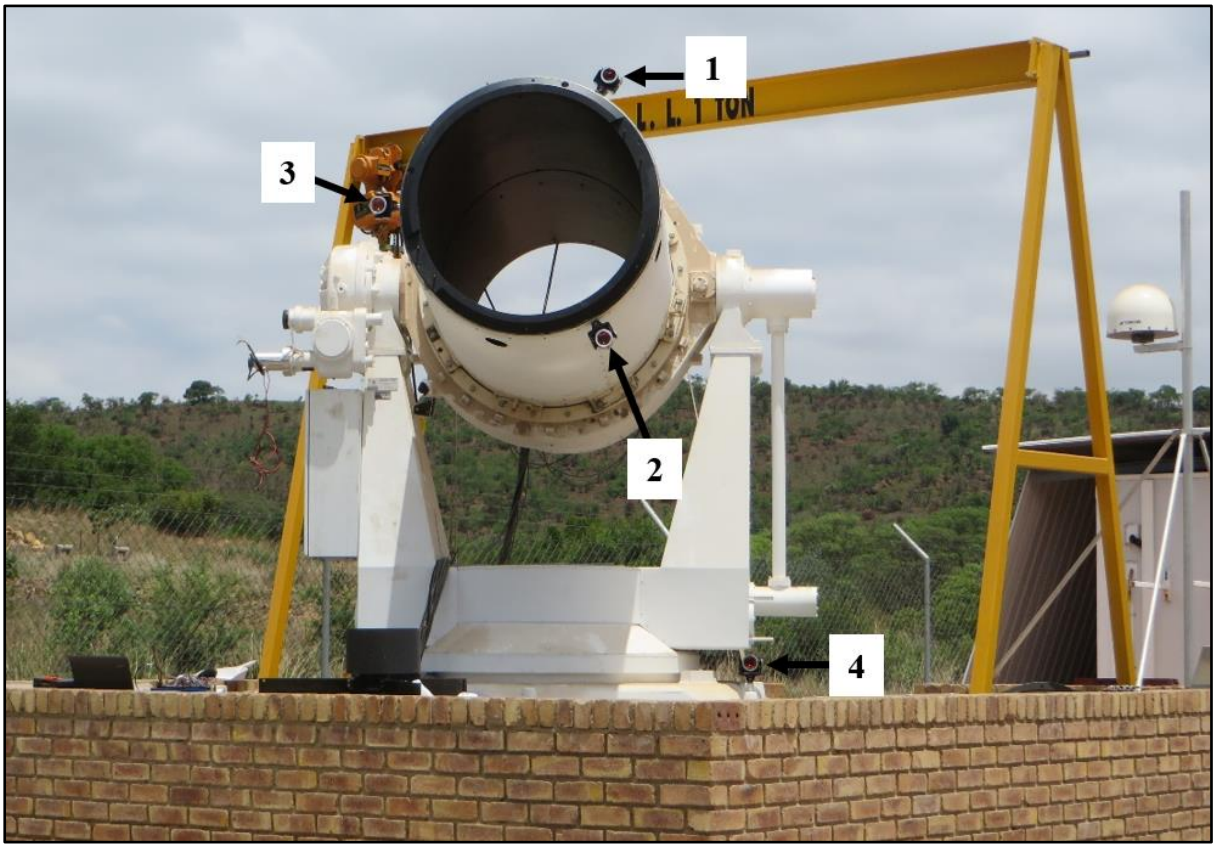

Figure 26: LLR telescope at HartRAO excluding the tube mirrors and spider assembly which are currently being revamped. In particular, 3 Leica GPH1P Prism Precision Reflectors are mounted onto the front-end of the tube (closer to where the spider assembly is mounted) and 1 more prism is mounted onto the telescope base linked to the pedestals (which are fixed onto the ground - hidden by the wall).

3.3. Description of data used

Table 5 presents a list of data sets used including their respective description and provider. Furthermore, the HartRAO site-based air temperature profiles are displayed in Figure 27 to indicate broadly, the temperature range and peaks, as well as the approximate times when rapid temperature changes occur at the site.

Table 5: Summary of data sets used in this research study

No.	Data set	Description	Use	Provider
1.	Hourly diurnal-air-temperature	Temperature data of the HartRAO site for summer, winter and autumn months of 2009, 2013 and 2018.	Guided the estimation of the widest possible temperature range including the approximate times when rapid temperature changes occur at the site where the LLR telescope is located. Data was also used an input parameter during thermal analysis of the telescope, well as for determining the relationship between temperature and telescope tube displacements	HartRAO
2.	RTD temperature measurements	Temperature measured at marked locations (i.e. thermally important FE nodes) on the mock-up tube as well as the LLR telescope tube	On the mock-up tube: (i) conducted tests of accurate temperature readings in relation to readings obtained through a sample of DS18B20 sensors; (ii) interpolate tube temperature at unmarked locations, (iii) analysis of the magnitude of tube thermal variations under different ambient temperature conditions, and (vi) compare acquired thermal variations with the derived thermal simulations. On the LLR telescope tube: determining the relationship between tube temperature and tube displacements	Self-produced
3.	Coordinate displacements	Daily distance measurements to prism reflectors mounted on the LLR tube and base structure. These measurements entail displacements in the height, northing and easting of the tube and base.	Determine the magnitude of tube displacements as a result of the ambient air (coupled with the sun effect) and tube temperature distribution.	HartRAO
4.	Interpolated tube temperature gradients	Real-time RTD temperature measurements at marked locations were used to interpolate temperatures at unmarked locations (i.e. locations without sensors)	Testing of proposed thermal model (Tsela et al., 2016b) on the tube structure	Self-produced

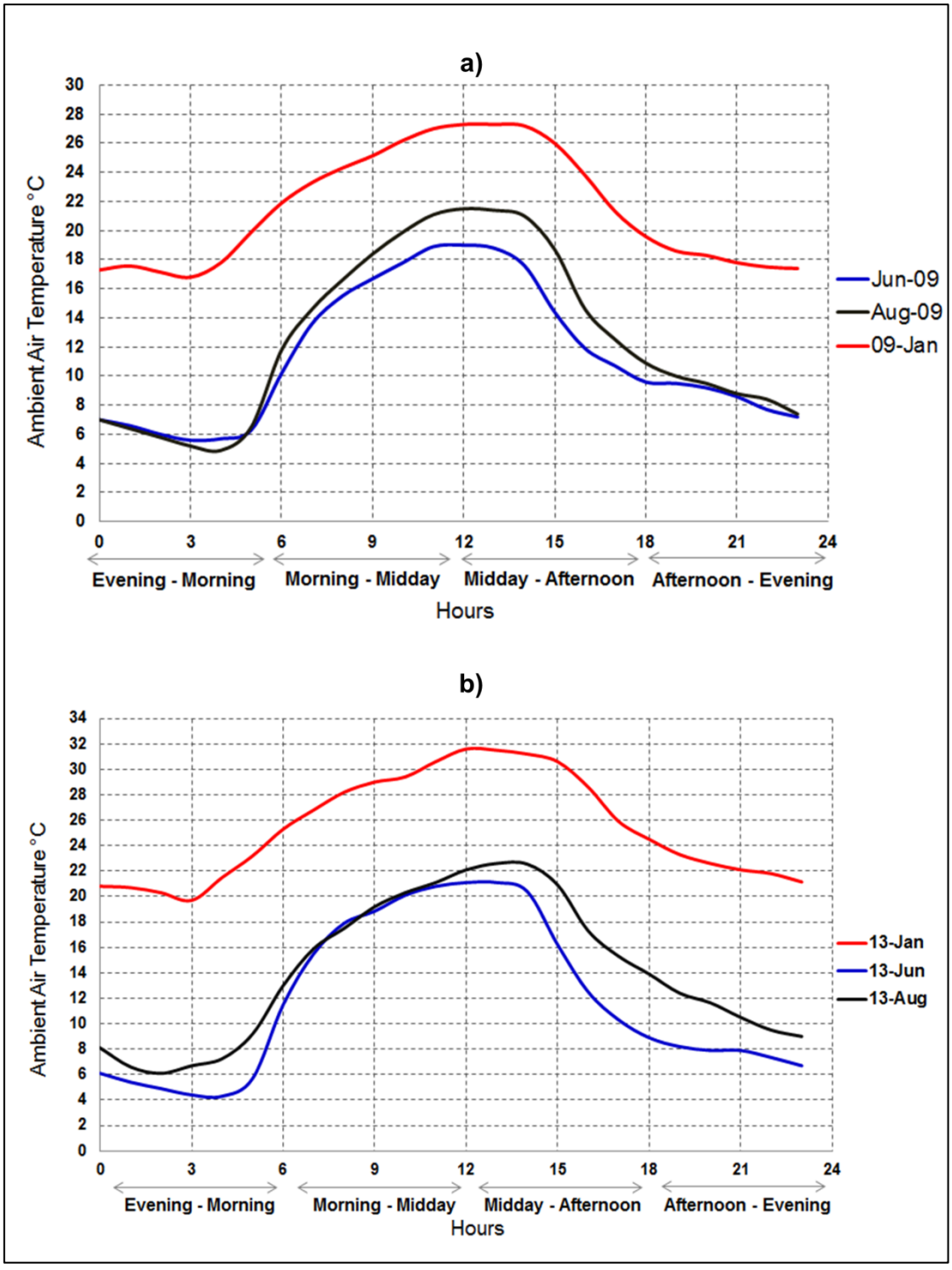

Figure 27: Hourly diurnal-air-temperature changes at the HartRAO site for summer, winter and autumn seasons of 2009 (a) and 2013 (b). These temperature plots were used to guide the estimation of the widest possible temperature range including the approximate times when rapid temperature changes occur at the site where the LLR telescope is located.

3.4. Description of methods used

3.4.1. Analysis of thermal variations

The analysis of thermal variations on the telescope composite structure (Figure 17) was performed in ANSYS software using heat transfer Equations (15) and (16):

$$\vec{Q}_{cv} = hA_x(T_x - T_\infty)\hat{e}_x + hA_y(T_y - T_\infty)\hat{e}_y + hA_z(T_z - T_\infty)\hat{e}_z. \quad (15)$$

$$\vec{Q}_{cd} = -k(A_x \frac{\partial T}{\partial x}\hat{e}_x + A_y \frac{\partial T}{\partial y}\hat{e}_y + A_z \frac{\partial T}{\partial z}\hat{e}_z). \quad (16)$$

In Equation (15) $\vec{Q}_{cv}$ represents the convection heat transfer rate between the telescope components and T_∞ at the HartRAO site. Here, h and T_∞ denotes the film coefficient of air temperature (W/m^2 °C) and ambient air temperature (°C) respectively; $\hat{e}_x, \hat{e}_y$ and $\hat{e}_z$ denotes the unit vectors; A_x, A_y and A_z represent the surface areas in meters; T_x, T_y and T_z are the temperatures in °C of the corresponding surfaces in three dimensional space of the assembled telescope structure respectively (Çengel and Ghajar, 2011).

Furthermore, in Equation (16) $\vec{Q}_{cd}$ represent the conduction heat transfer rate through the telescope component materials as a result of their temperature difference ∂T in three dimensional space; and the thermal conductivity k in W/mK (Çengel and Ghajar, 2011). Subsequent to the abovementioned heat transfer Equations, the analysis of heat transfer by radiation from the sun, sky and ground ought to be conducted particularly to understand the net radiation budget of the LLR telescope, and the overall effect on the telescope structure and optics. Although, this particular important analysis was not conducted (using ANSYS) in this study, efforts were taken in this study to acquire and monitor real-time RTD temperature measurements of the LLR telescope tube structure which was exposed to the sun, ground and sky radiation (during day and night) at the HartRAO site. This information was then linked with simultaneously acquired, electronic distance measurements of tube displacements in-order to determine the extent of thermally-induced tube displacements during day- and night-time.

The telescope composite structure (Figure 17) was assumed to be at an initial temperature of 9 ºC and subsequently subjected to T_∞ typical of the HartRAO site (Figure 27) encompassing

a 24 hour time period for a particular day in June (winter). In this study, we assumed stationary air at room temperature around the telescope structure by adopting a constant *h* value of 0.025 W/m²C. This assumption thus excludes the wind effect during this thermal analysis because, at HartRAO, no ranging to the lunar reflectors is expected to take place under windy conditions. However, the wind effect including the varying *h* values representative of natural and/or forced convection are possible future considerations for the current analysis so as to approximate reality (as far as possible). In overall, this analysis provided insight about the magnitude of thermal variations on and between the telescope components, particularly how these components thermally behaved in response to T_∞ (Tsela et al., 2016a; Tsela et al., 2016).

3.4.2. Analysis of thermally-induced deformations

The analysis of thermal deformations of the telescope component materials (Figure 17) was performed in ANSYS software, taking into cognizance the material length and volume changes due to thermal variations, expressed as $\alpha_l \Delta T$ and $\alpha_v \Delta T$ in Equations (17) and (18) respectively (Dalcher et al., 1977):

Change in length (μm) with temperature:
$$\frac{l_f - l_o}{l_o} = \alpha_l (T_f - T_o) = \alpha_l \Delta T \qquad (17)$$

Change in volume (m^3) with temperature:
$$\frac{v_f - v_o}{v_o} = \alpha_v (T_f - T_o) = \alpha_v \Delta T \qquad (18)$$

In Equation (17), the symbol α_l represents the linear CTE which quantifies the amount of strain on a material with a change in temperature ΔT. The symbol α_v in Equation (18) denotes the volume CTE or the extent to which the volume of a material changes subject to ΔT. This analysis was conducted using ANSYS software to provide a spatial and temporal indication of the total thermal deformations of the telescope component materials in the x, y and z directions (Tsela et al., 2016a).

3.4.3. Description of the proposed mathematical thermal model

The thermal model presented in this subsection was initiated by Greve et al. (1996) followed by notable refinements later on (Bremer and Penalver, 2002; Greve et al., 2005) for

detailed thermal modelling of radio telescopes, characterized by varying design specifications and climatic environments. Basically, the model entails installation of several temperature sensors on strategically identified locations throughout the telescope's critical components. Thereafter, real-time temperature measurements are acquired and fed into a mathematical thermal model for monitoring thermal variations and calculating thermally-induced deformations of the telescope structure. This information can be used to determine the extent of thermally-induced pointing offsets, and the needed corrections either in the pointing model parameters (Wresnik et al., 2007; Combrinck, 2014) or through microprocessor-controlled venting systems (Bremer and Greve, 2011).

Notwithstanding the importance of the simulation-based method for example, Cho et al. (2010) and Vogiatzis et al. (2014) by far, the abovementioned method has been tested over the years to be reliable in providing detailed real-time temperature monitoring and modeling for prediction and correction thermally-induced pointing errors, even for optical laser telescopes (for example Mittag et al. (2008)). In particular, this study describes procedures of the mathematical thermal model adapted for thermal modelling of the HartRAO LLR optical telescope (Tsela et al., 2016b) in-order to mitigate thermal variations of critical components to ~ 1 °C and contribute toward the attainment of the required pointing accuracy of ~1″ (Combrinck 2014).

3.4.3.1. Modelling of thermal gradients

Temperatures measured at the selected FE nodes (T_K) of the LLR telescope structure (Figure 19, Table 4) are used to interpolate temperatures of the elements (E) of the telescope structure using interpolating functions. These functions are basically polynomials whose degree is dependent on the number of nodes (Bremer and Penalver, 2002; Greve et al., 2005). In particular, the temperature of every element with K nodes can be expressed using Equation (11) as follows:

$$T(x, y, z, t) = [W(x, y, z)][T(t)] \tag{19}$$

where $[W(x, y, z)]$ represents the row matrix of the temperature interpolating function $W(x, y, z)$; and $[T(t)]$ denotes the column matrix of nodal temperatures as a function of time.

Thereafter, the interpolated temperatures in Equation (19) are used to determine the thermal gradients within each element across all the telescope structural components by solving

a matrix of Equations. Since, the thermal gradients are multidirectional within the elements (i.e. may occur in the x, y and /or z directions) they can be derived using Equations (20) - (22):

$$\frac{\partial T(x,y,z)}{\partial x} = \sum_{i=1}^{k} \frac{\partial W_i(x,y,z)}{\partial x} T_i(t) \tag{20}$$

$$\frac{\partial T(x,y,z)}{\partial y} = \sum_{i=1}^{k} \frac{\partial W_i(x,y,z)}{\partial y} T_i(t) \tag{21}$$

$$\frac{\partial T(x,y,z)}{\partial z} = \sum_{i=1}^{k} \frac{\partial W_i(x,y,z)}{\partial z} T_i(t) \tag{22}$$

where $i = 1,2\ldots,k$ and k represents the number of nodes with sensors where measurements are sampled. Therefore, Equations (20) - (22) can be written in a matrix as follows:

$$\begin{pmatrix} \frac{\partial T(x,y,z)}{\partial x} \\ \frac{\partial T(x,y,z)}{\partial y} \\ \frac{\partial T(x,y,z)}{\partial z} \end{pmatrix} = \begin{bmatrix} \frac{\partial w_1(x,y,z)}{\partial x} & \frac{\partial w_2(x,y,z)}{\partial x} & \cdots\cdots\cdots & \frac{\partial w_k(x,y,z)}{\partial x} \\ \frac{\partial w_1(x,y,z)}{\partial y} & \frac{\partial w_2(x,y,z)}{\partial y} & \cdots\cdots\cdots & \frac{\partial w_k(x,y,z)}{\partial y} \\ \frac{\partial w_1(x,y,z)}{\partial z} & \frac{\partial w_2(x,y,z)}{\partial z} & \cdots\cdots\cdots & \frac{\partial w_k(x,y,z)}{\partial z} \end{bmatrix} [T(t)] = B[x,y,z][T(t)] \tag{23}$$

where $B[x,y,z]$ represents a matrix of the interpolated thermal gradients throughout the telescope structure.

Furthermore, thermally-induced structural deformations can be calculated from the abovementioned interpolated temperature gradients throughout the telescope. Equations (19) - (23) represent the first phase of the thermal model to calculate (interpolated) thermal gradients of the HartRAO LLR telescope in real-time. This phase of the model has so far been tested on the mockup tube structure, and efforts are underway to test the model on the HartRAO LLR telescope structure.

3.4.3.2. Interpolation of temperatures

As discussed above, Equation (19) is used for interpolating temperatures between the mounted sensors (or at locations without sensors) on the telescope material components. In particular, Equation (19) is alternatively expressed in Equation (24) below for legibility and ease of explaining the procedure, and thus was tested in this study on the mockup tube structure, for the interpolation of the telescope tube temperatures:

$$T(x, y, z, t) = \sum_{i=1}^{n} W_i(x, y, z) T_i\,(t) \tag{24}$$

For improved computational efficiency (given the large number of FE model nodes of the LLR telescope structure (Figure 19, Table 4)) during the interpolation procedure of finding unknown temperatures from fewer marked positions with RTD sensors, a slightly modified version of Equation (24) can be written as:

$$T_i = \frac{\sum_{l=1}^{m} T_l W_{il}}{\sum_{l=1}^{m} W_{il}} \tag{25}$$

where *n or m* denotes selected nodes (positions) with RTD sensors out of a total of *N* Finite element (FE) model nodes; T_i (*i* = 1, 2, 3, .., .., *N*-*m*) is the temperature at a position without a sensor; T_l (*l* = 1, 2, 3, .., .., *m*) is the temperature at a position with the RTD sensor denoted $T_{measured}$.

Furthermore, the weighting function W_{il} is defined as follows (Bremer and Penalver, 2002):

$$W_{il} = \frac{1}{[\varepsilon^2 + (x_i - x_l)^2 + (y_i - y_l)^2 + (z_i - z_l)^2]^p} \qquad 1 \leq p \leq 3 \text{ and } \varepsilon = 0.1\text{cm} \tag{26}$$

where the x_i, y_i and z_i denote coordinates in mm of the $T_{reference}$ sensors on the tube (i.e. position without sensor ($T_{reference}$ basically denote reference temperature used to validate the interpolated temperature)), and x_l, y_l and z_l denote coordinates in mm of the $T_{measured}$ sensors (i.e. position with a sensor).

Therefore, these coordinates were used to compute the relative distances between measured temperatures and locations of unknown temperature (monitored by $T_{reference}$) to be interpolated. The parameters p represents the order of polynomial, whereas, ε denotes a numerical quantity to avoid singularities i.e. division by 0 particularly for locations (x, y, z) close to each other. In this study, Equation (25) was tested on the mockup tube structure, representative of the LLR tube with the aim of achieving the targeted interpolation accuracy of at least 0.3 °C. This interpolation accuracy was intuitively selected for this study in-order to ensure that the computed or overall temperature distribution is minimally (or not) inflated erroneously (Greve et al., 2005; Bremer and Penalver, 2002; Greve and Bremer, 2010; Greve et al., 2005). Further testing ought to be carried-out on the actual components to obtain a holistic spatio-temporal thermal behaviour of the LLR telescope composite structure in response to T_{∞}. This information constitutes an important phase for the computation of thermally-induced structural deformations.

3.4.3.2. Modelling of thermally-induced structural deformations

To compute thermally induced deformations we follow the method proposed by Greve et al. (2005) although adapted in this study to the critically-identified component materials of our LLR telescope (Tsela et al., 2016b). For each important component or substructure of the telescope we assign the matrix $\boldsymbol{M}_{substructure}$. For example, the matrices of the tube and primary mirror are denoted by the matrices $\boldsymbol{M}_{tube}$ and $\boldsymbol{M}_{primary}$ respectively. Corresponding to each matrix are the deformations δ_{tube} and $\delta_{primary}$. Take note, the tube and primary mirror are used as exemplary substructures in-order to simplify the description of the modelling procedure. Furthermore, this procedure is applied analogously to residual substructures of the telescope such as, the fork arms, *El*/ *Az* mounts and spider assembly.

Assume, the selected number of nodes with sensors (T_K) on the tube is 16 (according to Table 4) we can therefore express $\boldsymbol{M}_{tube}$ as:

$$\mathbf{M}_{tube} = \begin{bmatrix} \delta_{tube}(1,1).....\delta_{tube}(1,N) \\ \delta_{tube}(2,1).....\delta_{tube}(2,N) \\ ..... \\ \delta_{tube}(16,1).....\delta_{tube}(16,N) \end{bmatrix} \tag{27}$$

where N is the total number of FE nodes used to model the whole telescope structure. $\boldsymbol{M}_{primary}$ is similarly represented. Consequently, the deformations on the tube structure $\Delta\boldsymbol{M}_{tube}$ for a specific thermal load can be obtained by:

$$\Delta\mathbf{M}_{tube}(k) = \begin{bmatrix} \delta_{tube}(1,1).....\delta_{tube}(1,N) \\ \delta_{tube}(2,1).....\delta_{tube}(2,N) \\ ..... \\ \delta_{tube}(16,1).....\delta_{tube}(16,N) \end{bmatrix} \begin{bmatrix} \frac{\partial T(x,y,z)}{\partial x} \\ \frac{\partial T(x,y,z)}{\partial y} \\ \frac{\partial T(x,y,z)}{\partial z} \end{bmatrix} \tag{28}$$

$$\text{where} \quad \begin{bmatrix} \frac{\partial T(x,y,z)}{\partial x} \\ \frac{\partial T(x,y,z)}{\partial y} \\ \frac{\partial T(x,y,z)}{\partial z} \end{bmatrix} = \begin{bmatrix} \Delta T_1 \\ \Delta T_2 \\ ..... \\ \Delta T_N \end{bmatrix} \text{ similar to equation (23)} \tag{29}$$

where the ΔT_i $(i = 1,2...N)$ are obtained from superposition of the individual deformations.

Each element $\delta_{tube}(node, N)$ of the $\boldsymbol{M}_{substructure}$ matrix is obtained from the ANSYS software (Greve et al., 2005; Greve and Bremer, 2010; Greve et al., 2005). The ΔT column matrix is obtained by measuring the temperature of the relevant structure at some k sensor assigned node (where k is a subset set of the N nodes with sensors) then taking the derivative of the interpolated temperature as described above.

3.4.4. Tube experiments

3.4.4.1. Mockup tube (RTD) measurement setup

A total of 64 RTD sensors were systematically arranged and thermally bonded on the outer surface of the mockup tube (Figure 28, Figure 29). The illustration in Figure 28 was instrumental in the positioning, labeling and troubleshooting of RTD sensors (Tsela et al., 2016). In particular, the arrangement of sensors on the tube was such that, they are equally

spaced and dense as much as possible in-order to acquire a representative distribution of thermal variations of the tube structure relative to T_{∞}.

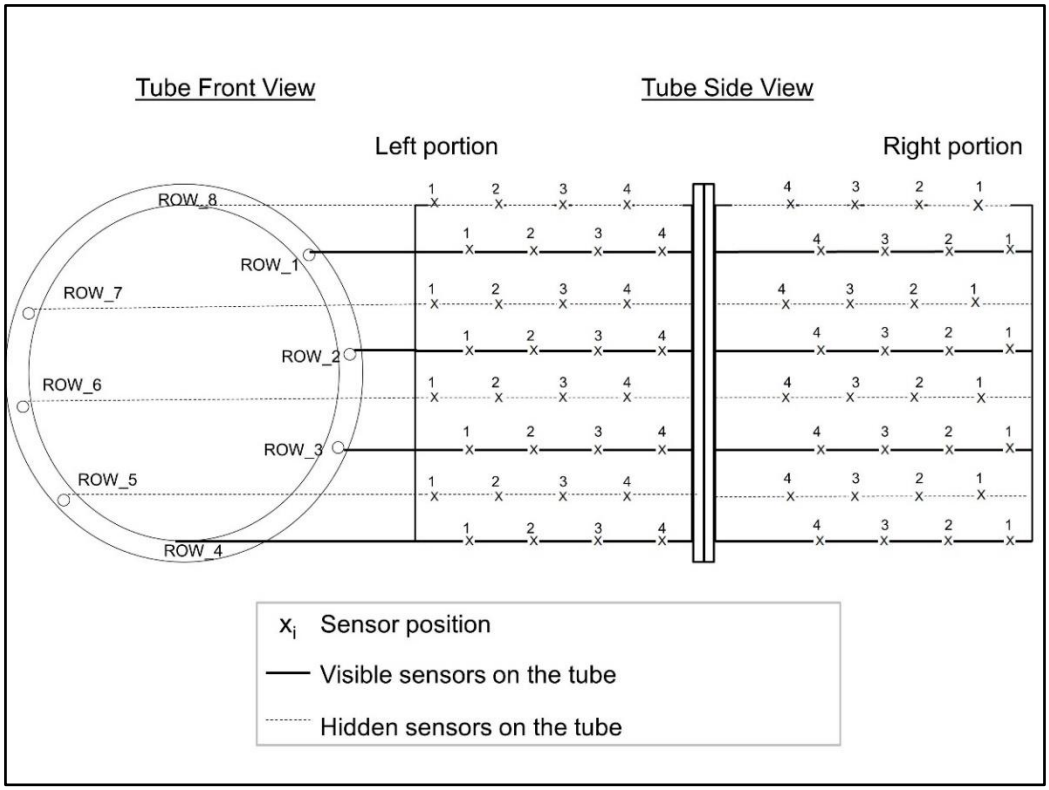

Figure 28: Placement of temperature sensors (RTDs) on the mock-up tube. The distance between sensors along the tube is approximately 140 mm whereas the distance between rows, around the tube is 127.5 mm.

Figure 29: Troubleshooting and simple calibration setup of the tube showing the mounting and alignment of RTD sensors including the wiring and digital multimeters.

The complete tube experiment setup comprising the tube, RTD sensors, digital multimeters as well as the wiring is shown in Figure 29. During the installation of RTD sensors, it was necessary to verify and compare the temperature of particular RTD sensors. In particular, digital multimeters were used solely for this purpose. Fixed within the tube at specific, corresponding RTD sensor locations are the DS18B20 reference sensors (discussed earlier in section 3.2.3). These reference sensors were used during the experiment as final calibration reference and to detect possible faulty sensors. The above procedure was necessary to ensure verified RTD sensor readings were acquired (Tsela et al., 2016).

3.4.4.2. Interpolation of temperature on the mockup tube

Twenty four RTD sensors denoted $T_{measured}$ (Figure 30) were thermally bonded onto the outer (mockup) tube surface for acquiring tube temperature measurements and for interpolating the temperature between the $T_{measured}$ sensors. The entire interpolation procedure was based on Equations (24) - (26) described earlier in section 3.4.3.2. On the other hand, another set of twenty four RTD sensors denoted $T_{reference}$ was mounted between the $T_{measured}$ RTD sensors on the tube (Figure 30).

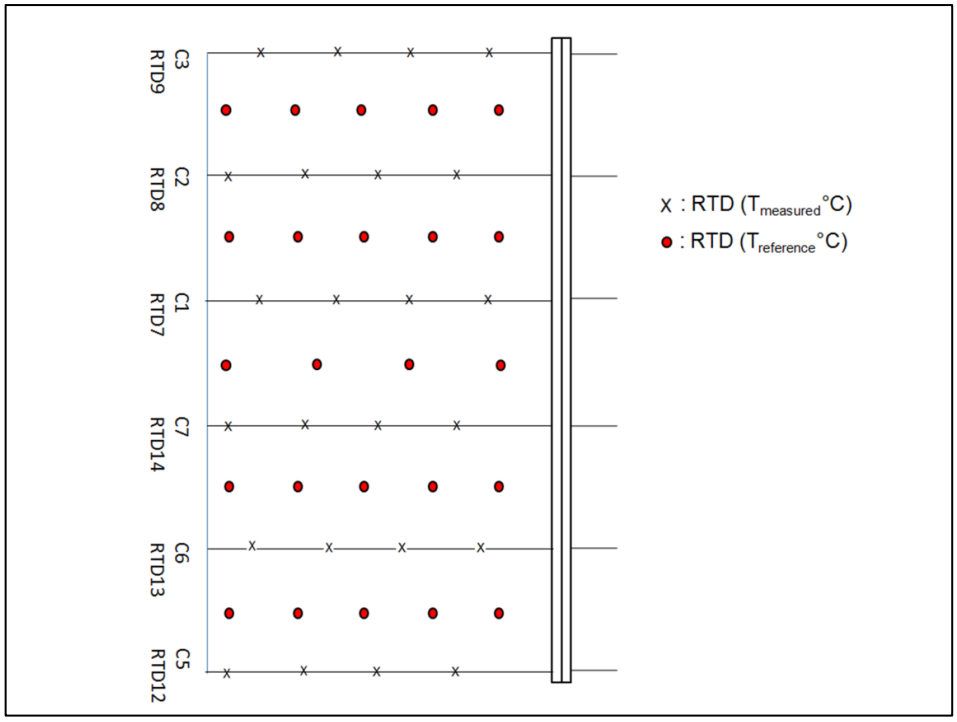

Figure 30: Portion of the mock-up tube depicting marked positions of the mounted RTD sensors denoted $T_{measured}$ and $T_{reference}$ respectively. Labels on the far left depict tube row identity with the corresponding RTD31 module number used for this experiment.

In this study, the $T_{reference}$ tube temperature data was primarily used for comparison with the interpolated tube temperature data and calculation of interpolated temperature error at the corresponding locations on the tube. Measurements for both $T_{measured}$ and $T_{reference}$ were recorded through the RTD31 modules connected to the MAQ®20 data acquisition system (Figure 22).

Prior thermal simulation results of the telescope tube assembly indicated the components where most thermal variations would occur (Tsela et al., 2016). In particular, the simulation results of the outer tube surface revealed minimum-maximum thermal variations for a full-day of about 1.06 °C when exposed to T_{∞} at the site. These results showed isotherms propagating from the 'open' front-end of the tube toward the 'closed' back–end where the primary mirror is structurally located. This information was used to strategically identify $T_{measured}$ positions on the tube structure for placement of RTD sensors (Figure 30) such that a representative sample of temperature variations can be acquired.

Figure 31: Thermally bonded RTD sensors for $T_{measured}$ and $T_{reference}$ on the test tube, all wired using the 12-core cat5e shielded cable. Visible strips/ patches of the insulation tape aided the alignment of the wiring.

The portion of the tube depicted in Figure 30 and Figure 31, is typical of the back-end where the primary mirror is structurally located; and has a sub-length of 1120 mm with distances of about 140 mm between RTD sensors ($T_{measured}$) along the tube and 127.5 mm between rows around the tube, respectively. Furthermore, the acquired $T_{measured}$ data constitute an important parameter in the proposed thermal model (section 3.4.3) specifically for the interpolation of temperature (subsection 3.4.3.2) at unmeasured or $T_{reference}$ locations on the tube. In particular, Figure 31 depicts the actual tube experimental setup conducted in this study, where the RTD wiring is straightened along the tube concealed with an insulation tape; the back-end of the tube is fitted with polystyrene, which represents an insulator typical of the 1–metre Zerodur primary mirror installed on the HartRAO LLR telescope.

3.4.4.3. LLR tube (RTD) measurement setup

The complete tube experiment setup at HartRAO comprising the actual LLR tube and 64 RTD sensors, for the acquisition of real-time temperature measurements of the tube structure is shown in Figure 32. This experiment setup was based primarily on the procedure described in section 3.4.4.1 (demonstrated in Figure 28).

The difference between the two experiments is that, on the mockup tube, there were no arc-metal sheets (Figure 33 (A)) to cover the mounted sensors, and the mockup tube was never integrated (unlike the actual LLR tube (Figure 33 (B)) into any structure. The mockup tube experiment was pivotal for calibration of RTD sensors as well as, testing the arrangement and strategic placement of sensors for representative readings of the tube temperature distribution with respect to ambient temperature (Tsela et al., 2016). The testing was also extended to the interpolation procedure of the proposed thermal model.

On the other hand, the LLR tube, mounted with sensors and covered with arc-metal sheets, was integrated into the telescope structural body (Figure 33) in-order to enable investigation of the relationship between tube temperature and temperature-induced tube displacements. Note, the internal components of the LLR tube, such as the mirrors, back plate and spider assembly, could not be integrated into the tube structure due to ongoing refurbishments. The integration of outstanding internal components will take place soon as the refurbishments are completed, as this would aid future experiments to produce more realistic indications of thermally-induced tube displacements.

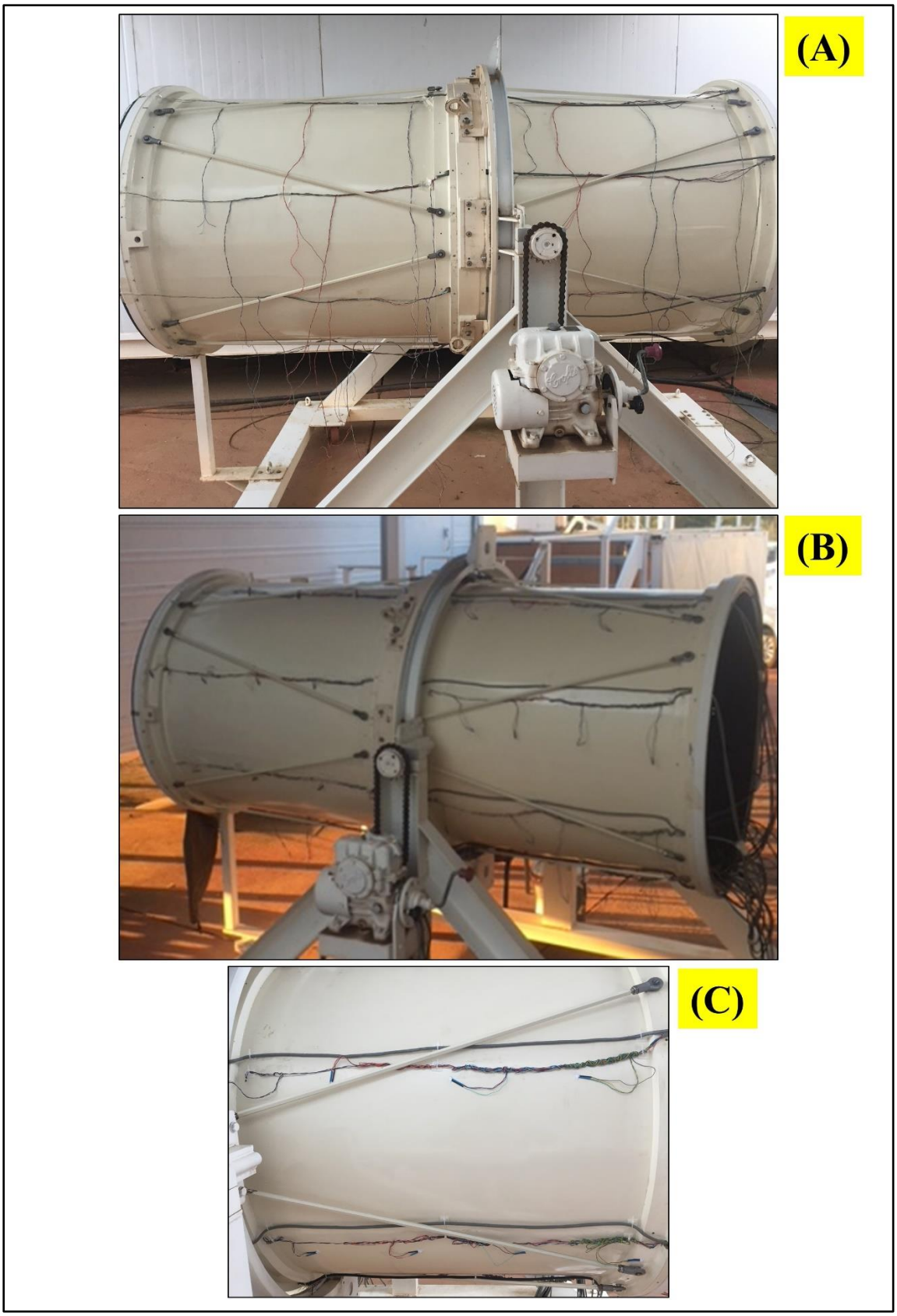

Figure 32: Sensor wiring arrangement (A) and mounted RTD sensors (B) on the first-layer surface of LLR optical tube at HartRAO. The LLR tube was placed on a metal stand that aided the LLR tube experiment setup. An expanded view of the mounted RTD sensors can be seen on the tube for legibility (C).

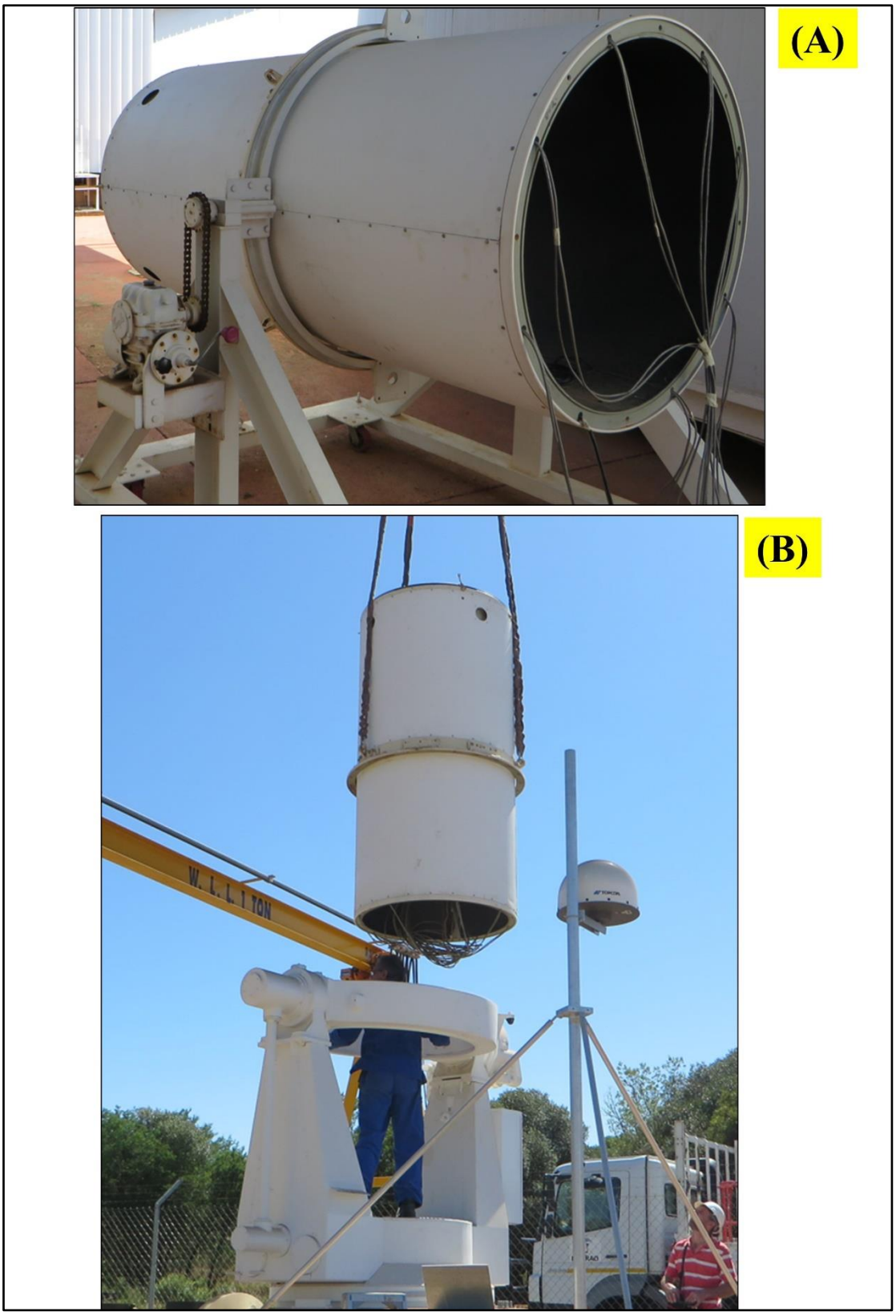

Figure 33: The arc-metal sheets were used to cover the mounted sensors on the LLR tube (A). These sheets insulated the sensors from external disturbances such as exposure to direct sun light and wind. The LLR tube was integrated into the telescope's elevation and azimuth mount at HartRAO (B). Note, the small circular openings on the front-end of the tube cover sheets indicate the relative locations of the fans, which were not installed for this experiment.

3.4.4.4. LLR tube displacement

This experiment was performed in this study to determine the extent of thermally-induced tube displacements during day- and night-time (Figure 34). The description of equipment used for this experiment is provided in section 3.2.6 of this chapter. Basically, daily distance measurements to prism reflectors mounted on the LLR tube and base structure were acquired. These measurements entail displacements in the height, northing and easting of the tube and base. In particular, the use of 4 prisms as shown in Figure 34 provided information on the relative displacements taking place at different parts of the telescope (Figure 26). For example, the prism mounted on the base structure was used to monitor the stability of the telescope base structure and to establish whether the displacements taking place at the tube are influenced by the stability of the telescope base structure. The tube was parked at an elevation of 30° (facing the multi-station) in order for any tube displacements in either the x, y and/or z direction to be measured.

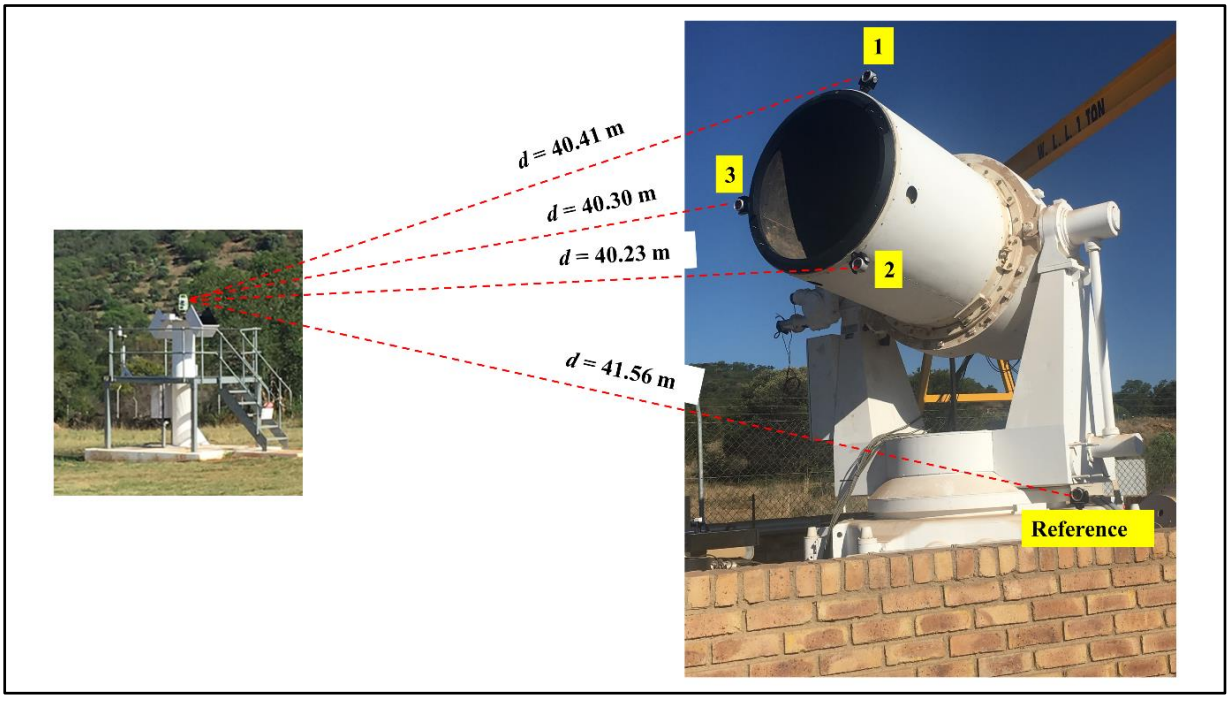

Figure 34: The LLR tube displacement monitoring experiment based on the site-based Leica Nova MS50 Multi-Station and 4 Leica GPH1P Prism Precision Reflectors mounted on the telescope tube and base. The horizontal distance (*d*) between the multi-station and the respective prisms mounted on the telescope is shown in the figure.

Virtually similar experiments based on laser alignment systems have been successfully tested (for example Hu et al. (2015)) with the aim of measuring the extent of the object's displacement and determining strategies to compensate for the displacements. In our case, this could be the displacements of the telescope's critical components (such as the tube) due to varying air temperatures causing thermal expansion or deformation of the component, which are known to be detrimental to telescope pointing accuracy (Mittag et al., 2008). In particular, the output of this experiment could be an important parameter in the precise determination of the amount of thermally-induced pointing error of the HartRAO LLR so that, the error can be compensated in the LLR pointing model under construction (Combrinck, 2014) or through a micro-controller ventilation system.

3.5. Concluding remarks

This chapter gave detailed information pertaining the (i) study site, (ii) LLR performance requirements, (iii) material, data and methods used, (iv) proposed LLR thermal model and methods used, and (v) experiments conducted. In particular, it was acknowledged that the study site i.e. HartRAO has a unique local climatic environment and its parameters ought to be taken into cognizance during thermal analysis of the LLR telescope. These parameters, such as T_{∞}coupled with the thermal properties of the LLR telescope component materials could have influence on the LLR performance requirements, especially pointing (Bely, 2003) which is expected to be accurate at ~1″ (Combrinck, 2014). Key to the attainment of such high pointing accuracy to the lunar reflectors is, thermal analysis and control of the telescope critical components (Murphy Jr et al., 2008). Thus, various material and data sets were described in this chapter for conducting first-phase analysis of thermal variations and thermally-induced deformations, with respect to T_{∞} through simulations of the HartRAO LLR telescope structure and optics. These simulations are considered important in providing information regarding the thermal behaviour of the LLR telescope components and also in guiding the design of the thermal model proposed in this study.

Furthermore, the proposed thermal model of the HartRAO LLR telescope was presented in this chapter. A sequence of mathematical steps was laid out, spanning the strategic placement of temperature sensors, measurement and interpolation of temperatures, calculation of thermal gradients and thermally-induced deformations. This model is regarded as a practical approach for real-time temperature data acquisition of the telescope structure and optics, as well as

calculating the magnitude of temperature variations and related structural deformations with respect to T_{∞}. In particular, the deformations are known to potentially cause displacements or misalignments of the tube and/or its optical axis, and thus detrimental to pointing accuracy (Mittag et al., 2008). In this chapter, portions of the proposed thermal model were tested through various experiments. For example, the strategic placement of temperature sensors, measurement (through MAQ®20) and interpolation of temperatures were tested on the mockup tube as well as on the actual LLR tube. The deformations part of the model was not tested in this study, however through experiments the thermally-induced displacements of the LLR tube (assembled into the telescope elevation and azimuth mount) were determined by use of a set of prisms and a fixed multi-station at the HartRAO site. This information could aid in the determination of pointing offsets due to thermally-induced displacements of the tube structure.

During the course of this study, the internal components of the LLR tube, such as the mirrors, back plate and spider assembly, could not be integrated into the tube structure due to ongoing refurbishments. Therefore, the integration of outstanding internal components is expected to take place soon as the refurbishments are completed, as this would aid future experiments to produce more realistic indications of thermally-induced tube displacements.

Most of the content of this chapter has been published in journal papers by the current author. For example, the heat transfer mechanisms for thermal analysis (Tsela et al., 2016a; Tsela et al., 2016), the proposed thermal model (Tsela et al., 2016b) as well as the mockup tube experiments (Tsela et al., 2016) have been published, respectively.

Chapter 4: Results and Discussion

4.1. Thermal analyses of the LLR optical tube assembly

4.1.1. Analysis of thermal variations

For T_∞ that varied from ~9 ºC to 23 ºC spanning the time period 00:00 and 11:30 a.m., the resulting minimum and maximum thermal variations across the telescope component materials were 9.3 ºC to 10.1 ºC (Figure 35). In particular, the (Zerodur) primary mirror had the lowest thermal variations of ~0.1 ºC relative to the other component materials with respect to T_∞ for the time period under study. This observation is found to be consistent with the thermal properties of the mirror (see, Schott, 2011 and Table 3), especially given its low *k*. Timely equalization using either natural or forced air ventilation of these variations on the mirror (which responds comparatively slow to ambient temperature changes) including other component materials of the tube assembly is important for overall optical and pointing performance of the telescope (Perry, 1943).

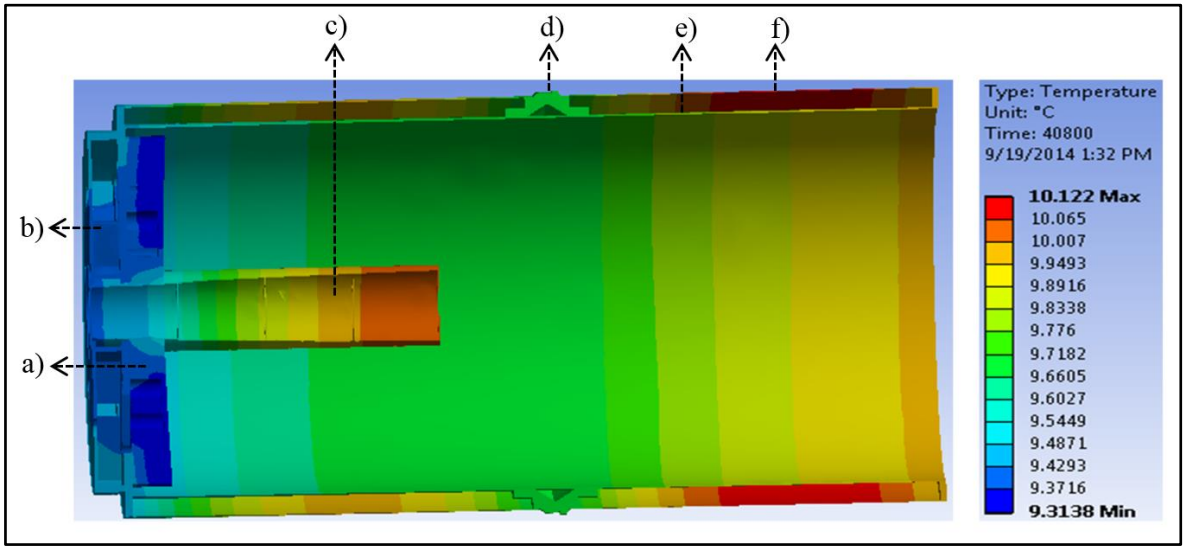

Figure 35: Cross-section of the assembled telescope component materials showing the simulated thermal variations as modelled by ANSYS. The symbols a), b), c), d), e) and f) denotes the 1-m primary mirror, mounting plate, baffle tube, middle outer ring, inner tube surface and outer tube surface respectively.

Further, a slight increase of ~0.23 ºC of the thermal variations is seen on the steel mounting plate where the mirror rests. The minimal variations revealed by the two aforementioned components are in contrast with those on the tube structure (Figure 35). The

tube structure including the baffle tube (which are both of aluminium T6 7075) had the highest thermal variations in the range 9.54 ºC to 10.12 ºC with respect to T_{∞}. In particular, the baffle tube is surrounded by a very good insulator (i.e. Zerodur mirror material) which reduces heat transfer at the bottom side of the tube; this as a result, makes the top part of the baffle tube to be more exposed to ambient air, hence it appears warmer. Additionally, the isotherms along the tube suggest that the thermal variations could be unidirectional, propagating from the 'open' front-end of the tube toward the 'closed' back-end where the primary mirror and mounting plate are structurally located. The evident decreasing temperatures toward the 'closed' back-end of the tube, suggest continuous (natural) heat losses as the thermal energy propagates along the optical tube in a unidirectional manner. These heat losses along the tube could have been accelerated by the contacting middle outer ring surface which is made of steel, coupled with dissimilar thermal properties relative to the aluminium tube.

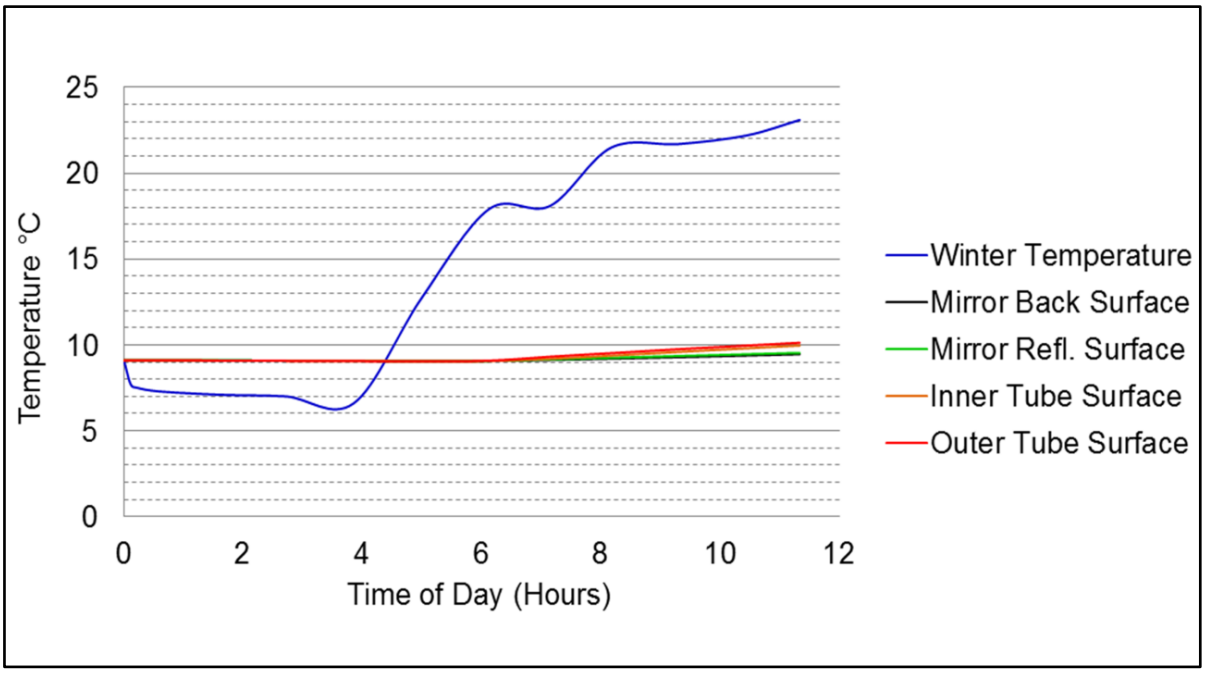

Figure 36: Temporal thermal variations on the tube and mirror surfaces in relation to $\boldsymbol{T}_{\infty}$ typical of the HartRAO site, during the time period 00:00 and 11:30 a.m. for a particular day in June. The thermal variations were probed from Figure 35 only for the abovementioned surfaces.

Take note that the tube design consists of two layers or surfaces, i.e., the outer shell and inner shell, both made of thin aluminium; thus leaving an open region between the surfaces for insulation purposes. This is evident in Figure 35 where the relative thermal gradients on the inner and outer shells respectively can be seen clearly. Furthermore, the thermal variations probed specifically from the mirror and optical tube surfaces revealed a total temperature

gradient of ~ 1 ºC (Figure 36), meaning that we can generally expect these component materials of the assembly to respond very slowly to T_{∞}. However, thermal regulatory measures may be necessary to ensure these variations are equalized and kept to a minimum as much as possible i.e., < 1 ºC (Murphy Jr et al., 2008) to allow excellent telescope pointing (Mittag et al., 2008), thereby increasing the chance of being on-target with the retroreflectors located on the lunar surface (Combrinck, 2014).

4.1.2. Analysis of thermally-induced deformations

The thermal analysis results presented in Figure 35 were used to estimate the total thermally-induced deformations of the telescope structure in x, y and z directions (Figure 37). Figure 37 illustrates the total deformations in the range 2.9 μm to 40.7 μm spanning the time period 00:00 and 11:30 a.m. In particular, the resistance against temperature change (denoted ΔT) by the mirror shows virtually zero localised deformations of the mirror as well as its mounting plate (Figure 37). These observations concur with modelling studies on the thermal expansion of Zerodur glass material at varying temperature profiles (i.e., between 0 ºC and 50 ºC) which showed no radial variations and excellent homogeneity (Jedamzik et al., 2010). However, the magnitude of the error contribution from the derived total deformations of the tube assembly is yet to be investigated for LLR telescope pointing at HartRAO.

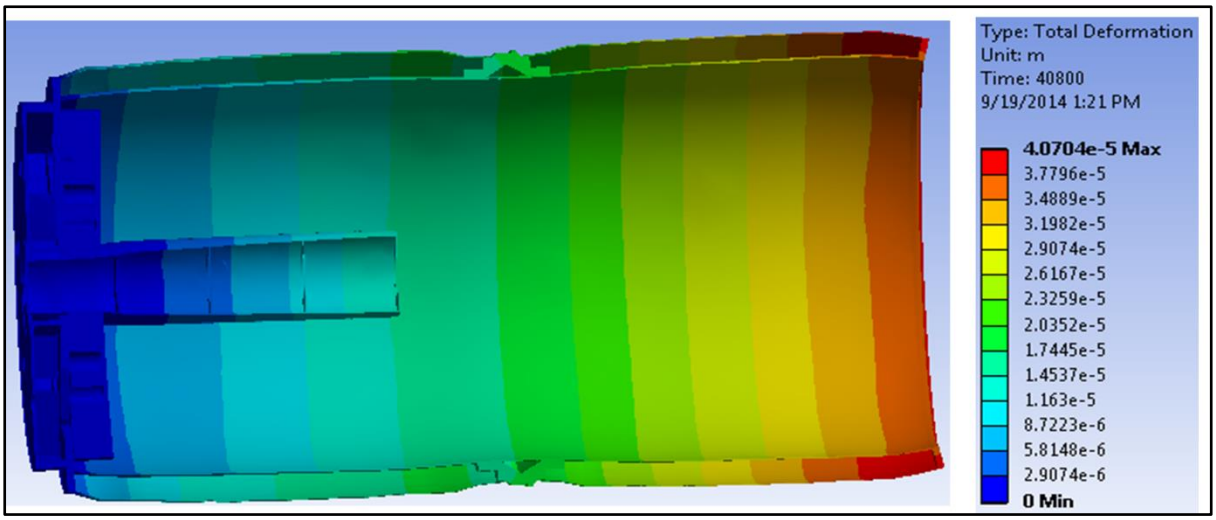

Figure 37: A cross-section of the telescope component materials showing the thermally-induced structural deformations in x, y and z directions.

The effects of the derived thermal variations (Figure 35) are largely evident along the edges of the tube surface through material expansion (Figure 37); and thus, have been reported elsewhere to be a significant source for a misalignment of the optical axis to the telescope tube axis (see Shinnaga et al. (2004) and Mittag et al. (2008)). In this context, the optical axis entails the correct position of the spider assembly carrying the secondary focus mirror (not shown in Figure 37) in relation to that of the primary mirror. The secondary mirror is attached to the front of the optical tube using a spider assembly (this allows centring and focussing). Therefore, any slight deformations on the mirrors and/or materials holding the mirrors would potentially misalign the optical axis thereby contributing to pointing errors and focussing problems during ranging. These findings call for the development of a thermal dynamic model which can compensate for structural misalignments due to thermal variations.

4.2. Thermal analyses of the LLR telescope composite structure

For a T_{∞} profile that varied from 9.1 ºC to 23 ºC at the site for a half day (00:00 – 12:00), the resulting minimum and maximum thermal variations measured at 12:00 midday across the telescope composite structure were in the range of 9.11 ºC to 10.03 ºC respectively (Figure 38). For a full day, T_{∞} profile spanning 00:00 – 23:59 the resulting range of thermal variations measured at 23:59 nighttime across the telescope composite structure was 9.12 ºC to 9.86 ºC (Figure 39). The discrepancy between the thermal variations depicted in multicolor isotherms on Figure 38 and Figure 39 indicate that the telescope experience more thermal variations (and related structural deformations depicted in Figure 37) during day time compared to nighttime. Further, it is evident that the thermal response time varies per component material primarily due to their respective thermal properties.

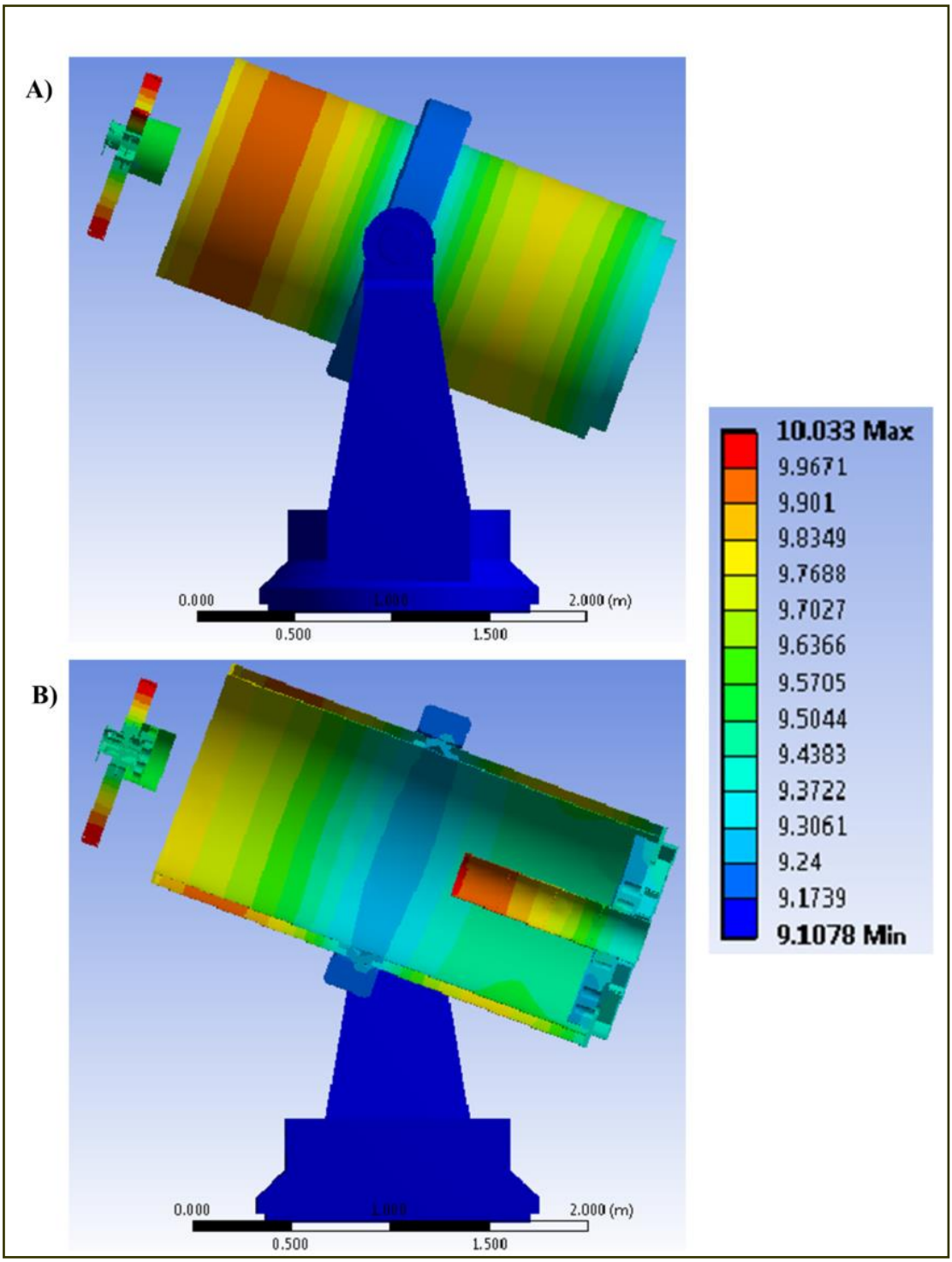

Figure 38: Full (A) and cross-section (B) of the telescope composite structure indicating the resulting thermal variations measured at 12:00 midday on the telescope components, in response to the T_{∞} profile from the HartRAO site for the time period 00:00 – 12:00. The thermal variations (°C) are represented by different coloured regions, each colour being an isotherm region; hence more colours correspond to more variations. Note the spider assembly in exploded view for legibility.

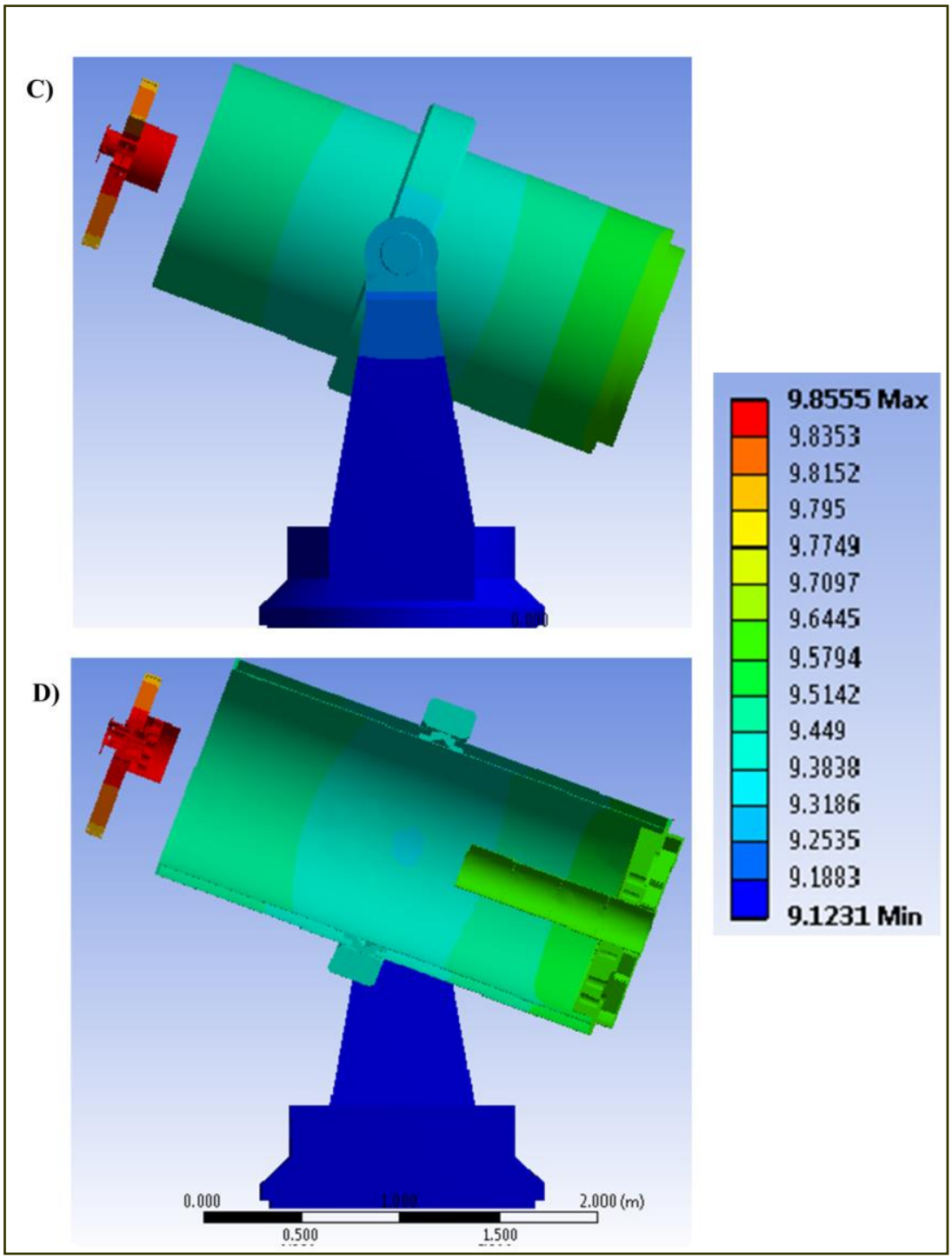

Figure 39: Full (C) and cross-section (D) of the telescope composite structure indicating the resulting thermal variations measured at 23:59 night-time on the telescope components, in response to the T_{∞} profile from the HartRAO site for the time period 00:00 – 23:59. The thermal variations (°C) are represented by different coloured regions, each colour being an isotherm region; hence fewer colours correspond to fewer variations. Note the spider assembly in exploded view for legibility.

In particular, the spider assembly and outer tube surface had the largest range of thermal variations i.e. greater than absolute 1 ºC with corresponding high standard deviations (Table 6) and thus, could be the main areas on the telescope where most thermal variations are likely to occur. The primary mirror surface including its mount or support structure responds slowly to T_{∞} with thermal variations of about 0.6 ºC (Table 6). In particular, these thermal variations had low variability (i.e. standard deviation) of 0.26 ºC and 0.24 ºC respectively (Table 6). Furthermore, the fork assembly (comprising the fork arms, elevation and azimuth mounts) had the smallest range of thermal variations (0.22 ºC) coupled with the lowest variability of 0.091 ºC.

Table 6: Descriptive statistics computed from the values of the telescope thermal state measured between 00:00 - 23:59. The sample size comprised of 145 recordings (°C) of the thermal state of the telescope composite structure taken at a sampling interval of 10 minutes within the time period of 00:00 – 23:59. The standard deviation indicates the variability of the 145 telescope thermal state values that were measured every 10 minutes throughout the day.

Model Input Variables	**Range (max-min) of thermal variations ºC**	**Average thermal variation ºC**	**Standard deviation of thermal variations ºC**
Ambient Air	23.2-6.4 = 16.8	13.92	6.051
Telescope components			
Spider Assembly	10.29-9.042 = 1.248	9.680	0.445
Outer Tube Surface	10.14-9.076 = 1.064	9.587	0.374
Inner Tube Surface	10.06-9.073 = 0.987	9.537	0.356
Secondary Mirror Reflective Surface	9.874-9.037 = 0.837	9.497	0.346
Primary Mirror Reflective Surface	9.719-9.072 = 0.647	9.416	0.261
Primary Mirror Support/Mount	9.637-9.062 = 0.585	9.377	0.241
Ring Support	9.440-9.091 = 0.349	9.261	0.147
Fork Assembly	9.320-9.099 = 0.221	9.194	0.091

The extent of thermal variations experienced by the individual telescope components including their thermal behaviour given the full-day T_∞ profile of the HartRAO site is graphically shown in Figure 40.

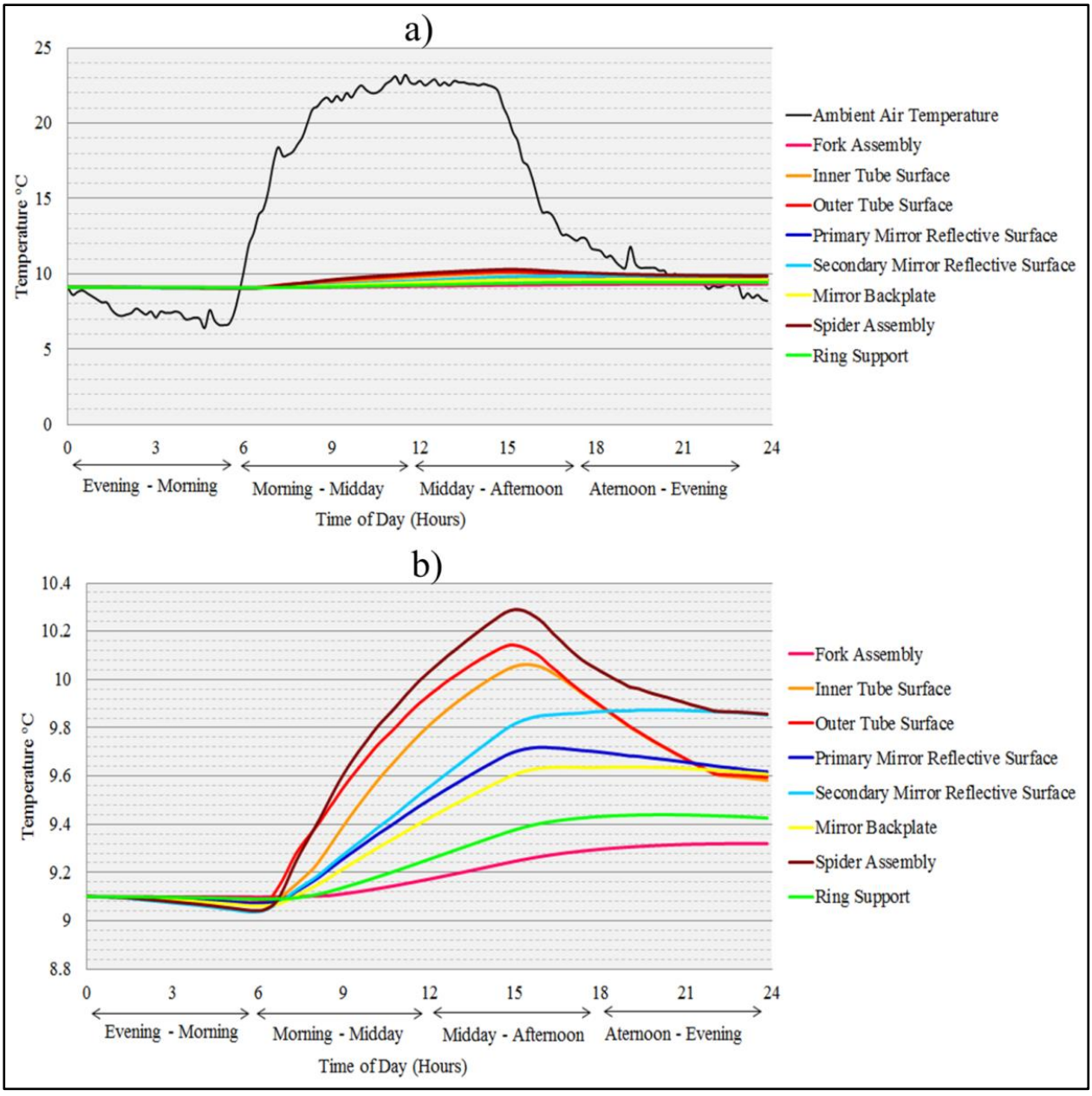

Figure 40: (a) Temperature changes measured at 10 minute intervals on the telescope component materials in relation to $\boldsymbol{T}_\infty$ typical of the HartRAO site during the time period 00:00 and 23:59 for a particular full-day in June. These temperature changes represent the thermal variations depicted in Figures 6 and 7 for the considered component materials; (b) Thermal variations in (a) shown in exploded view.

The sharp increase in T_∞ of the morning hours triggered the temperature change of all telescope components, which attempts to thermally respond to the T_∞ profile (Figure 40). Further, the continual rise of T_∞ particularly toward midday and early afternoon appears to trigger more thermal variations of the telescope components, with peak variations observed around 15:00 in the afternoon (Figure 40). During this time, we can expect the thermal state of the telescope composite structure not to be equal, coupled with high thermal variations (of some components) exceeding 1 ºC. While temperature of the telescope components collectively attempts to follow the decrease in T_∞, it will be interesting to observe the time it takes for the telescope's thermal state to reach internal equilibrium naturally, particularly post-midnight (Figure 40).

In overall, the thermal variations depicted in Figures 35, 36 and 37 have been shown in other studies (for example Atwood and O'Brien (2003); Zheng et al. (2012); Tsela et al. (2016a); Wang et al. (2018)) to have the potential to induce structural displacements that could impact on the mirror reflective surface, link length between mirrors and consequent defocus of the lens. As a result, if such thermally-induced displacements are not properly accounted for, they could be detrimental to the required pointing accuracy of the HartRAO LLR optical telescope.

In particular, the corresponding range values of the secondary mirror indicate that it could be warmer than the primary mirror at end of day (Table 6; Figure 40). This outcome is partly due to the encapsulation of the secondary mirror within the spider assembly, and more importantly, the mechanical composition of the spider assembly (particularly at the centre where the mirror is mounted) appears to be manufactured in a manner that traps heat according to our thermal simulations (Figure 39). On the other hand, the primary mirror's range values (Table 6) indicate that, towards the end of day i.e. 23:59 when T_∞ has dropped, the primary mirror would be warmer than any of its contacting surfaces (Figure 39; Figure 40). The apparent thermal variations of the mirrors are consistent with the thermal properties of the Zerodur mirror, especially their low *k* and CTE values (Jedamzik et al., 2010).

4.3. Mock-up tube experiments

4.3.1. Mock-up tube RTD measurement

Results of temperature measurements acquired using the 64 RTD sensors mounted onto the outer surface of the mockup tube, reveal tube overall thermal variations of about 2 ºC (Figure 41). For illustration purposes, the sample of measurements were taken in the morning hours of 5th May 2016 (winter season) i.e., for the time period of 05:25 - 05:55 a.m. and 06:45 - 07:15 a.m. in a fairly stable environment. The results of the tube experiment showed that there was no significant change on the tube thermal variations (Figure 41). Further, during the night or early morning hours prior to sunrise, the tube surface temperature generally tends to be constant, with virtually no bulk temperature fluctuations along the tube surface detected by the RTD sensors (Figure 41 (a)).

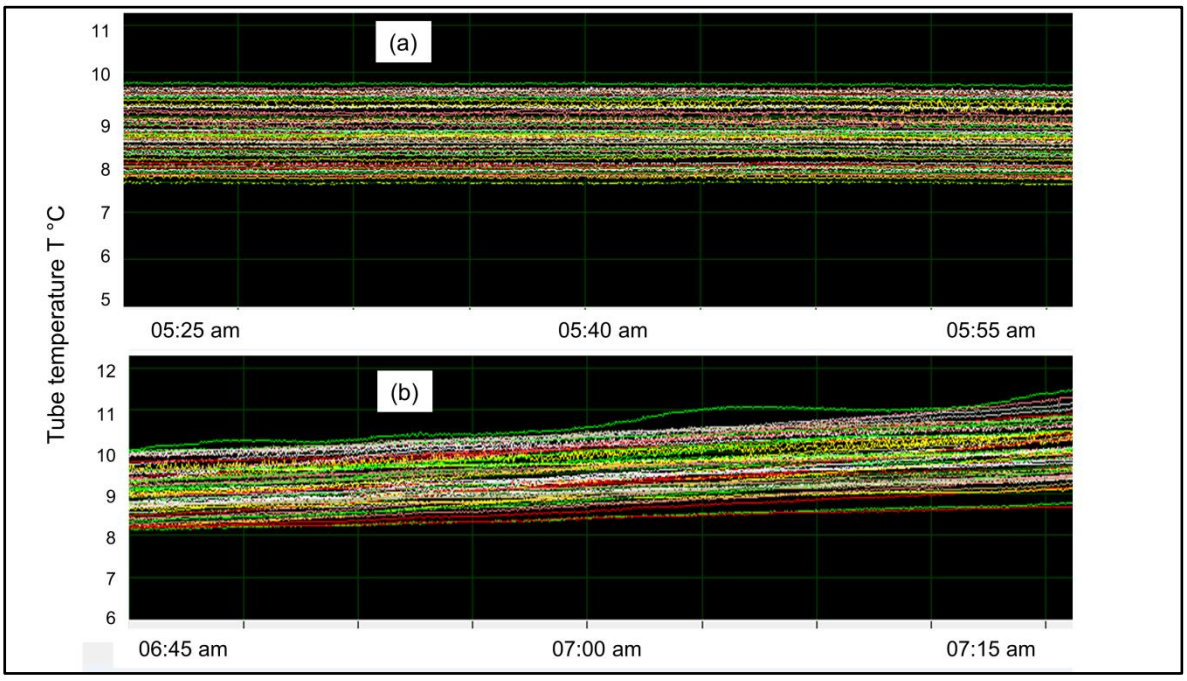

Figure 41: Recorded temperature (ºC) versus time (in hours) of 64 RTD sensors.

A subsequent gradual rise of thermal variations can be observed which represents the tube's thermal response to the fluctuations in T_{∞} (Figure 41 (b)). Additionally, this gradual rise is due to the tube's horizontal position (see section 3.4.4.1) which mainly exposes the upper arc of the tube surface to incoming solar radiation. Notably, the acquired tube-sensor temperature readings do not entirely overlap with each other and thus, the little gaps in between, could be an indication that the temperature along tube structure is not entirely the same (Figure

41). For example, this assertion can be corroborated by the simulation results which showed varying temperatures between the middle and front-end of the tube (see Figure 38 and Figure 39). In addition, the observed thermal behaviour of the tube from this experiment (Figure 41) show similar trends with the thermal simulation profile of the outer tube surface at corresponding times (Figure 40 (b)). During the night or time period considered, the tube temperature resembles an isotherm coupled with minor variations of the tube temperature sensor readings. In overall, the tube-sensor readings showed tube thermal variations of approximately 2 ºC coupled with an error of ±0.5 ºC associated with each RTD sensor. These findings indicate that the RTD sensors used, have the potential to acquire accurate temperature measurements, and can therefore be used on the actual components of the LLR telescope as well as testing the proposed thermal model.

4.3.2. Mockup tube temperature interpolation

Figure 42 show results of the measured T_{∞}, tube average temperatures and the interpolated tube average temperature, spanning different time intervals in the evening of the 24th, 25th and 26th September 2016. Nighttime was considered suitable for this for experiment to test the interpolation procedure due to minimal temperature fluctuations. In particular, the measured tube average temperatures appeared to follow the intermittent fluctuations and general decline of T_{∞} at the site during the time period considered. In addition, this observation is partly corroborated by the virtually corresponding temperature variations (minimum-maximum) of for example, 17.51 - 22.94 °C and 13.20 - 17.32 °C of T_{∞}, and 17.29 - 23.11 °C and 13.35 - 17.45 °C of measured tube average temperatures, respectively (Figure 42 a and c).

The thermal properties of the mockup tube material used are such that, changes in measured tube average temperatures in response to T_{∞} are discernible after every 5 minutes (minimum) within the complete time interval considered (Figure 42). Such rapid thermal response time suggests that the (real) LLR tube structure can easily reach thermal equilibrium especially when T_{∞} is stable i.e. during nighttime. The minimum and maximum temperature differences between T_{∞} and average tube temperatures (either measured or interpolated) were found to be at about 0.5 °C (Figure 42 a) and 1 °C (Figure 42 b) corresponding to transient time periods of 19:15 - 19:20 and 00:30 - 00:35 respectively. These experimental findings imply that the thermal regulatory requirement of ≤ 1 °C (Tsela et al., 2016a) for thermal variations of the LLR tube assembly can be achieved.

On the other hand, Figure 42 also contains results of the interpolated tube average temperature profile for the 24 unmeasured locations on the tube. Clearly, the variation of this profile follows T_{∞} and also resembles the profile of the measured tube average temperature. The observed overlap between the profiles of measured and interpolated temperatures (particularly on Figure 42a and 42c) shows that the thermal distribution across the tube surface is isothermic during nighttime in contrast to daytime or early sunrise. Furthermore, the observed overlap could be an indication that the sensor placement including spacing and density on the tube is representative and provides a realistic picture of the tube thermal state.

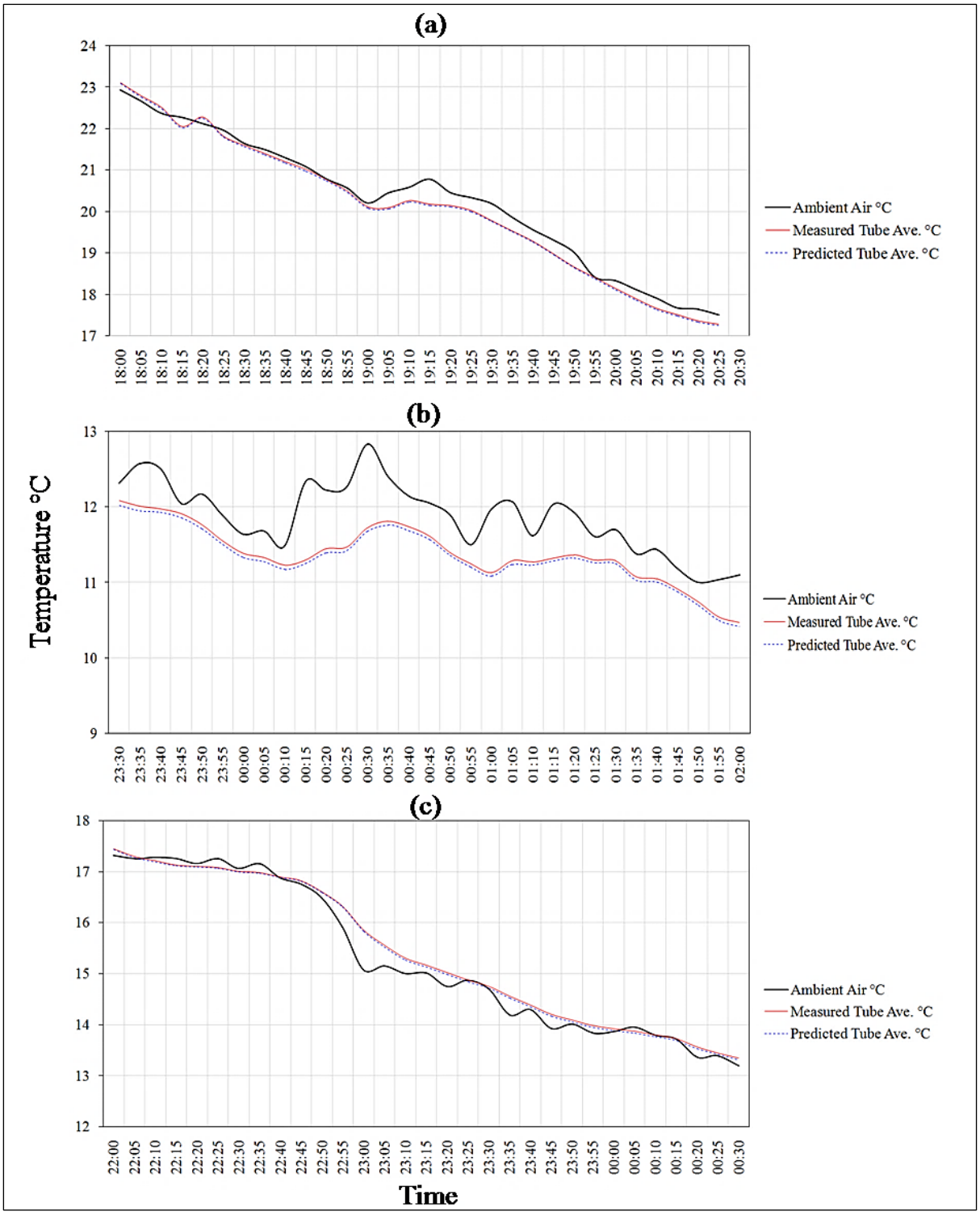

Figure 42: Temperature profiles of ambient air, measured and predicted tube-average temperature in the evening of the 24th (a), 25th (b) and 26th (c) September 2016

Figure 43 shows the computed RMSE variation of the interpolated tube average temperatures which indicates that, the applied interpolation algorithm in this study can be expected to predict temperature of the LLR tube structure at accuracies (RMSE) in the range

of 0.26 - 0.34 °C (a), 0.29 - 0.37 °C (b) and 0.24 - 0.32 °C (c) respectively, during nighttime. In particular, the targeted interpolation accuracy of at least 0.3 °C was achieved. Virtually similar observations were reported in Greve et al., (2005) and Greve and Kaercher, (2009) whereby the RMSE in the range of approximately 0.2 - 0.3 °C was found for the FE model structure of the IRAM 30 m radio telescope.

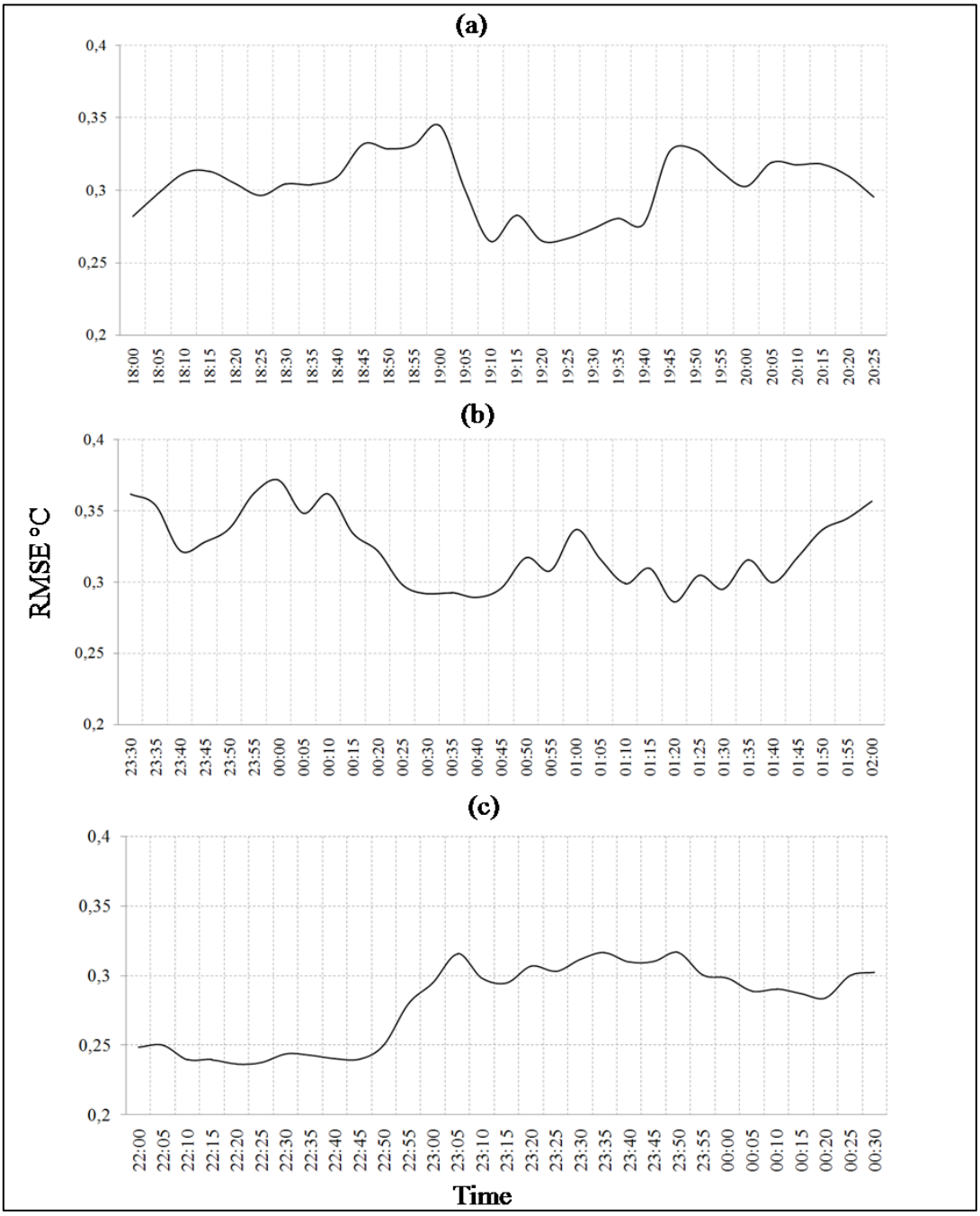

Figure 43: Root mean squared (RMS) error variation of the interpolated tube-average temperatures in the evening of the 24th (a), 25th (b) and 26th (c) September 2016.

In this experiment, three exponential values of p which represent the order of polynomial (Equation (26)) were tested in-order to find a suitable p value that gives better interpolation results. Table 7 depicts the test results of the exponent p used in the interpolation algorithm, and as a result the exponential p value of 2 was found to produce the smallest interpolation error (i.e. RMS) relative to the p values of 1 and 3 when tested on three night-time data sets. Furthermore, Table 7 show that, in overall, the smallest and largest RMS we can expect for the interpolation algorithm is 0.24 °C and 0.37 °C respectively, when a p value of 2 is applied.

Table 7: Summary of test results of the exponent $\boldsymbol{p}$ used in the interpolation algorithm

	Date: 24 Sept 2016 Time: 18:00-20:25				**Date: 25 Sept 2016 Time: 18:00-20:25**				**Date: 26 Sept 2016 Time: 22:00-00:30**		
$1 \leq p \leq 3$	$p = 1$	$p = 2$	$p = 3$		$p = 1$	$p = 2$	$p = 3$		$p = 1$	$p = 2$	$p = 3$
Min RMS °C	0,27	0,26	0,28		0,32	0,29	0,30		0,25	0,24	0,25
Max RMS °C	0,37	0,34	0,35		0,42	0,37	0,38		0,35	0,32	0,32
Median RMS °C	0,33	0,30	0,32		0,35	0,32	0,33		0,32	0,29	0,30

These findings suggest that the applied interpolation algorithm (Equations (24) - (26)) is likely to predict temperatures of the telescope composite structure accurately, particularly during nighttime. Furthermore, the interpolated temperatures combined with RTD measured temperatures provided a realistic temperature distribution of the mock-up tube thermal state within the considered times. Further research would be to align interpolated temperatures with the FE model nodes of the LLR telescope tube (and other components) so as to ensure that temperatures at all nodes without RTD sensors can be estimated. These findings constitute an important parameter in further testing and completing the execution of the proposed thermal model presented in section 3.4.3.

4.4. LLR tube experiments

4.4.1. LLR tube RTD measurements

Figure 44 show the daily temperature variations of the LLR tube and T_∞ at the HartRAO site, sampled every 5 minutes for 2 successive days i.e. 30 Nov 2018 – 01 Dec 2018. In particular, the LLR tube measurements were averaged from a distribution of 64 RTD sensors and sampled every 5 minutes. It is evident from Figure 44 that, the tube temperature follows variations of T_∞ successively during day- and nighttime. The rapid thermal response of the tube

is largely due to its thermal material properties, discussed earlier (Tsela et al., (2016a)). For example, during daytime the tube average temperature can rise above 30° C which is at least 4° C higher than T_{∞} especially, between 10h00 and 17h00 when the tube is exposed to incoming radiation. This temperature may have increased further, if it was not for the double layer structural design of the tube (Tsela et al., 2016a), which insulates the inner surface or first layer of the tube where the RTD sensors are mounted. Nonetheless, a tube average temperature of about 30° C (is often coupled with tube material expansion), which may be sufficient to misalign the tube optical axis, thus have been shown elsewhere (Mittag et al., 2008) to cause azimuth and elevation offsets of about of 40″ and 10″ respectively, during pointing.

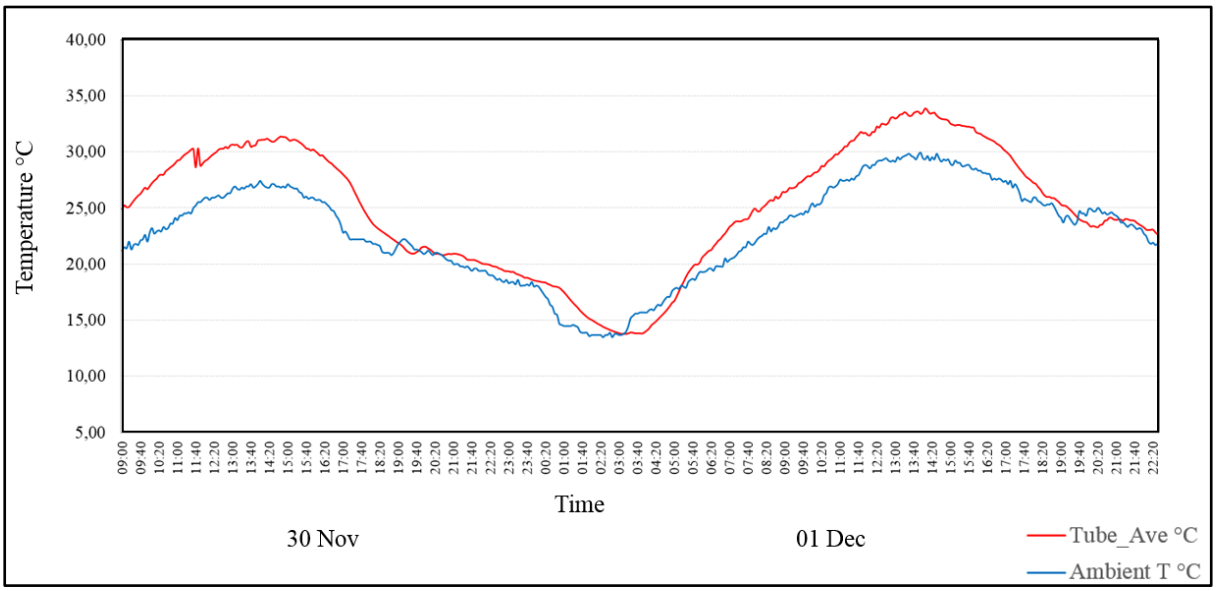

Figure 44: Illustration of the measured average temperature of the LLR tube (Tube_Ave °C) and the ambient air temperature (Ambient T °C) for HartRAO sampled every 5 minutes, for the times and days shown.

On the other hand, during nighttime particularly from around 19h00 to the late night hours, the tube temperature and T_{∞} generally overlaps. This could be due to the ambient temperature stability or micro T_{∞} variations at those times, which enable the tube structure to assume isothermic thermal behaviour (also see Figure 39 in section 4.2). The resulting nighttime discrepancy between tube temperature and T_{∞}at the considered times can be expected to be as low as ~1° C (Figure 44). In overall, these findings constitute an important input for the analysis of tube displacements due to its temperature fluctuations.

4.4.2. Thermally-induced tube displacements

4.4.2.1. Analysis of relative displacements of the LLR tube

The Total Station's repeatability used for the measurements of relative tube displacements is at the 1 mm level, but due to its high sampling rate will provide sub-mm ranges statistically (Figure 45). In particular, repeated laser distance measurements to the optical centre of the prisms mounted on the LLR telescope tube (Figure 45), yielded 3-dimensional distance variations between the true centre and the apparent centre of the prisms, due to the assumed tube thermal variations.

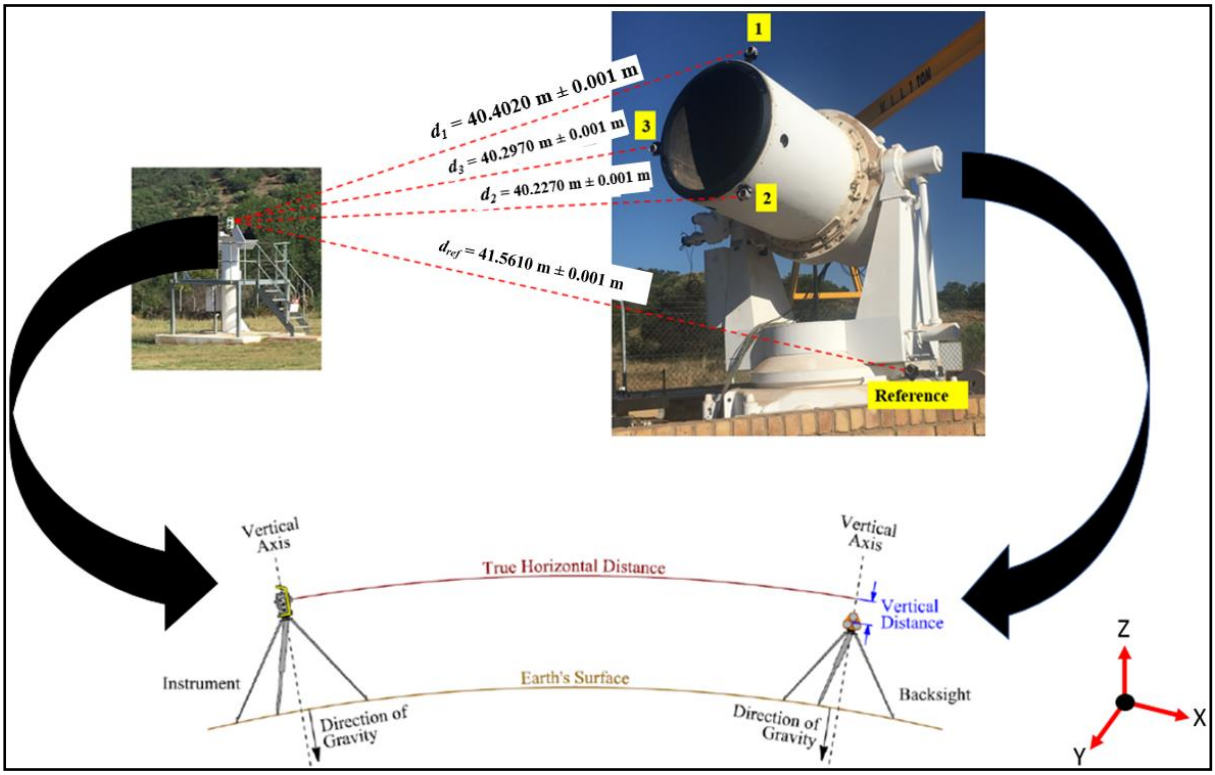

Figure 45: Illustration of the LLR tube displacement monitoring experiment based on the site-based Leica Nova MS50 Multi-Station and 4 Leica GPH1P Prism Precision Reflectors mounted on the telescope tube front and base. The horizontal distance (d_i) ± Total Station measurement accuracy between the multi-station and the respective prisms mounted on the telescope is shown in the figure. A theoretical representation of the Earth curved surface and the parallel horizontal distance are also shown (Torge and Müller, 2012)

The measured displacements by the reference prism mounted on the telescope base structure (Figure 45), were deducted from the measured displacements by the 3 prisms mounted on the LLR front-end of the tube. The deduction process basically removed the contribution of the base structure displacements, from the tube measured displacements in the height (z),

easting (x) and northing (y) respectively. As a result, the relative displacements Δ, of the tube front-end are presented in Figure 46 to Figure 48 over two consecutive days i.e. 30 Nov 2018 – 01 Dec 2018.

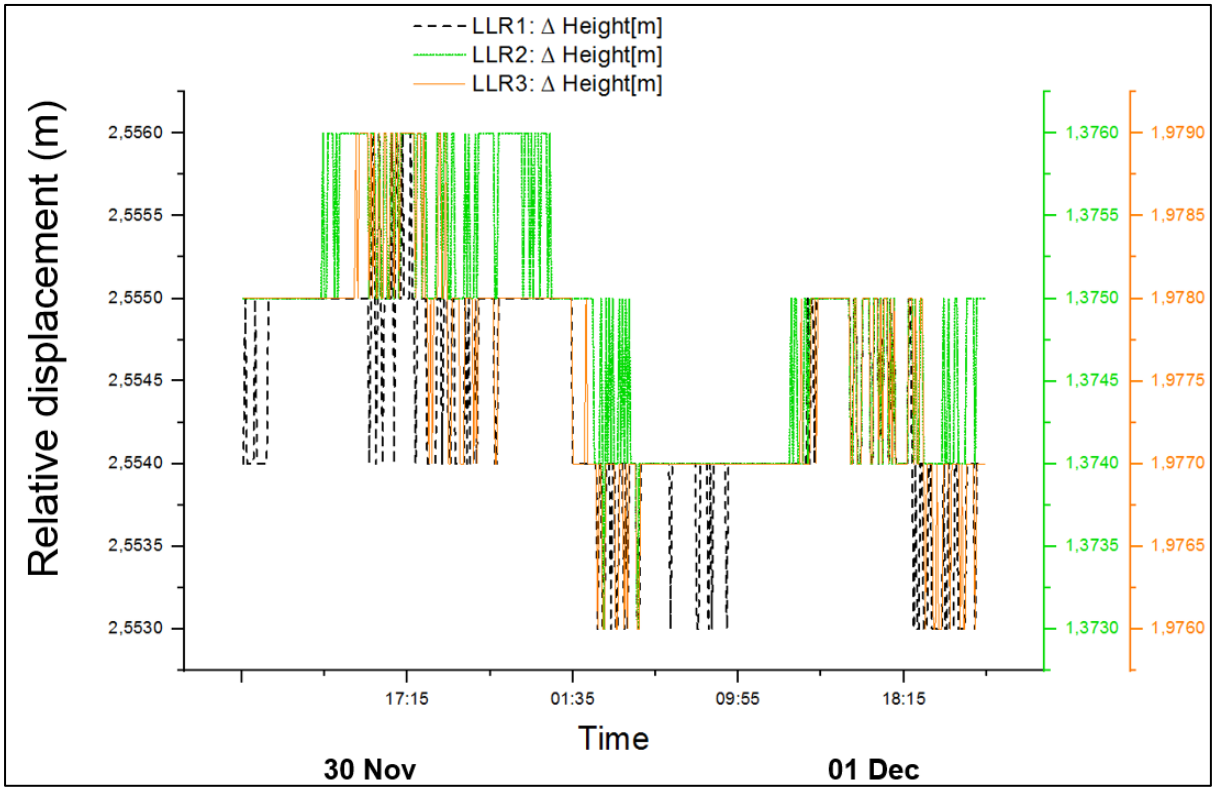

Figure 46: Displacements of the tube front-end, sampled every 5 minutes in the vertical (z) direction relative to the telescope base structure by use of 4 prisms (see Figure 45). LLR 1, 2 and 3 denote the respective positions of the 3 prisms mounted on the tube front-end.

Notable changes are evident on Figure 46 in the height relative displacements of the tube, measured simultaneously at prisms 1, 2 and 3 over the two-day period when the experiments were conducted. The temporal oscillations of tube relative displacements in the vertical direction appears evident across day-time to night-time (Figure 46). As a result, these oscillations may be attributed to the possible tube structural changes due to tube temperature variations (discussed later in section 4.4.2.2). For example, the variations (standard deviations are shown in Figure 49) of the relative displacements at prisms 1, 2 and 3 in the vertical direction were found to be 0.670 mm, 0.751 mm and 0.692 mm respectively. A difference is noted in the slightly higher variation of relative displacement at prism 2 and thus, gravity-induced deformation on the tube lower arc may have had an effect, as shown in Nkosi et al. (2016). Overall, this finding corroborates simulation results of the tube thermal deformations

presented in section 4.1.2 which depicted thermally-induced deformations of the front of the tube. Exposure of the tube front to incident solar radiation and T_{∞} (particularly during day-time) could have implications for the stability of the spider assembly and alignment of the optical axis (Figure 45). However, telescope pointing experiments would have to be conducted to investigate the influence of the reported relative displacements on the required pointing accuracy for the LLR HartRAO telescope.

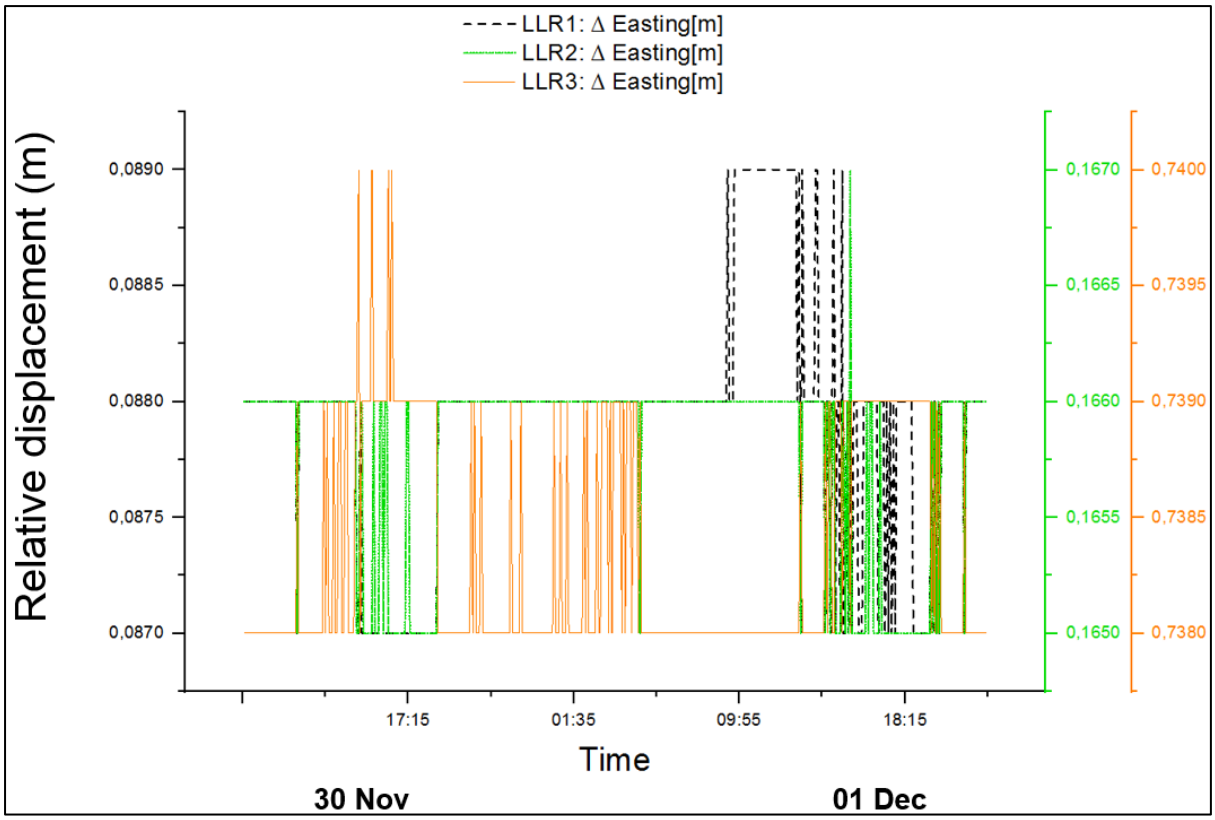

Figure 47: Displacements of the tube front-end, sample every 5 minutes in the easting (x) direction relative to the telescope base structure by use of 4 prisms (see Figure 45)). LLR 1, 2 and 3 denote the respective positions of the 3 prisms mounted on the tube front-end.

Furthermore, changes are also evident in Figure 47 in the easting (x) relative displacements of the tube, measured simultaneously at prisms 1, 2 and 3 over the two-day period when the experiments were conducted. In particular, the variations (i.e. standard deviation shown in Figure 49) of the relative displacements at prisms 1, 2 and 3 in the easting (x) direction were found to be 0.523 mm, 0.418 mm and 0.493 mm respectively. The temporal oscillations of the relative displacements (Figure 47) appeared modest and had lower variation compared to the vertical relative displacements.

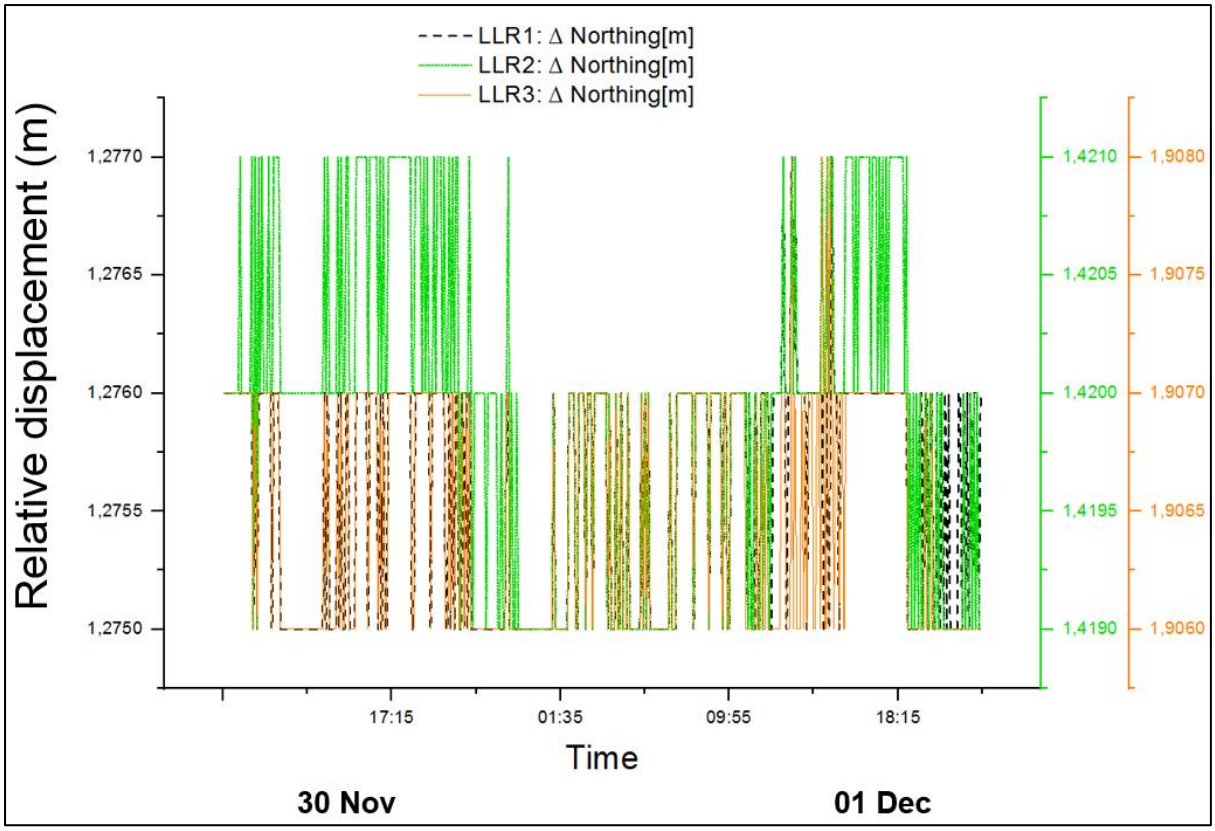

Figure 48: Displacements of the tube front-end, sample every 5 minutes in the northing (y) direction relative to the telescope base structure by use of 4 prisms (see section 3.4.4.4). LLR 1, 2 and 3 denote the respective positions of the 3 prisms mounted on the tube front-end.

Relative displacement of the tube in the northern (y) direction is also evident (Figure 48). More variation in temporal oscillations of relative displacement could be seen during day-time when the tube is exposed the incident solar radiation, and less during the late afternoon through to night-time, especially at prism 2. Furthermore, the variations (Figure 49) of the relative displacements at prisms 1, 2 and 3 in the northing (y) direction were found to be 0.513 mm, 0.691 mm and 0.518 mm respectively.

In overall, the height or vertical relative displacements had the highest variations i.e. of about 0.670 mm, 0.751 mm and 0.692 mm for the time period considered, compared to variations of relative displacements in the easting and northing directions (Figure 49). The second highest variations of relative displacements were in the northing direction, followed by the easting direction (Figure 49). Note, in this discussion the standard deviation of the relative displacements shown in meters (Figure 49) was converted into millimeters, simply for legibility of the variations.

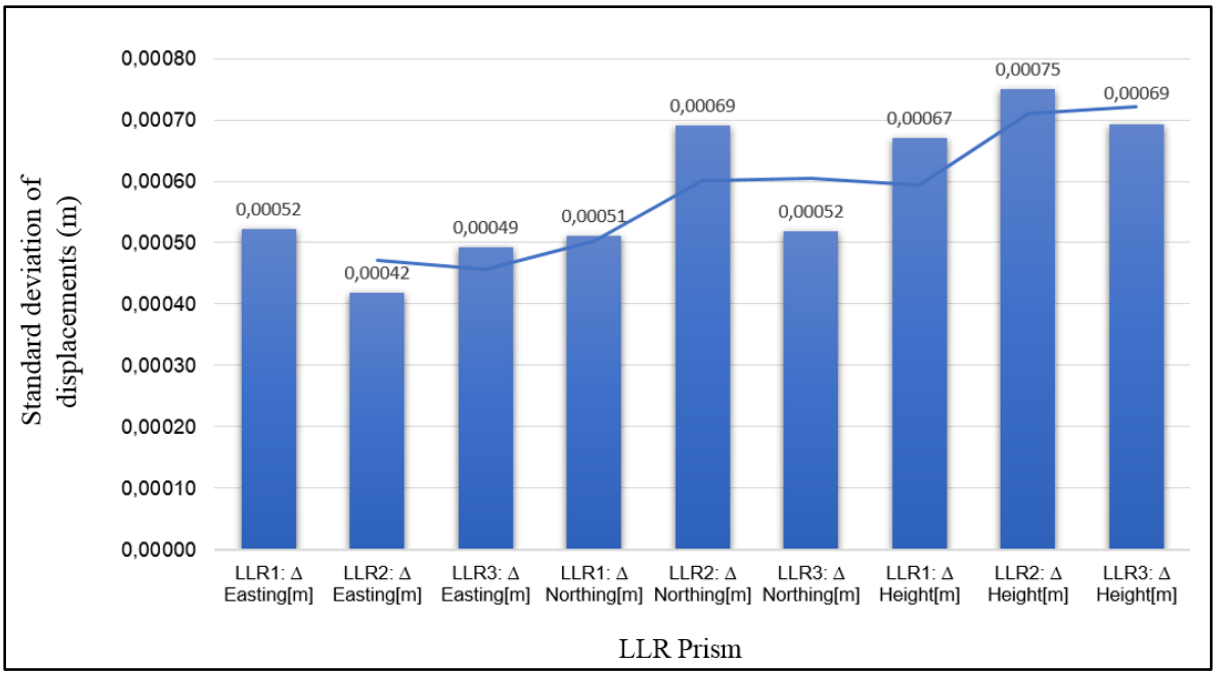

Figure 49: Standard deviation of the relative displacements in height (z), easting (x) and northing (y) at all 3 prisms mounted on the LLR tube structure.

Interestingly, these findings show that, the variations of relative displacements at prism 2 (LLR 2: Δ Easting: 0.418 mm, Δ Northing: 0.691 mm, Δ Height: 0.751 mm) were highest compared to those of prisms 1 and 3. This finding could be an indication of an area on the tube that undergoes more structural deformations. Considering the location of prism 2 at the lower arc of the tube front, this finding suggest there could be a combination of thermally-induced (Tsela et al., 2016a) and gravity-induced (Nkosi et al., 2016) deformations simultaneously happening on the tube, thus leading to more displacement compared to other areas on the tube front.

Furthermore, the measured variations of tube displacement at prisms 1 and 3 could be partially attributed to the tube's exposure to direct sunlight which: (i) transiently (from approximately 07h30 to 10h30 in the morning hours) irradiates the west-facing side of the tube where prism 3 is mounted, and (ii) lastingly (from around 11h00 to 17h30) irradiates the top and east-facing side of the tube where prism 1 is mounted, respectively. The observed variations of relative displacements across all 3 prisms suggest the tube structure expands in a radial manner (Figure 49). It is has been empirically shown that the high tube temperatures lead to thermal expansion of the tube, followed by displacements (Mittag et al., 2008) therefore, this could have been the case in our experimental results.

4.4.2.2. Analysis of thermally-induced tube displacements

Visual inspection of the time series of the overlaid (i) measured tube average temperature, (ii) ambient air temperature, and (iii) relative displacements of the tube in height, easting and northing; show that variations of relative displacements appeared to happen simultaneously with the successive peaks of both tube average temperature and ambient air temperature, T_{∞} (from Figure 50 to Figure 58). In particular, the relative displacements of tube height (Figure 50, Figure 51 and Figure 52) revealed a clearer pattern of variations in relation to tube average temperature. Furthermore, the relative displacements of tube height (especially in Figure 50 and Figure 52) show oscillations that correspond with increases and decreases of tube average temperature, particularly during the times 15:00 – 22:35 (30 Nov) and 12:40 – 22:00 (01 Dec).

Similar patterns are also evident for relative displacements of the tube toward the east in (Figure 54; Figure 55) particularly during the times 11:45 – 18:15 (30 Nov) and 13:45 – 20:15 (01 Dec). The relative displacements of the tube towards the north in Figure 57 had the finest oscillations in-relation to tube average temperature profile, virtually across the entire time series. These finding indicate that the tube undergoes structural changes (expansion and contraction) with change in temperature. The smallest variations in relative displacements of the tube were found to be 0.523 mm (east), 0.512 mm (north) and 0.670 mm (height) measured through LLR prism 1 whereas, the largest variations were reportedly 0.418 mm (east), 0.691 mm (north) and 0.751 mm (height) measured through LLR prism 2 (Figure 49).

This information could be used in guiding the efforts to determine the amount of correction needed to be fed into the LLR telescope pointing model (Combrinck, 2014) to counteract thermally-induced pointing offsets. The general idea would be to ensure an even distribution of temperature throughout the telescope tube (and mount assembly) through a microprocessor controlled venting system. Especially the areas where mechanical distortion would lead to optical collimation and alignment or focussing errors, such as the secondary mirror spider assembly should have no unevenly heated areas.

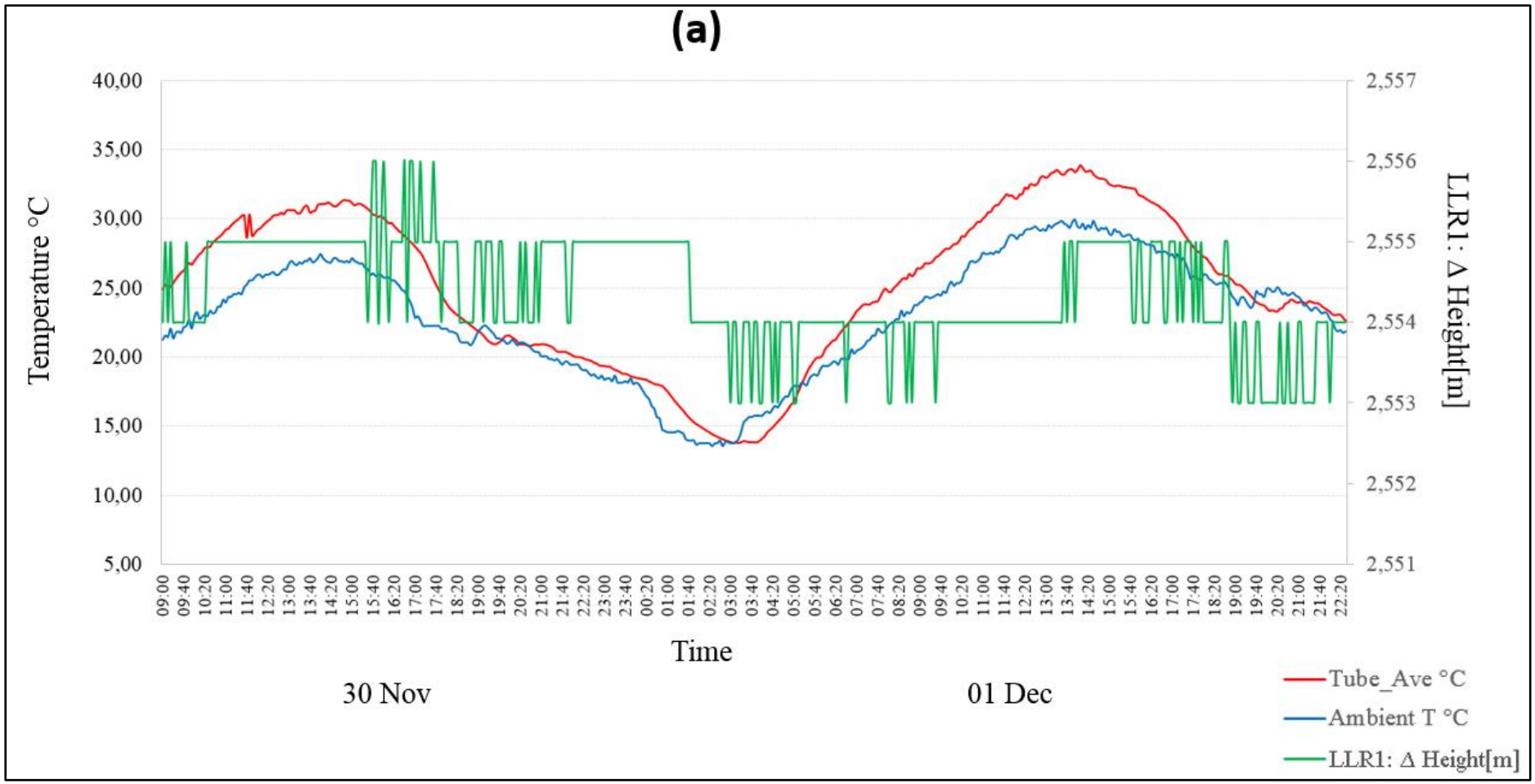

Figure 50: Time series of the (i) measured tube average temperature, (ii) ambient air temperature, and (iii) relative displacements of tube height at the location where the LLR1 prism was mounted.

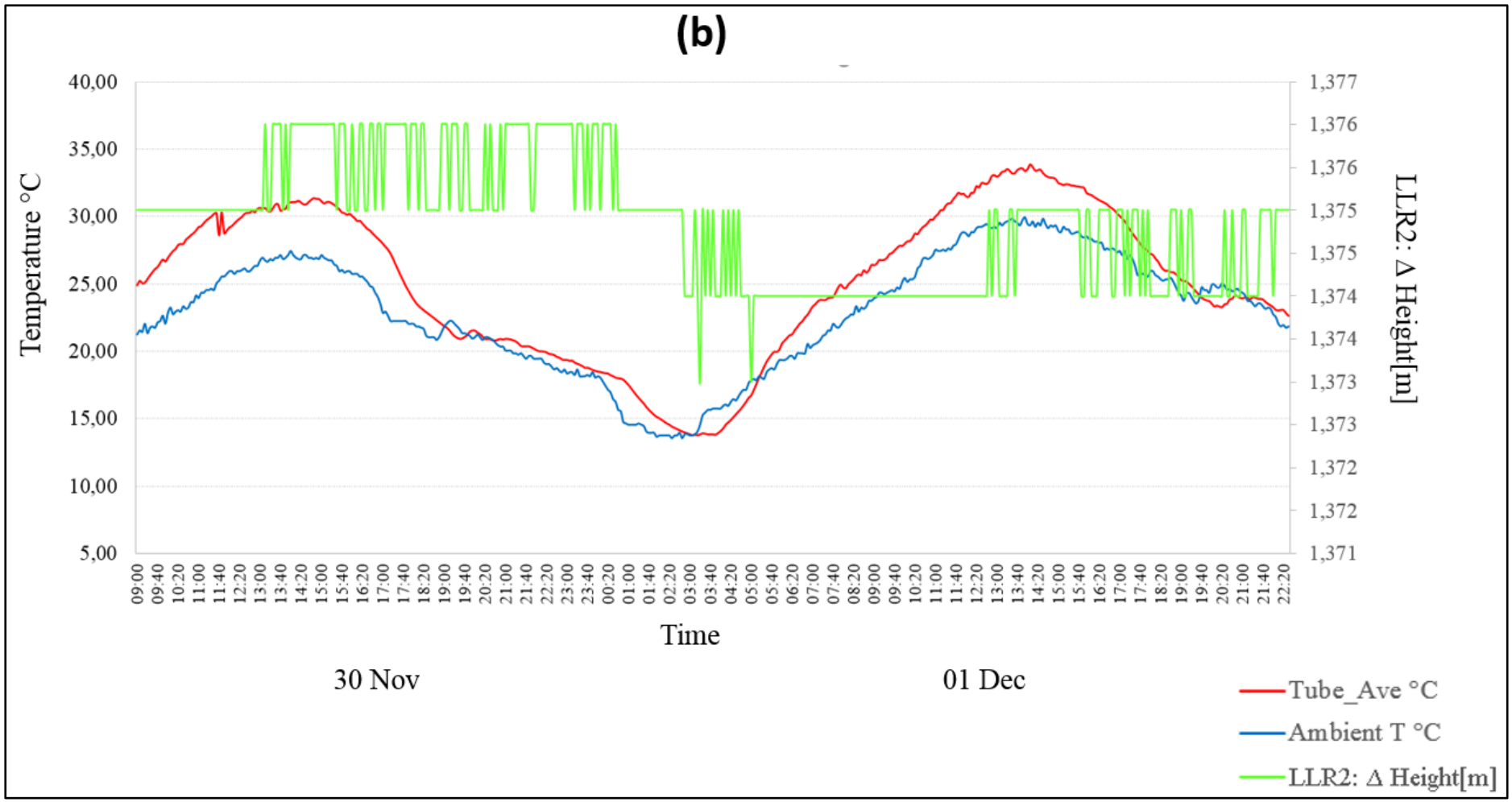

Figure 51: Time series of the (i) measured tube average temperature, (ii) ambient air temperature, and (iii) relative displacements of tube height at the location where the LLR2 prism was mounted.

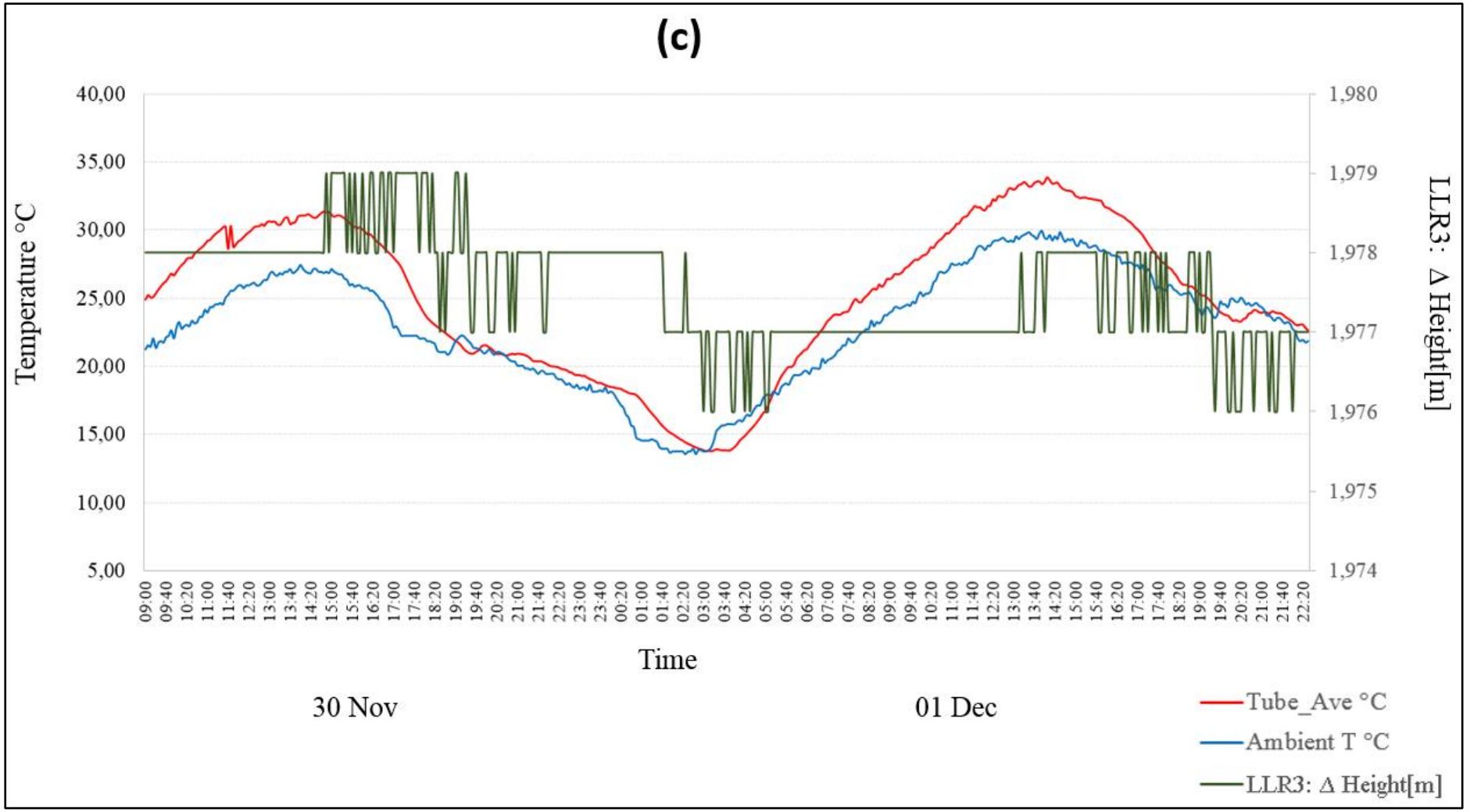

Figure 52: Time series of the (i) measured tube average temperature, (ii) ambient air temperature, and (iii) relative displacements of tube height at the location where the LLR3 prism was mounted.

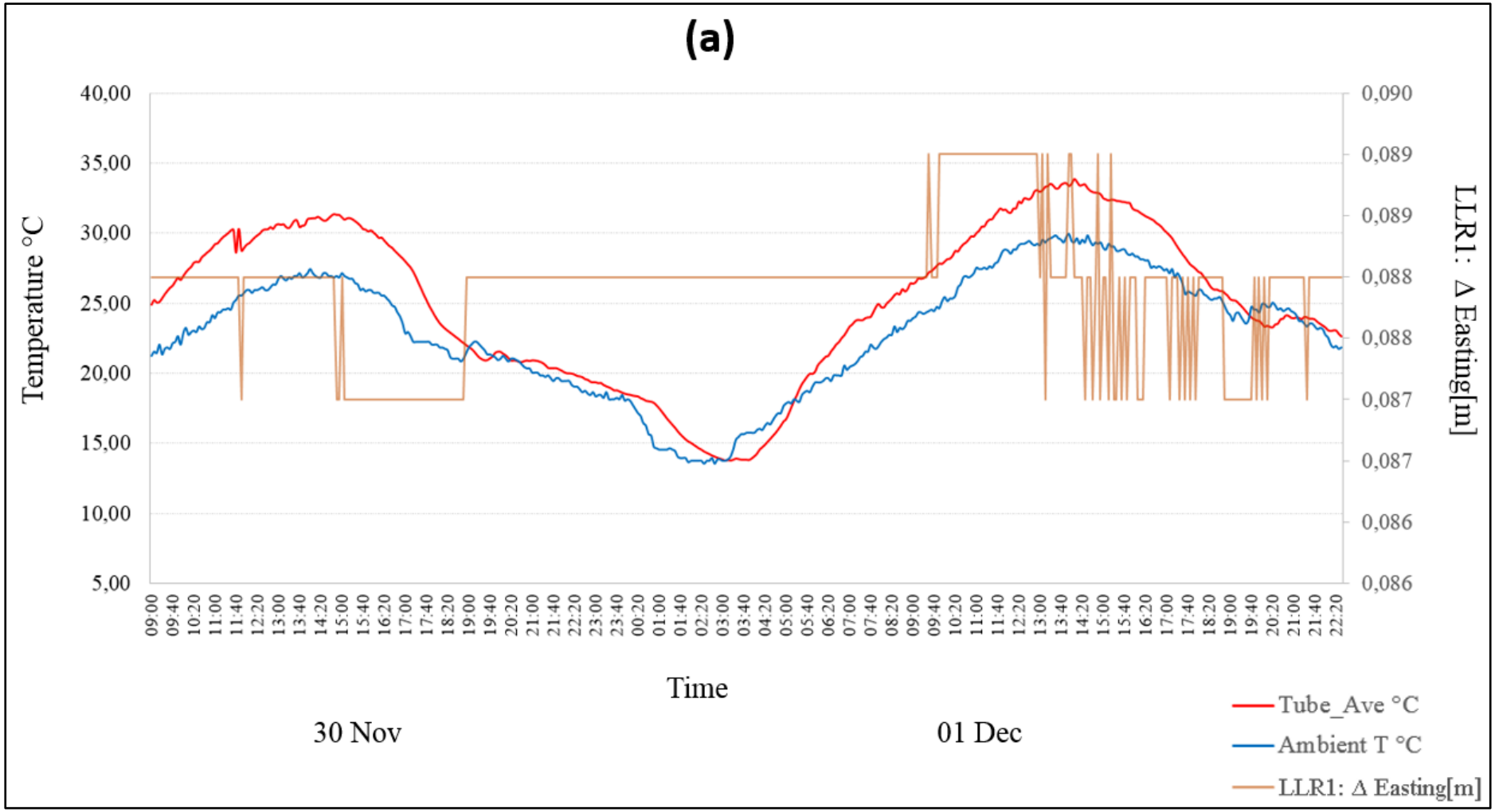

Figure 53: Time series of the (i) measured tube average temperature, (ii) ambient air temperature, and (iii) relative displacements of the tube toward the east at the location where the LLR1 prism was mounted.

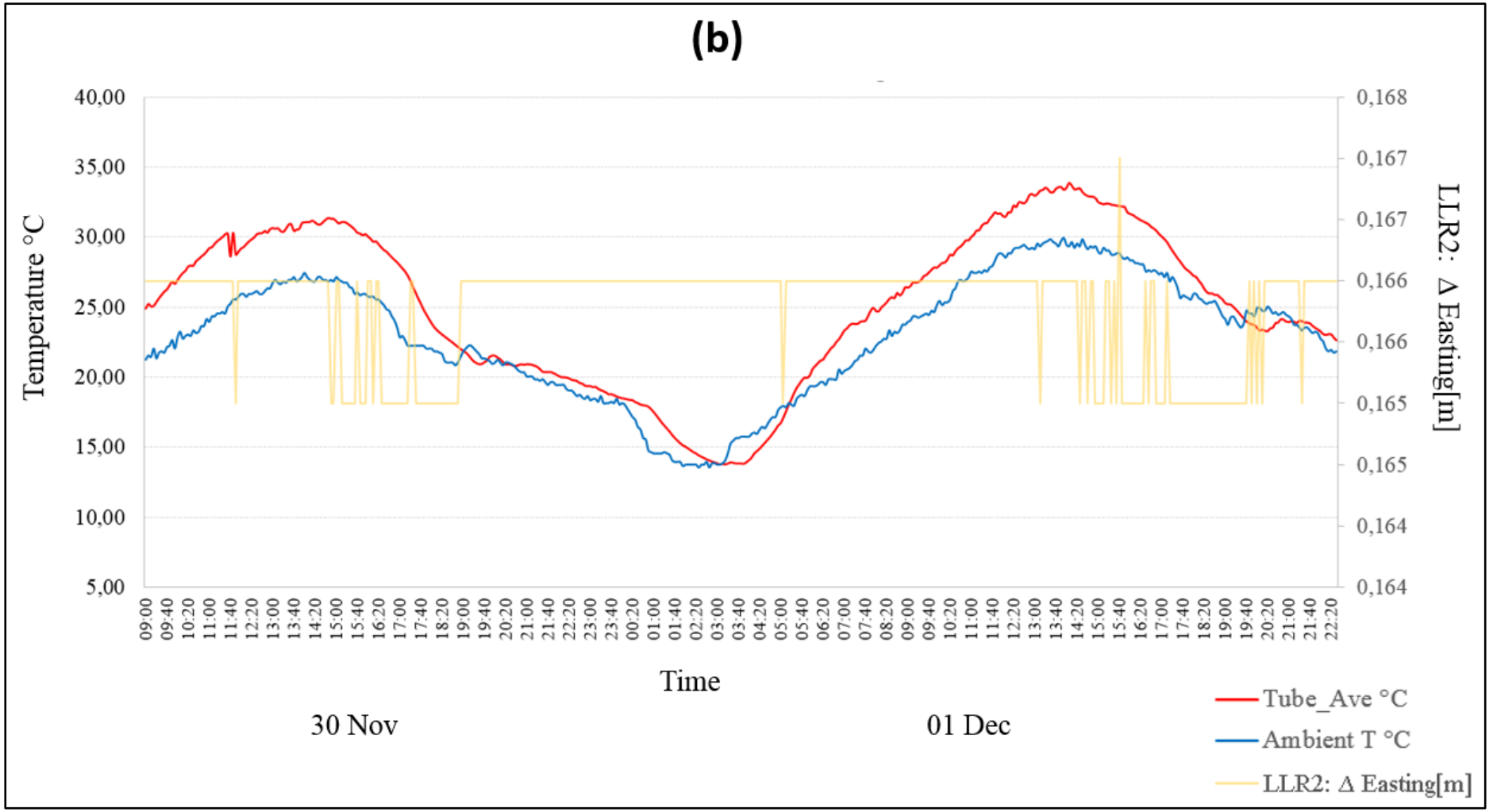

Figure 54: Time series of the (i) measured tube average temperature, (ii) ambient air temperature, and (iii) relative displacements of the tube toward the east at the location where the LLR2 prism was mounted.

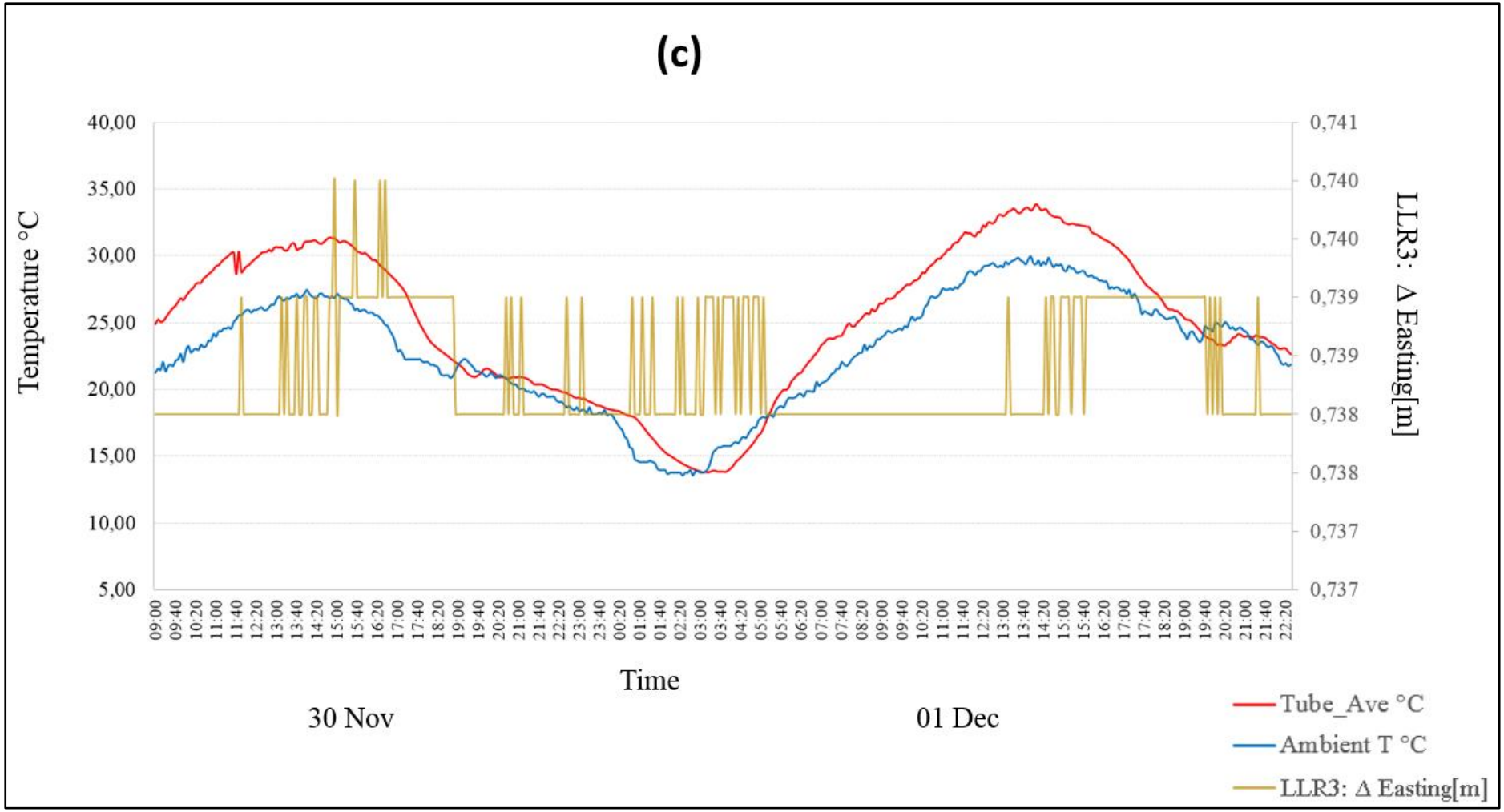

Figure 55: Time series of the (i) measured tube average temperature, (ii) ambient air temperature, and (iii) relative displacements of the tube toward the east at the location where the LLR3 prism was mounted.

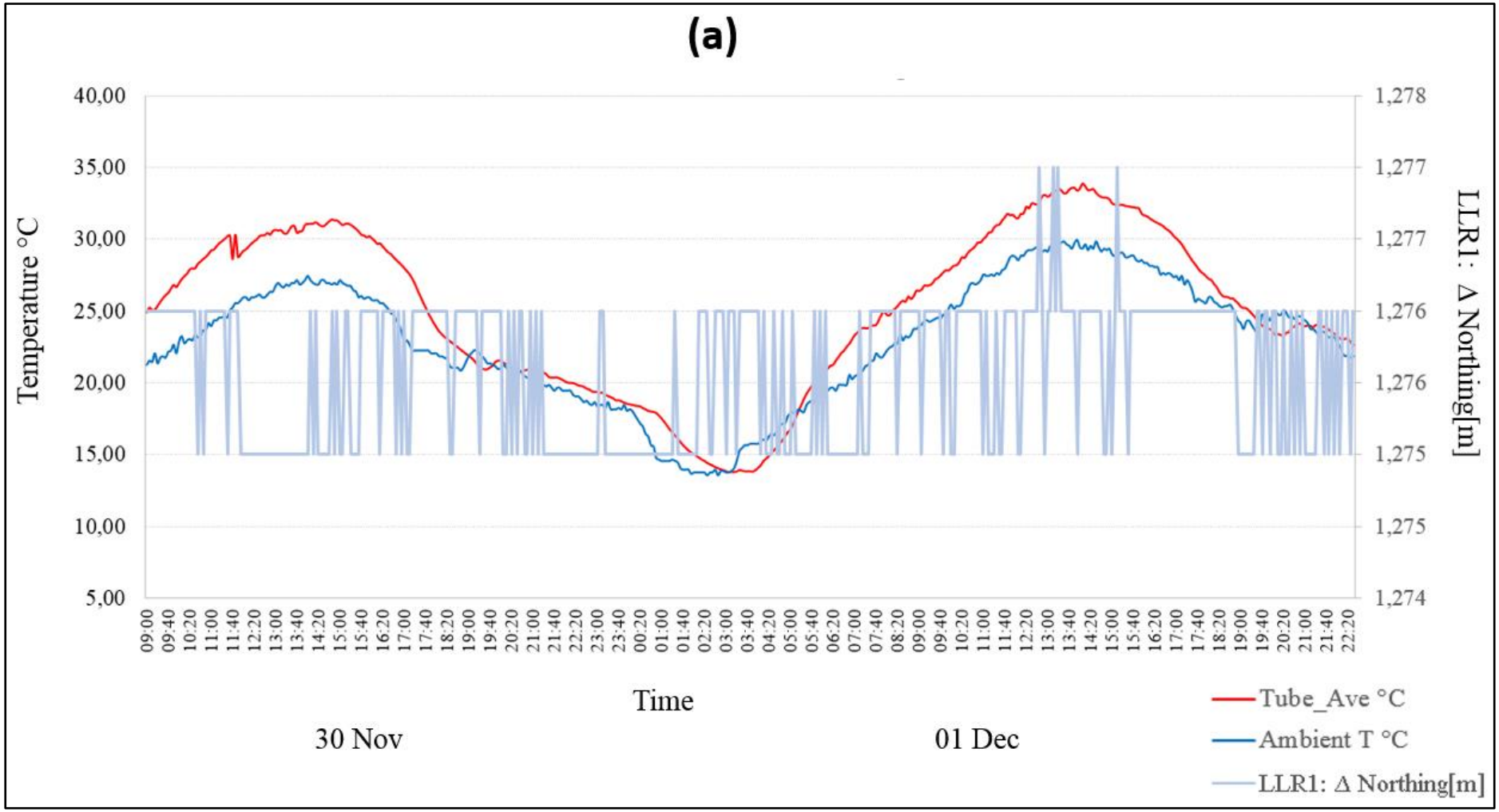

Figure 56: Time series of the (i) measured tube average temperature, (ii) ambient air temperature, and (iii) relative displacements of the tube toward the north at the location where the LLR1 prism was mounted.

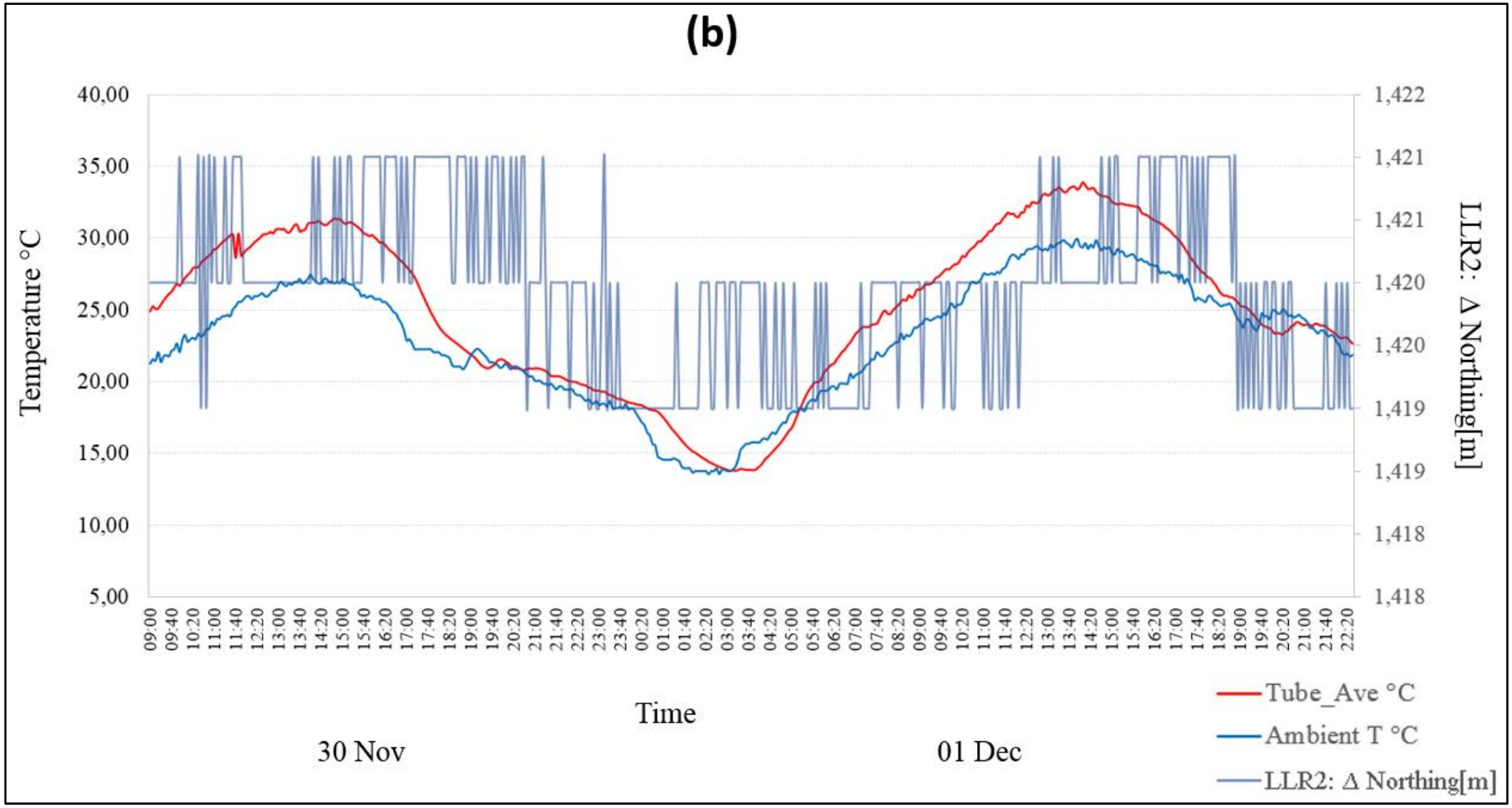

Figure 57: Time series of the (i) measured tube average temperature, (ii) ambient air temperature, and (iii) relative displacements of the tube toward the north at the location where the LLR2 prism was mounted.

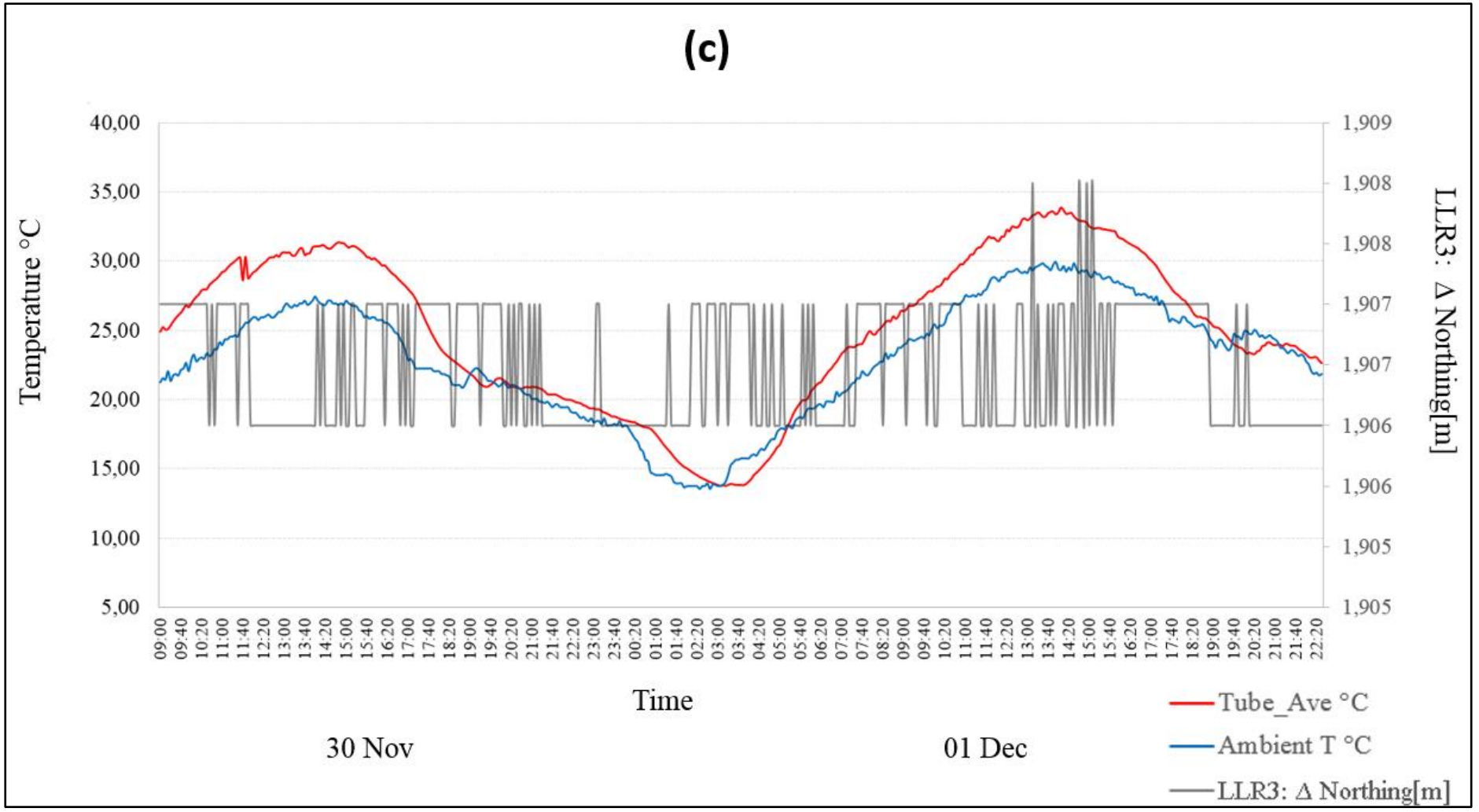

Figure 58: Time series of the (i) measured tube average temperature, (ii) ambient air temperature, and (iii) relative displacements of the tube toward the north at the location where the LLR3 prism was mounted.

4.4.2.3. Sources of error during distance measurements

There are various sources of error that ought to be accounted for, when using the Total Station to acquire distance measurements. The errors may arise from natural, instrument and human errors respectively. In particular, natural errors in distance measurements could be due to, for example atmospheric parameters, gravity, Earth curvature and atmospheric refraction (Torge and Müller, 2012). It is worth mentioning that, the measurements acquired in this study to produce relative displacement results, were automatically corrected for natural errors by the Leica Nova MS50 Total Station (see section 3.2.6). This station compensated for environmental conditions at the site, and further, the curvature and refraction constants were applied to each measurement (http://surveyequipment.com/assets/index/download/id/219/). The constants corrects for the Earth curvature and atmospheric refraction when calculating the horizontal distance and height difference.

Human errors that may arise from physical limitations and observation habits by the surveyor were largely minimized. For example it can be seen on Figure 24 (section 3.2.6) that the Total Station used was mounted onto a fixed white concrete pillar, drilled more than 10 meters underground at the HartRAO site, for purposes of low expansion, target alignment, and stability due to movement or wind around the Total Station. Furthermore, calibration of the Leica Nova MS50 Total Station is carried-out regularly through an interface controlled system on-site to minimize instrument-related errors which can potentially bias the acquired distance measurements.

4.5. Concluding remarks

The modelled and experimental results of the thermal behaviour and thermal distortion dynamics of the HartRAO LLR telescope for possible impact on pointing are presented in this chapter. Firstly, simulation-based-analysis of the extent of influence of T_{∞} on the thermal variations and related deformations of the LLR composite structure, through heat transfer functions was reported. This analysis showed that the thermal response time varies per telescope material component, primarily due to their respective thermal properties. In particular, the spider assembly and outer tube surface had the largest range of thermal variations, and thus were identified as the main areas on the telescope where most thermal variations can be expected.

However, the primary mirror surface including its mount as well as the fork assembly had the lowest range of thermal variations; this is expected as here the mass is the greatest. The total deformations particularly of the tube assembly was found to be in the range 2.9 μm to 40.7 μm from night (00h00) until approximately midday (11h30) while, the primary mirror had virtually zero localised deformations due to its resistance against temperature change. Secondly, the above analysis laid a foundation for proposing a thermal model for monitoring thermal variations and related deformations of the HartRAO LLR telescope composite structure. Several test results of the proposed LLR thermal model were presented in this chapter which covered the placement of RTD sensors on thermally-important areas of the tube structure, as well as measurement and interpolation of tube temperatures. The deformations part of the proposed model was not tested in this study, however, results of tube displacements due to assumed thermal deformations were reported. In particular, the variations of relative tube displacements appeared to concur with the successive peaks of both tube average temperature and T_{∞}.

This finding showed that the tube undergoes structural changes with change in temperature. Furthermore, the smallest variations in relative displacements of the tube were found to be 0.523 mm (east), 0.512 mm (north) and 0.670 mm (height) measured through LLR prism 1 whereas, the largest variations were reportedly 0.418 mm (east), 0.691 mm (north) and 0.751 mm (height) measured through LLR prism 2 during the time period considered. These figures are just an indication of displacement as the precision of the Total Station used for the measurements is at the 1 mm level, but due to its high sampling rate will provide sub-mm ranges statistically. This information could be used in guiding the efforts to determine the amount of correction needed to be fed into the LLR telescope pointing model (Combrinck, 2014) to counteract thermally-induced pointing offsets. The general idea would be to ensure an even distribution of temperature throughout the telescope tube and mount assembly. Especially the areas where mechanical distortion would lead to optical collimation and alignment or focussing errors, such as the secondary mirror spider assembly should have no unevenly heated areas. So far, Combrinck, (2014) operated a prototype pointing and steering software package on a 125 mm dual refractor testbed telescope and achieved RMS error values at the 0.5″ level. It will be interesting to observe the extent of variation of the achieved values, particularly when the pointing model is tested on the actual LLR telescope which will be exposed to the varying thermal environment during operation.

Chapter 5: Conclusion

5.1. General summary

Plans are underway to operate the first-ever LLR station based in the Southern Hemisphere, which would be an addition to the 5 operating LLR stations all located in the Northern Hemisphere. Key to the achievement of the required 1 arcsecond pointing accuracy of the HartRAO LLR, is to have subsystems that can model and correct for the varying telescope disturbances. In particular, various studies over past decades have acknowledged temperature as one of the major disturbances that influence pointing accuracy for numerous optical telescopes, constructed from a combination of material components made of aluminium alloys, steel and optical glasses with varying CTE. For example, it has been shown that temperature variation in the range -6.4 ºC to 25.8 ºC can potentially misalign the tube optical axis and introduce peak azimuth and elevation pointing offsets of 40″ and 10″ respectively (Mittag et al., 2008). Additionally, other studies demonstrated correlations between the antenna pointing errors and temperature-induced deformations on selected structural components of the telescope (Pisanu et al., 2010). In overall, these studies successfully demonstrated that thermal modeling, particularly for an open-air ground-based telescope (such as the HartRAO LLR) may be necessary, which ought to take into account the telescope's structural design, thermal properties of the component materials and site-specific varying climatic factors, in-order to maximize the pointing accuracy of the telescope.

In particular, no study has been previously reported on the thermal behaviour and related structural changes coupled with displacements, of the HartRAO LLR composite structure with respect to ambient air temperature at the observatory site. Currently, a pointing and steering prototype model developed for the HartRAO LLR, has so far only been operated on a 125 mm dual refractor testbed telescope (under room temperature conditions) and achieved root mean squared error values at the 0.5 arcsecond level (Combrinck, 2014). The extent of variation of the achieved error values is currently not known, particularly when the pointing model will be tested on the actual LLR telescope, which will be exposed to the varying thermal environment during operation. Therefore, this research study modelled the thermal behaviour and related distortion dynamics of the HartRAO LLR composite structure for possible impact on the pointing.

5.2. Achievements of objectives and aim

The aim of this research study was to model the thermal behaviour and related distortion dynamics of the HartRAO LLR composite structure for possible impact on pointing, when ranging to the lunar retroreflectors. To achieve the aim of this research study, the following objectives were implemented:

(i) analysis of the extent of influence of varying ambient air temperatures at the HartRAO site on the thermal behaviour (thermal response times, variations and deformations) of the LLR telescope;
(ii) proposing a thermal model for monitoring thermal variations and related deformations of the HartRAO LLR telescope composite structure; and
(iii) quantification of the extent of thermally-induced tube displacements during day- and nighttime, so as to inform efforts to determine the amount of correction needed to be fed into the LLR telescope pointing model (Combrinck, 2014) to counteract thermally-induced pointing offsets.

In particular, the key findings of this research study corresponding to the above-mentioned objectives were as follows:

(i) The thermal response time varies per LLR telescope material component, primarily due to their respective thermal properties. In particular, the spider assembly and outer tube surface had the largest range of thermal variations, and thus were identified as the main areas on the telescope where most thermal variations can be expected. However, the primary mirror surface including its mount as well as the fork assembly had the lowest range of thermal variations. The total deformations particularly of the tube assembly was found to be in the range 2.9 μm to 40.7 μm from night (00h00) until approximately midday (11h30) while, the primary mirror had virtually zero localised deformations due to its resistance against temperature change;

(ii) An LLR thermal dynamic model was proposed and several test results of the proposed model were presented in this study, which covered the placement of RTD sensors on thermally-important areas of the tube structure; measurement and interpolation of the optical tube temperatures. The deformations part of the proposed model was not tested

in this study, however results of tube displacements due to assumed thermal deformations were reported using a laser distance-measurement system. This made it possible to determine structural displacements based on varying magnitudes of the distance variations between the true centre and the apparent centre of the prism;

(iii) The smallest variations in relative displacements of the tube were found to be 0.523 mm (east), 0.512 mm (north) and 0.670 mm (height) whereas, the largest variations were reportedly 0.418 mm (east), 0.691 mm (north) and 0.751 mm (height). This period was characterized by ambient temperatures that varied between 11.20 °C and 29.90 °C and the corresponding tube temperatures that varied between 13.75 °C and 33.84 °C.

These findings demonstrated an attempt to model the thermal behaviour and related distortion dynamics of the HartRAO LLR composite structure for possible impact on pointing; and they constitute an important input for guiding the efforts to determine the amount of correction needed to be fed into the LLR telescope steering and pointing model (Combrinck, 2014) to counteract expected thermally-induced pointing offsets. Furthermore, these results are a step towards the development of a thermal monitoring system for the HartRAO LLR telescope, which is imperative in maximizing the pointing accuracy of the telescope, thereby increasing the chance being on-target with the retroreflectors located on lunar surface. Efforts to maximize pointing accuracy for the HartRAO LLR would adhere to the current state of high-accuracy laser ranging, which currently provides millimeter accuracy (Vasiliev, 2018).

5.3. Contribution to science

No study has been previously reported on the thermal behaviour and related structural changes coupled with displacements, of the HartRAO LLR composite structure with respect to ambient air temperature at the observatory site. One of the basic meteorological parameters which has been studied widely for thermal considerations of site-based open-air telescopes is ambient air temperature. The interaction of the ambient air temperature with the telescope's critical components such as the tube, mirrors and supporting structure, has relatively unique effects on telescope pointing and overall operational performance (Mittag et al., 2008).
In particular, this research study analysed the relative effects induced by the heat transfer mechanisms i.e. conduction and convection, on the thermal variations and response times of the HartRAO-based telescope composite structure. This information was further used to

determine the extent of thermally-induced deformations of the structure, which may cause displacement or misalignment of telescope components was investigated. In particular, the extent of tube displacements due to varying ambient air temperatures at the site during day- and nighttimes was investigated. These efforts were fundamental in understanding the thermal behaviour of the HartRAO-based LLR telescope composite structure in relation to pointing, and as a result, guided the proposal of thermal modelling procedures. These procedures entailed the determination of the types of temperature sensors needed, strategic placement of the sensors the telescope tube (which will later be expanded onto other critical components), and sequence of mathematical steps for data acquisition, monitoring and analysis; so as to determine the amount of correction needed to be fed into the LLR telescope steering and pointing model (Combrinck, 2014) to counteract expected thermally-induced pointing offsets in-order to achieve the required 1 arcsecond pointing accuracy. The findings of this research study (Tsela et al., 2016; Tsela et al., 2016a; Tsela et al., 2016b) have significant scientific implications in exploring strategies and options for developing thermal dynamic models and monitoring systems for current and future LLR optical telescopes.

5.4. Shortcomings of the study

In this study, we assumed a constant h value of 0.025 W/m^{2}C during the thermal simulation process of the telescope. This assumption thus excludes the wind effect during this thermal analysis. The wind effect including the varying h values representative of natural and/or forced convection are possible future considerations for the current analysis so as to approximate reality as far as possible.

Several test results of the proposed LLR thermal model were presented in this study which covered the placement of RTD sensors on thermally-important areas of the tube structure, as well as measurement and interpolation of tube temperatures. However, the deformations part of the thermal model was not tested in this study. This could be an area of further research, and most importantly to implement and test the full thermal model on the telescope. However, these efforts also require complete integration of the telescope material components.

Furthermore, this study determined the magnitude of thermally-induced displacements of the LLR tube front (where the spider assembly is fitted). It would be more informative if

these displacements are analysed over more days and across seasons, and furthermore tested during pointing so as to investigate their contribution to pointing offsets during ranging, and/or if they have any considerable effect on the error values at the 0.5 arcsecond level so far achieved by Combrinck (2014) on a 125 mm dual refractor testbed telescope (under room temperature conditions). In particular, the extent of variation of the achieved error values is currently not known, particularly when the pointing model will be tested on the actual LLR telescope, which will be exposed to the varying thermal environment during operation.

5.5. Recommendation for further research

A comprehensive sensor network set-up is planned for acquiring near real-time temperature measurements of the complete HartRAO LLR telescope composite structure (Figure 59). In particular, the temperature sensors would be strategically mounted onto the telescope surface components and wired to the RTD-based MAQ®20 data acquisition unit. Temperature measurements will be logged and saved on the server for retrieval during thermal modelling and planned ventilation procedures. The red highlighted text on Figure 59 show the component (i.e. optical tube) which the sensor set-up was implemented in this research work (see section 3.4.4.3). It is recommended that further research work, expand the sensor network onto other components such as the primary and secondary mirrors, fork assembly and pedestals, post the revamp and integration processes at HartRAO so to enable a detailed study of the multi-temporal temperature profile of the telescope composite structure.

Furthermore, the proposed thermal model in this study ought to be expanded in-order to realise a fully-functional temperature control system (Figure 60) of the HartRAO LLR telescope. This system would utilise the data acquired in Figure 59 to monitor the thermal behaviour and response times of the telescope's material components in relation to ambient air temperature and relative humidity at the HartRAO site. In particular, the monitoring would incorporate parameters pertaining to the thermal properties of the material components, and a microprocessor controlled venting system. The main aim of the monitoring would be to ensure that the telescope composite structure reaches thermal equilibrium (particularly during the times of ranging), whereas other thermal effects such as dew formation on the mirrors will be controlled through forced air ventilation.

For example, thermal simulation results presented in this study showed that the telescope can reach thermal equilibrium, naturally, particularly in the early morning hours and late in the evening throughout the night. However, the main challenge as seen from the simulation results in this study, is reaching thermal equilibrium during the day when the telescope is exposed to daily oscillating ambient temperatures. Therefore, to have such a monitoring system (Figure 60) could ensure thermal variations are equalized and kept to a minimum as much as possible i.e. < 1 °C (Murphy Jr et al., 2008) to allow excellent telescope pointing, thereby increasing the chance of being on-target with the retroreflectors located on the lunar surface.

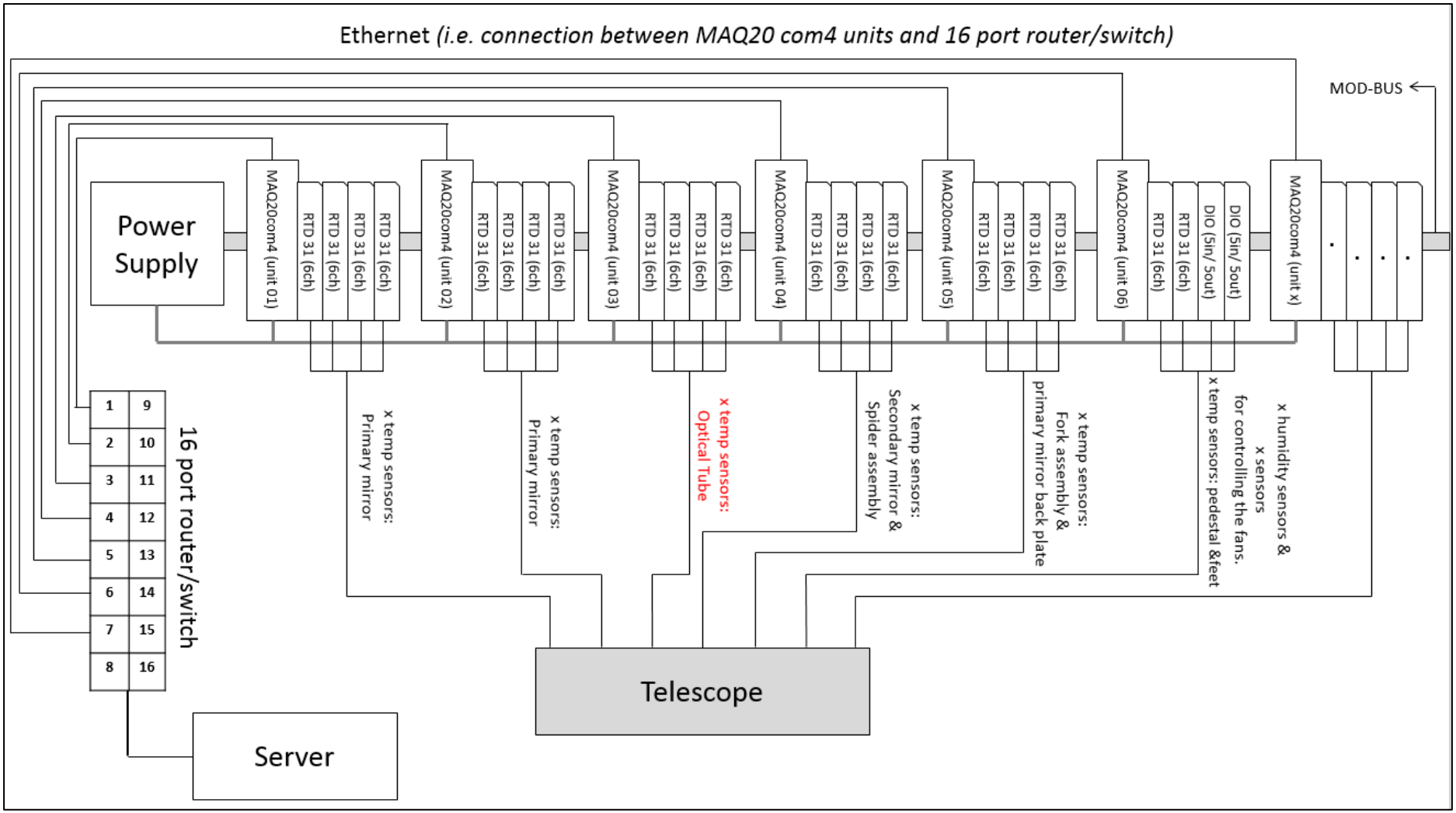

Figure 59: Overview of the planned sensor-network connection set-up of the telescope.

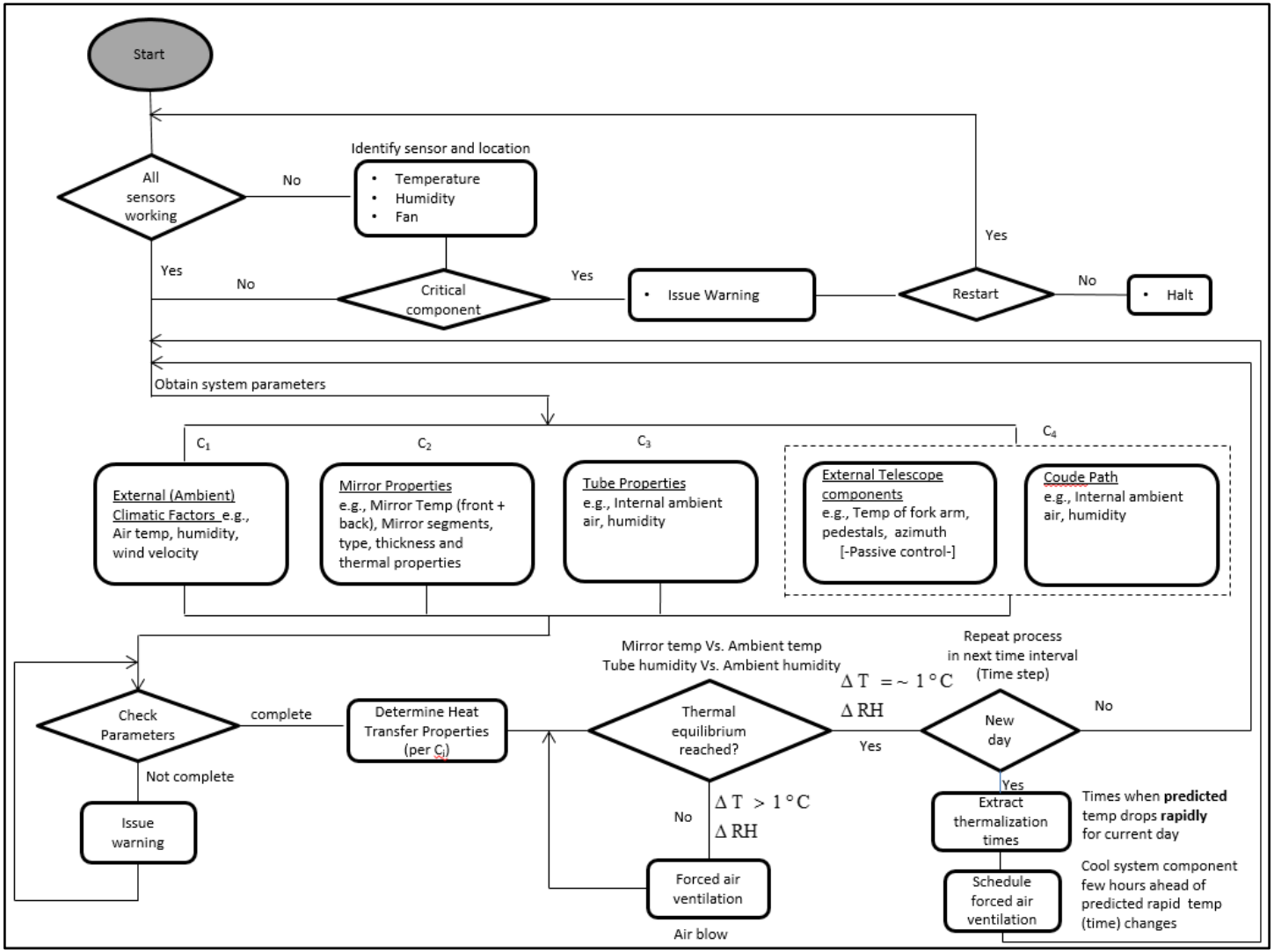

Figure 60: Overview of the planned temperature control system of the HartRAO LLR telescope. The symbols C_i denote the telescope component; RH denotes relative humidity and T denotes the temperature.

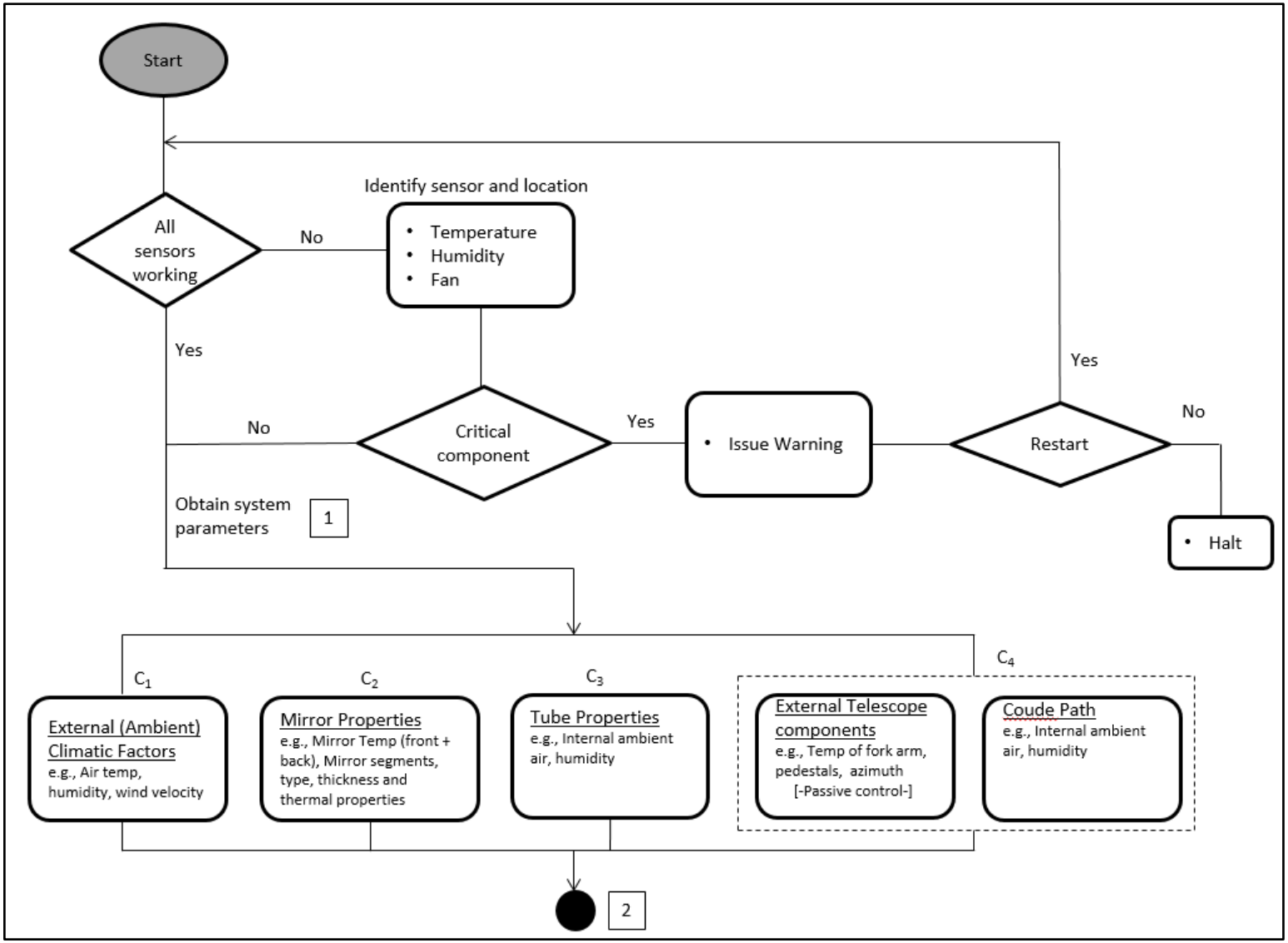

Figure 61: Expanded view of the planned temperature control system in Figure 60, showing system initialization and parameter acquisition.

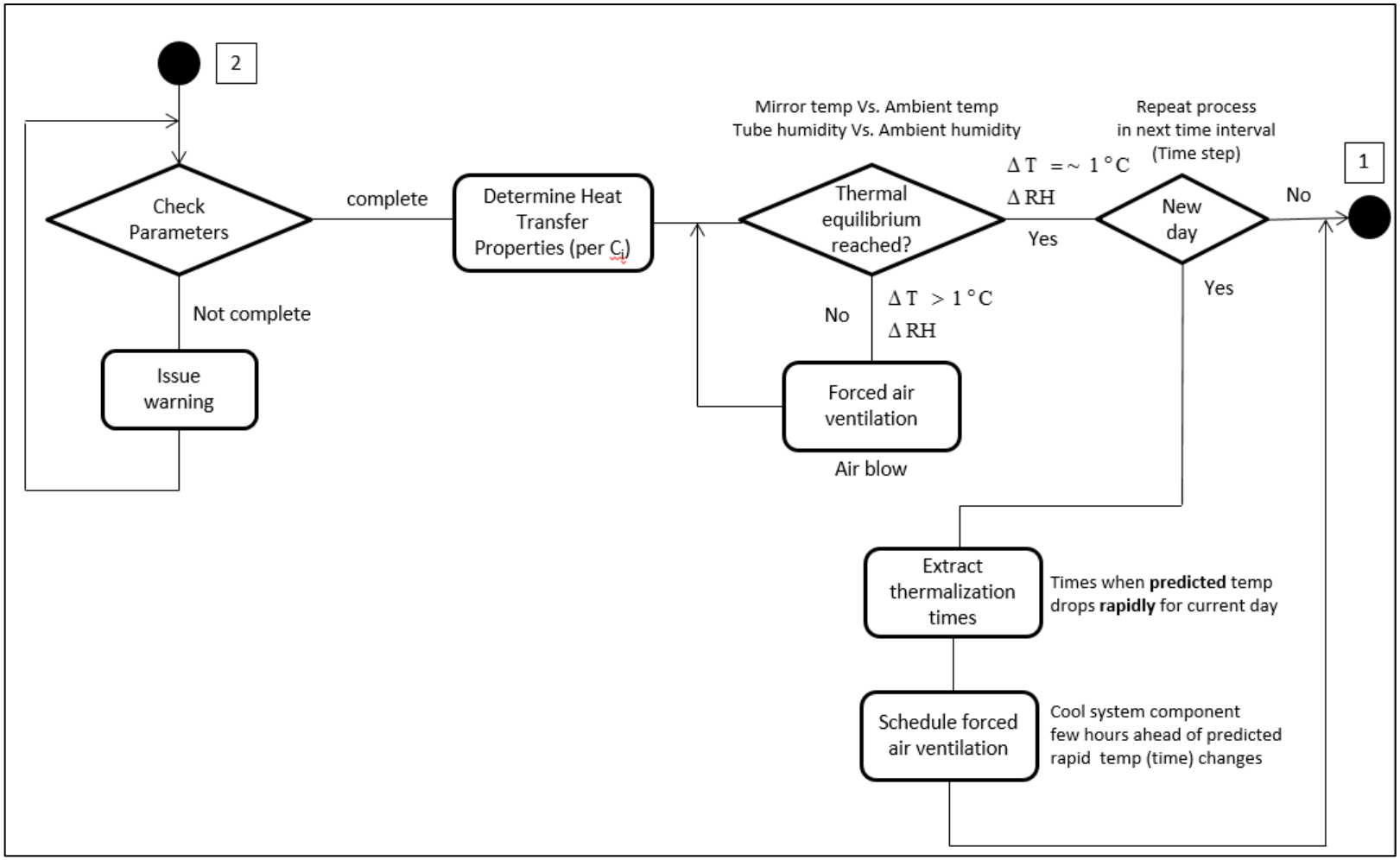

Figure 62: Expanded view of the planned temperature control system in Figure 60, showing the system analysis process.

References

Altamimi, Zuheir, Paul Rebischung, Laurent Métivier, and Xavier Collilieux. 2016. "ITRF2014: A new release of the International Terrestrial Reference Frame modeling nonlinear station motions." Review of. *Journal of Geophysical Research: Solid Earth* 121 (8):6109-31.

Anderson, John D, and JG Williams. 2001. "Long-range tests of the equivalence principle." Review of. *Classical and Quantum Gravity* 18 (13):2447.

Antebi, Joseph, Frank W Kan, and Rajesh S Rao. 1998. Active segmented primary reflector and pointing accuracy of the Large Millimeter Telescope (LMT). Paper presented at the Astronomical Telescopes & Instrumentation.

Atwood, Bruce, and Thomas P O'Brien. 2003. Adjustable truss for support, optical alignment, and athermalization of a Schmidt camera. Paper presented at the Astronomical Telescopes and Instrumentation.

Baars, JWM, BG Hooghoudt, A Greve, and J Penalver. 1988. "Thermal control of the IRAM 30-m millimeter radio telescope." Review of. *Astronomy and Astrophysics* 195:364-71.

Bayley, AM, RJ Davis, JS Haggis, and H Karcher. 1994. "Thermal effects on the pointing of the 32-m MERLIN radio telescope at Cambridge." Review of. *Astronomy and Astrophysics* 283:1051.

Bely, Pierre. 2003. *The design and construction of large optical telescopes*: Springer.

Bender, PL, DG Currie, RH Dicke, DH Eckhardt, J Ek Faller, WM Kaula, JD Mulholland, HH Plotkin, SK Poultney, and EC Silverberg. 1973. "The lunar laser ranging experiment." Review of. *Science* 182 (4109):229-38.

Bergstrand, Sten, Magnus Herbertsson, Carsten Rieck, Jörgen Spetz, Claes-Göran Svantesson, and Rüdiger Haas. 2018. "A gravitational telescope deformation model for geodetic VLBI." Review of. *Journal of Geodesy*:1-12.

Bianco, G, and T Varghese. 1994. The matera laser ranging observatory: current status. Paper presented at the Proc. 9th International Workshop on Laser Ranging Instrumentation, Australian Government Publishing Service,(Canberra).

Bohannan, Bruce, Earl T Pearson, and David Hagelbarger. 2000. Thermal control of classical astronomical primary mirrors. Paper presented at the Optical Design, Materials, Fabrication, and Maintenance.

Borovkov, Alexey I, Denis V Shevchenko, Alexander V Gaev, and Alexander S Nemov. 2004. 3D Finite Element Thermal and Structural Analysis of the RT-70 Full-Circle Radio Telescope. Paper presented at the Proceedings of International ANSYS Conf.

Botha, Roelf Cornelis. 2016. "Development of diode end-pumped Nd: YLF lasers at 1314 nm for high power operation." Stellenbosch: Stellenbosch University.

Bremer, Michael, and Albert Greve. 2011. A dynamic thermal model for design and control of an 800-element open-air radio telescope. Paper presented at the Integrated Modeling of Complex Optomechanical Systems.

Bremer, Michael, and Juan Penalver. 2002. FE model-based interpretation of telescope temperature variations. Paper presented at the Workshop on Integrated Modeling of Telescopes.

Burns, Jack, and Joseph Lazio. 2011. "Planetary Science by the NLSI LUNAR Team: The Lunar Core, Ionized Atmosphere, & Nanodust Weathering." Review of. *arXiv preprint arXiv:1108.3289*.

Calame, O, M-J Fillol, G Guérault, R Muller, A Orszag, J-C Pourny, J Rösch, and Y de Valence. 1970. "Premier échos lumineux sur la lune obtenus par le télémètre laser du Pic du Midi." Review of. *Academie des Sciences Paris Comptes Rendus Serie B Sciences Physiques* 270:1637-40.

Carter, WE, and JD Williams. 1974. University of Hawaii LURE Observatory. Paper presented at the Earth's Gravitational Field and Secular Variations in Position.

Çengel, Yunus A, and Afshin Jahanshahi Ghajar. 2011. *Heat and mass transfer: fundamentals & applications*: McGraw-Hill.

Chapront, J, M Chapront-Touzé, and G Francou. 2002. "A new determination of lunar orbital parameters, precession constant and tidal acceleration from LLR measurements." Review of. *Astronomy & Astrophysics* 387 (2):700-9.

Chapront, J, and G Francou. 2006. "Lunar Laser Ranging: measurements, analysis, and contribution to the reference systems." Review of. *The International Celestial Reference System and Frame*:97.

Cho, Myung, Andrew Corredor, Konstantinos Vogiatzis, and George Angeli. 2009. Thermal performance prediction of the TMT telescope structure. Paper presented at the SPIE Optical Engineering+ Applications.

Cho, Myung, Andrew Corredor, Konstantinos Vogiatzis, and George Angeli. 2010. Thermal analysis of the TMT telescope structure. Paper presented at the SPIE Astronomical Telescopes+ Instrumentation.

Combrinck, L. 2011. Development of a satellite and lunar laser ranger and its future applications. Paper presented at the 62nd International Astronautical Congress.

Combrinck, L, and R Botha. 2014. Challenges and progress with the development of a Lunar Laser Ranger for South Africa.

Combrinck, Ludwig. 2014. Development of a high accuracy, user-friendly Lunar Laser Ranging telescope steering and pointing software package at HartRAO. Paper presented at the 19th International Workshop on Laser Ranging, Annapolis, Maryland.

Courde, C, JM Torre, E Samain, G Martinot-Lagarde, M Aimar, D Albanese, P Exertier, A Fienga, H Mariey, and G Metris. 2017. "Lunar laser ranging in infrared at the Grasse laser station." Review of. *Astronomy & Astrophysics* 602:A90.

Cui, Cunxing, Qibo Feng, and Bin Zhang. 2015. "Compensation for straightness measurement systematic errors in six degree-of-freedom motion error simultaneous measurement system." Review of. *Applied optics* 54 (11):3122-31.

Cui, Morris, Steven A Berg, and Nandini Bhattacharya. 2016. "Distance measurement in air without the precise knowledge of refractive index fluctuation." Review of. *arXiv preprint arXiv:1611.06107*.

Currie, Douglas, Simone Dell'Agnello, and Giovanni Delle Monache. 2011. "A lunar laser ranging retroreflector array for the 21st century." Review of. *Acta Astronautica* 68 (7-8):667-80.

Cova, Sergio, A. Lacaita, P. Lovali, and Franco Zappa. "Performance of near-infrared single-photon detectors in laser ranging measurements." In Proceedings of the 9th International Workshop on Laser Ranging. 1994. Dalcher, AW, TM Yang, and CL Chu. 1977. "High temperature thermal-elastic analysis of dissimilar metal transition joints." Review of. *Journal of Engineering Materials and Technology* 99 (1):65-9.

Dalcher, A. W., T. M. Yang, and C. L. Chu. 1977. High temperature thermal-elastic analysis of dissimilar metal transition joints. Journal of Engineering Materials and Technology, 99(1), pp.65-69.

Degnan, John J. 1993. "Millimeter accuracy satellite laser ranging: a review." Review of. *Contributions of space geodesy to geodynamics: technology* 25:133-62.

Dickey, Jean O, PL Bender, JE Faller, XX Newhall, RL Ricklefs, JG Ries, PJ Shelus, C Veillet, AL Whipple, and JR Wiant. 1994. "Lunar laser ranging: A continuing legacy of the Apollo program." Review of. *Science* 265 (5171):482-90.

Énard, Daniel, André Maréchal, and Jean Espiard. 1996. "Progress in ground-based optical telescopes." Review of. *Reports on Progress in Physics* 59 (5):601.

Faller, James, Irvin Winer, Walter Carrion, Thomas S Johnson, Paul Spadin, Lloyd Robinson, E Joseph Wampler, and Donald Wieber. 1969. "Laser beam directed at the lunar retro-

reflector array: observations of the first returns." Review of. *Science* 166 (3901):99-102.

Fienga, A, C Courde, JM Torre, H Manche, T Murphy, J Mueller, J Laskar, S Bouquillon, L Biskupek, and F Hofmann. 2014. "Interests of a new lunar laser instrumentation on the ESO NTT Telescope." Review of. *arXiv preprint arXiv:1405.0473*.

Green, Don W. 2008. *Perry's chemical engineers' handbook*. Vol. 796: McGraw-hill New York.

Greene, Ben, and John McK Luck. LLR developments at Mount Stromlo. Paper presented at the 13 International Workshop on Laser Ranging.

Greenhalgh, R Justin S, Larry M Stepp, and Eric R Hansen. 1994. Gemini primary mirror thermal management system. Paper presented at the 1994 Symposium on Astronomical Telescopes & Instrumentation for the 21st Century.

Greiner, Benjamin, Bernhard Malicek, Michael Lachenmann, Alfred Krabbe, and Jörg Wagner. 2018. A new finite element model of the SOFIA primary mirror cell to investigate dynamical behavior. Paper presented at the Ground-based and Airborne Telescopes VII.

Greve, A, JWM Baars, J Penalver, and B LeFloch. 1996. "Near–focus active optics: An inexpensive method to improve millimeter–wavelength radio telescopes." Review of. *Radio Science* 31 (5):1053-65.

Greve, A, and G MacLeod. 2001. "Thermal model calculations of enclosures for millimeter wavelength radio telescopes." Review of. *Radio Science* 36 (5):1111-28.

Greve, Albert, and Michael Bremer. 2010. *Thermal design and thermal behaviour of radio telescopes and their enclosures*. Vol. 364: Springer.

Greve, Albert, Michael Bremer, Juan Penalver, Philippe Raffin, and David Morris. 2005. "Improvement of the IRAM 30-m telescope from temperature measurements and finite-element calculations." Review of. *Antennas and Propagation, IEEE Transactions on* 53 (2):851-60.

Greve, Albert, and Hans Juergen Kaercher. 2009. "Performance improvement of a flexible telescope through metrology and active control." Review of. *Proceedings of the IEEE* 97 (8):1412-20.

Greve, Albert, and Jeff Mangum. 2008. "Mechanical measurements of the ALMA prototype antennas." Review of. *Antennas and Propagation Magazine, IEEE* 50 (2):66-80.

Hartebeesthoek Radio Astronomy Observatory (HartRAO). 2005. Proposed re-location and conversion of CNES SLR system to South Africa in collaboration with OCA and the

greater ILRS community. Retrieved August, 2013, from http://www.hartrao.ac.za/iisgeo/docs/LLR_proposal.doc.

Hofmann, Franz, Liliane Biskupek, and Jürgen Müller. 2018. "Contributions to reference systems from Lunar Laser Ranging using the IfE analysis model." Review of. *Journal of Geodesy*:1-13.

Hofmann, Franz, Jürgen Müller, and Liliane Biskupek. "Lunar Laser Ranging: Das Erde-Mond-System und Tests der Einstein'schen Gravitationstheorie." Review of.

Hofmann, F, J Müller, and L Biskupek. 2010. "Lunar laser ranging test of the Nordtvedt parameter and a possible variation in the gravitational constant." Review of. *Astronomy & Astrophysics* 522:L5.

Hu, Pengcheng, Shuai Mao, and Jiu-Bin Tan. 2015. "Compensation of errors due to incident beam drift in a 3 DOF measurement system for linear guide motion." Review of. *Optics Express* 23 (22):28389-401.

Hunt, Mahlon S. 1974. "The AFCRL Lunar Laser Experiment." In.: AIR FORCE CAMBRIDGE RESEARCH LABS LG HANSCOM FIELD MASS.

Ibrahim, Dogan. 2002. *Microcontroller-based temperature monitoring and control*: Newnes.

Itzler, Mark A, Xudong Jiang, Mark Entwistle, Krystyna Slomkowski, Alberto Tosi, Fabio Acerbi, Franco Zappa, and Sergio Cova. 2011. "Advances in InGaAsP-based avalanche diode single photon detectors." Review of. *Journal of Modern Optics* 58 (3-4):174-200.

Jedamzik, Ralf, Thoralf Johansson, and Thomas Westerhoff. 2010. Modeling of the thermal expansion behaviour of ZERODUR at arbitrary temperature profiles. Paper presented at the SPIE Astronomical Telescopes+ Instrumentation.

Jensen, John R. 2009. *Remote sensing of the environment: An earth resource perspective 2/e*: Pearson Education India.

Khan, Amir, Klaus Mosegaard, JG Williams, and P Lognonné. 2004. "Does the Moon possess a molten core? Probing the deep lunar interior using results from LLR and Lunar Prospector." Review of. *Journal of Geophysical Research: Planets* 109 (E9).

Konopliv, AS, AB Binder, LL Hood, AB Kucinskas, WL Sjogren, and JG Williams. 1998. "Improved gravity field of the Moon from Lunar Prospector." Review of. *Science* 281 (5382):1476-80.

Kozai, Y. 1972. Lunar laser ranging experiments in Japan. Paper presented at the Space Research Conference.

Lamb, James W, and David P Woody. 1998. "Thermal behavior of the Leighton 10-m antenna backing structure." Review of. *NRAO Millimeter Array Memo Series* (234).

Lowne, CM. 1979. "An investigation of the effects of mirror temperature upon telescope seeing." Review of. *Monthly Notices of the Royal Astronomical Society* 188 (2):249-59.

Märki, Andreas. 2018. "Lunar laser ranging: A review." Review of. *arXiv preprint arXiv:1805.05863*.

Martini, M, S Dell'Agnello, D Currie, G Delle Monache, R Vittori, JF Chandler, C Cantone, A Boni, S Berardi, and G Patrizi. 2012. "MoonLIGHT: A USA–Italy lunar laser ranging retroreflector array for the 21st century." Review of. *Planetary and Space Science* 74 (1):276-82.

Medwadoski, S. 1981. "UC telescope pier rotations due to wind action on the observatory dome." In.: Keck Report.

Merkowitz, Stephen M. 2010. "Tests of gravity using lunar laser ranging." Review of. *Living Reviews in Relativity* 13 (1):7.

Mészáros, László, Attila Jaskó, András Pál, and Gergely Csépány. 2014. "Accurate Telescope Mount Positioning with MEMS Accelerometers." Review of. *arXiv preprint arXiv:1407.0035*.

Mittag, M, A Hempelmann, JN Gonzalez-Perez, and JHMM Schmitt. 2008. "The Temperature Dependence of the Pointing Model of the Hamburg Robotic Telescope." Review of. *Publications of the Astronomical Society of the Pacific* 120 (866):425-9.

Müller, J, and V Tesmer. 2002. "Investigation of tidal effects in lunar laser ranging." Review of. *Journal of Geodesy* 76 (4):232-7.

Müller, Jürgen, and Liliane Biskupek. 2007. "Variations of the gravitational constant from lunar laser ranging data." Review of. *Classical and Quantum Gravity* 24 (17):4533.

Müller, Jürgen, James G Williams, and Slava G Turyshev. 2008. "Lunar laser ranging contributions to relativity and geodesy." In *Lasers, Clocks and Drag-Free Control*, 457-72. Springer.

Mulholland, J Derral. 1977. "Mathematical Modelling of Lunar Laser Measures and their Application to Improvement of Physical Parameters." In *Scientific Applications of Lunar Laser Ranging*, 9-18. Springer.

Munghemezulu, C, L Combrinck, and OJ Botai. 2018. "A case study of the application of GPS to lunar laser ranging timing systems." Review of. *Journal of Applied Geodesy* 12 (4):279-87.

Munghemezulu, Cilence. 2018. "Development of an Integrated Timing System for the HartRAO Lunar Laser Ranging Station." University of Pretoria.

Munghemezulu, Cilence, Ludwig Combrinck, and Joel O Botai. 2016. "A review of the lunar laser ranging technique and contribution of timing systems." Review of. *South African Journal of Science* 112 (3-4):1-9.

Murphy Jr, TW, EG Adelberger, JD Strasburg, CW Stubbs, and K Nordtvedt. 2004. "Testing gravity via next-generation lunar laser-ranging." Review of. *Nuclear Physics B-Proceedings Supplements* 134:155-62.

Murphy Jr, TW, Eric G Adelberger, JBR Battat, LN Carey, Charles D Hoyle, P LeBlanc, EL Michelsen, K Nordtvedt, AE Orin, and Jana D Strasburg. 2008. "The apache point observatory lunar laser-ranging operation: instrument description and first detections." Review of. *Publications of the Astronomical Society of the Pacific* 120 (863):20-37.

Murphy, TW. 2013. "Lunar laser ranging: the millimeter challenge." Review of. *Reports on Progress in Physics* 76 (7):076901.

Ndlovu, SC, WL Combrinck, M Akombelwa, and N Chetty. 2016. "Variable link equation parameters and expected photon returns for the HartRAO Lunar Laser Ranger-Improving our understanding of the Earth-Moon system." Review of. *South African Journal of Geology 2016* 119 (1):77-82.

Nickola, G Leslie, and Ludwig Combrinck. 2011. "High-precision steering and pointing control of a lunar/satellite laser ranging telescope." Review of. *South African journal of geology* 114 (3-4):577-80.

Nickola, M, RC Botha, Igor Esau, George D Djolov, and WL Combrinck. 2011. "Site characterisation: Astronomical seeing from a turbulence-resolving model." Review of. *South African journal of geology* 114 (3-4):581-4.

Nkosi, N, WL Combrinck, and M Akombelwa. 2016. "Optical configuration and optical tests of the HartRAO Lunar Laser Ranger." Review of. *South African Journal of Geology 2016* 119 (1):99-108.

Noda, H, H Kunimori, and H Araki. 2014. Lunar Laser Ranging Experiment at Koganei SLR Station. Paper presented at the Lunar and Planetary Science Conference.

Nordtvedt Jr, Kenneth. 1968. "Testing relativity with laser ranging to the moon." Review of. *Physical Review* 170 (5):1186.

Nordtvedt, Kenneth. 1999. "30 years of lunar laser ranging and the gravitational interaction." Review of. *Classical and Quantum Gravity* 16 (12A):A101.

Onwubolu, Godfrey. 2013. *Computer-aided engineering design with SolidWorks*: World Scientific Publishing Company.

Pantic, S, L Candanedo, and AK Athienitis. 2010. "Modeling of energy performance of a house with three configurations of building-integrated photovoltaic/thermal systems." Review of. *Energy and buildings* 42 (10):1779-89.

Pavlov, Dmitry A, James G Williams, and Vladimir V Suvorkin. 2016. "Determining parameters of Moon's orbital and rotational motion from LLR observations using GRAIL and IERS-recommended models." Review of. *Celestial Mechanics and Dynamical Astronomy* 126 (1-3):61-88.

Pearlman, Michael R, Carey E Noll, Erricos C Pavlis, Frank G Lemoine, Ludwig Combrink, John J Degnan, Georg Kirchner, and Ulrich Schreiber. 2019. "The ILRS: approaching 20 years and planning for the future." Review of. *Journal of Geodesy*:1-20.

Perry, JW. 1943. "Thermal effects upon the performance of lens systems." Review of. *Proceedings of the Physical Society* 55 (4):257.

Pisanu, Tonino, Franco Buffa, Marco Morsiani, Claudio Pernechele, and Sergio Poppi. 2010. Thermal behavior of the Medicina 32-meter radio telescope. Paper presented at the SPIE Astronomical Telescopes+ Instrumentation.

Plaza, D. 2001. Diploma thesis, Tübingen: University of Tübingen

Pradhan, Saibal, and Susanta Sen. 1999. "An improved lead compensation technique for three-wire resistance temperature detectors." Review of. *IEEE Transactions on Instrumentation and Measurement* 48 (5):903-5.

Prochazka, Ivan, Jan Kodet, Josef Blazej, Georg Kirchner, and Franz Koidl. 2014. "Photon counting detector for space debris laser tracking and lunar laser ranging." Review of. *Advances in Space Research* 54 (4):755-8.

Samain, E, JF Mangin, C Veillet, JM Torre, P Fridelance, JE Chabaudie, D Feraudy, M Glentzlin, J Pham Van, and M Furia. 1998. "Millimetric lunar laser ranging at OCA (Observatoire de la Côte d'Azur)." Review of. *Astronomy and Astrophysics Supplement Series* 130 (2):235-44.

Samain, E. and Mangin, J. Detector Studies for Millimetric Lunar Laser Ranging at OCA, p. 449. 9th International Workshop on Laser Ranging Instrumentation, Canberra, Australia, November 7-11, 1994

Saydi, J, A Lotfalian, M Abedi, J Khalilzadeh, and H Saghafifar. 2014. "Atmospheric error correction of the laser beam ranging." Review of. *Advances in Meteorology* 2014.

Schott, AG. 2011. "ZERODUR®–Zero Expansion Glass Ceramic." Review of. *Data sheet, Mainz*.

Seeber, Günter. 2008. *Satellite geodesy: foundations, methods, and applications*: Walter de gruyter.

Shelus, Peter J. 1985. "MLRS: A lunar/artificial satellite laser ranging facility at the McDonald Observatory." Review of. *IEEE transactions on geoscience and remote sensing* (4):385-90.

Shinnaga, Hiroko, R Chamberlin, T Phillips, D Dowel, H Yoshida, and R Peng. 2004. "A consideration of thermal effect on pointing measured on a Nasmyth focus of the CSO 10.4 m Leighton telescope at k350 lm." In.: Technical memorandum.

Silverberg, EC. 1974. "Operation and performance of a lunar laser ranging station." Review of. *Applied optics* 13 (3):565-74.

Tantele, Elia A, Renos A Votsis, and Nicholas Kyriakides. 2018. Applications of thermal imaging camera for assessing structural integrity. Paper presented at the Sixth International Conference on Remote Sensing and Geoinformation of the Environment (RSCy2018).

Tsela, P, Ludwig Combrinck, R Botha, and B Ngcobo. 2016a. "Thermal analysis of the LLR optical telescope tube assembly based in Hartebeesthoek Radio Astronomy Observatory." Review of. *Acta Geodaetica et Geophysica* 51 (3):393-403.

Tsela, Philemon Lehlohonolo, Ludwig Combrinck, and Bongani Ngcobo. 2016. "A spatiotemporal analysis of the effect of ambient temperatures on the thermal behaviour of the Lunar Laser Ranging optical telescope at Hartebeesthoek Radio Astronomy Observatory." Review of. *South African Journal of Geomatics* 5 (3):373-92.

Tsela, PL, WL Combrinck, RC Botha, and BL Ngcobo. 2016b. "A proposed mathematical model of thermal variations on the HartRAO Lunar Laser Ranging telescope for enhanced test of Earth-Moon system dynamics." Review of. *South African Journal of Geology 2016* 119 (1):83-90.

Turyshev, Slava G, and James G Williams. 2007. "Space-based tests of gravity with laser ranging." Review of. *International Journal of Modern Physics D* 16 (12a):2165-79.

Turyshev, Slava G, James G Williams, William M Folkner, Gary M Gutt, Richard T Baran, Randall C Hein, Ruwan P Somawardhana, John A Lipa, and Suwen Wang. 2013. "Corner-cube retro-reflector instrument for advanced lunar laser ranging." Review of. *Experimental Astronomy* 36 (1-2):105-35.

Torge, Wolfgang, and Jürgen Müller. 2012. *Geodesy*: Walter de Gruyter.

Ukita, Nobuharu. 1999. "Thermal effects on the pointing of the Nobeyama 45-m telescope." Review of. *Publications of the National Astronomical Observatory of Japan* 5:139-47.

Ukita, Nobuharu, Hajime Ezawa, Bungo Ikenoue, and Masao Saito. 2007. "Thermal and wind effects on the azimuth axis tilt of the ASTE 10-m antenna." Review of. *Publ. Natl. Astron. Obs* 10:25-33.

Vasiliev, Vladimir Pavlovich. 2018. "Current state of high-accuracy laser ranging." Review of. *Physics-Uspekhi* 61 (7):707.

Vasilyev, MV, EI Yagudina, Jean-Marie Torre, and Dominique Feraudy. 2014. "Planned LLR station in Russia and its impact on the lunar ephemeris accuracy." Review of. *Resent developments and prospects in ground-based and space astrometry, Journees* 22:112.

Veillet, C, JF Mangin, JE Chabaubie, C Dumolin, D Feraudy, and JM Torre. 1993. "Lunar laser ranging at CERGA for the ruby period (1981-1986)." In *Contributions of space geodesy to geodynamics: technology*, 189-93. Wiley Online Library.

Viswanathan, V, A Fienga, M Gastineau, and J Laskar. 2017. "INPOP17a planetary ephemerides." Review of. *Notes Scientifiques et Techniques de l'Institut de mécanique céleste,(ISSN 1621–3823),# 108, ISBN 2-910015-79-3, 2017, 39 pp.* 108.

Viswanathan, Vishnu, Agnes Fienga, Clement Courde, Jean-Marie Torre, Pierre Exertier, Etienne Samain, Dominique Feraudy, Dominique Albanese, Mourad Aimar, and Hervé Mariey. 2016. LLR data analysis and impact on lunar dynamics from recent developments at OCA LLR Station. Paper presented at the EGU General Assembly Conference Abstracts.

Viswanathan, Vishnu, Agnes Fienga, Herve Manche, Mickael Gastineau, Clement Courde, Jean Marie Torre, Pierre Exertier, and Jacques Laskar. 2017. Infrared Lunar Laser Ranging at Calern: Impact on Lunar Dynamics. Paper presented at the EGU General Assembly Conference Abstracts.

Vogiatzis, Konstantinos. 2010. Thermal modeling environment for TMT. Paper presented at the SPIE Astronomical Telescopes+ Instrumentation.

Vogiatzis, Konstantinos, Amir Sadjadpour, and Scott Roberts. 2014. TMT Telescope Structure thermal model. Paper presented at the SPIE Astronomical Telescopes+ Instrumentation.

von Hoerner, Sebastian, and Woon-Yin Wong. 1975. "Gravitational deformation and astigmatism of tiltable radio telescopes." Review of. *IEEE Transactions on antennas and propagation* 23 (5):689-95.

Wang, Hairen, Jingquan Cheng, Zheng Lou, Ming Liang, Xianzhong Zheng, Yingxi Zuo, and Ji Yang. 2018. "A comparative study of the thermal performance of primary mirror at the four typical sites." Review of. *Optik* 174:727-38.

Williams, James G, and Dale H Boggs. 2008. Lunar core and mantle. What does LLR see. Paper presented at the Proceedings of the 16th International Workshop on Laser Ranging, held on.

Williams, James G, XX Newhall, and Jean O Dickey. 1996. "Lunar moments, tides, orientation, and coordinate frames." Review of. *Planetary and Space Science* 44 (10):1077-80.

Williams, James G, Slava G Turyshev, and Dale H Boggs. 2004. "Progress in lunar laser ranging tests of relativistic gravity." Review of. *Physical Review Letters* 93 (26):261101.

Williams, James G., Slava G. Turyshev, and Dale H. Boggs. 2012. "Lunar laser ranging tests of the equivalence principle." Review of. *Classical and Quantum Gravity* 29 (18):184004.

Williams, James G, Slava G Turyshev, and Thomas W Murphy Jr. 2004. "Improving LLR tests of gravitational theory." Review of. *International Journal of Modern Physics D* 13 (03):567-82.

Williams, J. G., turyshev, S. G. & boggs, D. H. 2009. Lunar laser ranging tests of the equivalence principle with the earth and moon. *International Journal of Modern Physics D*, 18**,** 1129-1175.

Williams, JG, DH Boggs, JO Dickey, and WM Folkner. 2002. Lunar laser tests of gravitational physics. Paper presented at the The Ninth Marcel Grossmann Meeting: On Recent Developments in Theoretical and Experimental General Relativity, Gravitation and Relativistic Field Theories (In 3 Volumes).

Williams, JG, DH Boggs, and JT Ratcliff. 2004. Lunar core and tides. Paper presented at the Lunar and Planetary Science Conference.

Williams, JG, RH Dicke, PL Bender, CO Alley, WE Carter, DG Currie, DH Eckhardt, JE Faller, WM Kaula, and JD Mulholland. 1976. "New test of the equivalence principle from lunar laser ranging." Review of. *Physical Review Letters* 36 (11):551.

Wresnik, Joerg, Rüdiger Haas, Johannes Boehm, and Harald Schuh. 2007. "Modeling thermal deformation of VLBI antennas with a new temperature model." Review of. *Journal of Geodesy* 81 (6-8):423-31.

Yang, Rongqian, and Yazhu Chen. 2011. "Design of a 3-D infrared imaging system using structured light." Review of. *IEEE Transactions on Instrumentation and Measurement* 60 (2):608-17.

Yoon, Jae-San, Hong-Il Kim, Jae-Hung Han, and Ho-Soon Yang. 2012. "Effect of dimensional stability of composites on optical performances of space telescopes." Review of. *Journal of Aerospace Engineering* 27 (1):40-7.

Zago, Lorenzo. 1997. Engineering handbook for local and dome seeing. Paper presented at the Optical Telescopes of Today and Tomorrow.

Zheng, Guoxian, Feng Zhou, Jianfeng Liu, Tuotuo Li, Ning An, and Binglong Zhang. 2012. "Influence of temperature on divergence angle of a focal telescope used in laser optical communication." Review of. *Optics Express* 20 (12):13208-14.